Doctoral Dissertation

Studies on Conformational Dynamics of Oligonucleotide and Its Photoregulation

オリゴヌクレオチドのコンフォメーションダイナミクスとその光制御に関する研究

JIE XU

June 2020

Division of Applied Chemistry,
Graduate School of Engineering,
Osaka University

Preface

The studies presented in this dissertation were carried out under the directions of Professor Mamoru Fujitsuka and Associate Professor Kiyohiko Kawai, the institute of Scientific and Industrial Research (SANKEN), Osaka University from October 2017 to June 2020.

The object of this dissertation is to study the dynamics of oligonucleotide looping and its photoregualtion. The research aims to study the dynamics of oligonucleotide looping at a long timescale (> 1 μs) under physiological conditions and to reveal the factors affecting the dynamics. The author hopes that the results and conclusions presented in this dissertation contribute to the further understanding of the conformational dynamics of oligonucleotides.

Jie Xu

Division of Applied Chemistry
Graduate School of Engineering
Osaka University
2020

Contents

General Introduction

The proper functioning of biomolecules comprises the core of cell life. The conformational diversity of biomolecules plays a pivotal role in their functions. Biomolecules such as proteins, polypeptides, and nucleic acids are all dynamic macromolecules and have several common characteristics. They all exhibit a fundamental relationship between conformation and function and they all have transient conformations that are dependent on time and the surrounding environment. Studies focusing on the conformational dynamics of biomolecules are critical in gaining knowledge on the organizations and activities of biomolecules in the fundamental processes of life and thereby on clarifications of disease progressions.[1–3] The studies can provide valuable perspectives on many up-to-date unsolved problems: how a protein molecule folds from the primary structure to the intricate 3D functional structure, how monomeric peptides or proteins polymerize into long unbranched fibers with a cross-β structure called amyloids which are known to be associated with human diseases, how RNA folds into elaborate structures, to name but a few.

Nucleic acids, DNA and RNA, are biomolecules carrying the genetic information necessary to create life and specify the function of any particular organism. Besides, they are of crucial functional importance in various physiological activities.[4–6] Conformational transition is the basis for many oligonucleotides to accomplish their crucial physiological roles. For example, it is reported that through Chi (crossover hotspot instigator) recognition-promoted formation of a growing single-stranded DNA (ssDNA) loop which is topologically resistant to reannealing the unwinding of DNA duplex by a bacterial helicases-nuclease complex AddAB bypasses ssDNA-binding protein.[4] It is proposed that DNA helicase might use ssDNA loop formation as a general strategy to promote the unwinding of DNA duplex.[4] Looping of single-stranded RNA (ssRNA) is demonstrated to be the mechanism of translation initiation by a 40S ribosomal submit.[7] It also provides the basis for ssRNA to fold into diverse secondary and tertiary structures.

Given both the functional and structural importance of oligonucleotide looping, it is critical to study the dynamics of oligonucleotide looping. Knowledge of the conformational dynamics of oligonucleotides will constitute the framework for understanding the associated functional and structural importance.

Dynamics of oligonucleotide looping has been experimentally studied by quenching of

fluorescence,[8–10] which accompanied the study of the looping dynamins of polypeptides.[11,12] As shown in scheme 1, a fluorescent molecule and its quencher are attached at both ends of an oligonucleotide molecule. The looping rate was measured through the intramolecular fluorescence quenching of the fluorescent molecule by its quencher. When the quenching of fluorescence is efficient, the formation of a loop ($k_{looping}$) is followed by the immediate deactivation of the fluorescence molecule by the quencher (k_d) which occurs faster than the dissociation of the loop ($k_{unlooping}$). Therefore, the quenching rate constant of the fluorescence molecule reflects the looping rate of the oligonucleotide molecule.[10]

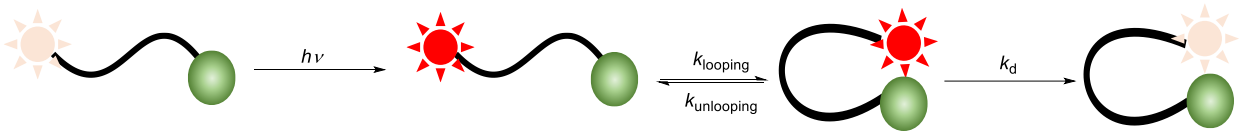

Scheme 1. Schematic illustration of using the methodology of quenching of fluorescence for studying the looping dynamics of oligonucleotides.

The fluorescence quenching of DBO by guanine has been used by Nau *et al*. in the study of looping dynamics of short single-stranded DNA (ssDNA), dimer or tetramer.[10] The looping dynamics of longer ssDNA with a length longer than 5 bases was studied by Uzawa *et al*. based on the fluorescence quenching of a ruthenium tris(bipyridine) fluorophore (Ru) by methyl ethyl viologen (MV) or 4-Dimethylaminoazobenzene-4'-sulfonyl (DABSYL).[8,9] While either the back electron transfer between Ru and MV[13] or Förster resonance transfer (FRET)-trigged fluorescence quenching when using DABSYL as the quencher competes with the electron transition (ET)-trigged fluorescence quenching of Ru,[9] making the system complicated. For both systems mentioned above, the fluorescence lifetimes of fluorescent molecules in water in the absence of quenchers are 420 ns and 650 ns, respectively.[8–10] Therefore, these systems will not be valid when the conformational dynamics of oligonucleotide occurs at a long timescale (> 1 μs).

The looping dynamics of (dA)-rich or (dT)-rich oligonucleotide from trimer to 9-mer has been studied in our previous work by observing the formation rate of pyrene dimer radical cation ($Py_2^{\bullet+}$) using laser flash photolysis technique.[14] As shown in Scheme 2, two pyrene (Py) molecules are attached at both ends of an oligonucleotide molecule. Through photoionization, pyrene radical cation ($Py^{\bullet+}$) is firstly formed at the one end, and it associates with its neutral

counterpart (Py) at the other end of the same oligonucleotide molecule during oligonucleotide looping to form $Py_2^{\bullet+}$. When a loop is formed, $Py_2^{\bullet+}$ is formed. Thus, the formation of $Py_2^{\bullet+}$ reflects the looping dynamics of oligonucleotide modified by Pys. Due to the long lifetimes of $Py^{\bullet+}$ and $Py_2^{\bullet+}$ (0.1–100 μs), dynamics of oligonucleotide looping in a wide time range of 10 ns–1 ms can be studied using this methodology.[14] However, the hydrophobicity of Py sets a barrier for its further use under physiological conditions.[15] A water-soluble Py derivative is highly desired.

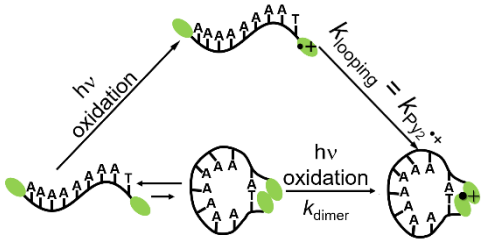

Scheme 2. Schematic illustration of the methodology of using the formation of $Py_2^{\bullet+}$ for studying the looping dynamics of oligonucleotides.

Apart from using the approach of quenching of fluorescence and the methodology of observing the formation rate of $Py_2^{\bullet+}$ established in our lab using laser flash photolysis technique, dynamics of oligonucleotides can also be studied by fluorescence blinking, which has drawn growing attention in the recent years owing to the remarkable development of fluorescence microscopy.[16] For example, the dynamics of enzyme-induced looping of ssDNA has been studied by FRET.[17] Since the advanced techniques enable the fluorescence microscopy to be carried at the single-molecule level. Single-molecule FRET has been a powerful approach for studying the conformational dynamics of biomolecules.[18–21] However, FRET is well-suited for observing the conformational dynamics of biomolecules on the nanometer scale.[22] When the conformational change at the subnanometer scale is required, other methods complementary to FRET are expected. Sunney *et al*. have used electron transfer (ET)-based quenching of fluorescence for studying protein conformational dynamics for a single molecule.[22] Nonetheless, as mentioned above, this method is not suitable when the conformational dynamics of biomolecules occurs at a longer timescale than the fluorescence lifetime. Hence, it is significant to explore other methods that are effective when the conformational dynamics of biomolecules is linked with the change within the subnanometer range, and when the dynamics takes place at a long timescale.

In this dissertation, the author aimed to address the problem of the hydrophobicity of Py

when using it for studying the looping dynamics of oligonucleotides by proposing and preparing a water-soluble derivative of Py. The application of this water-soluble Py derivative to the studies of dynamics and photoregulation of oligonucleotide looping under physiological conditions was investigated. At the same time, the author aimed to explore a triplet blinking-based method that can be used for studying the conformational dynamics of biomolecules at a long timescale on the subnanometer scale at the single-molecule level.

This dissertation consists of three chapters, as shown below.

In Chapter 1, water-soluble Py derivative, sulfonated pyrene (**SPy**), was synthesized. Its structure was identified by NMR. Its time-resolved absorption was studied using pulse radiolysis and laser flash photolysis. The intermolecular formation rate of **SPy** dimer radical cation ($\mathbf{SPy_2^{\bullet+}}$) was revealed by using laser flash photolysis. By attaching two **SPy** molecules at both ends of ssDNA, the looping dynamics of ssDNA modified by **SPy** was studied using laser flash photolysis.

In Chapter 2, the dynamics of single-stranded RNA (ssRNA) was studied using **SPy** and the same method as Chapter 1. A comparison of looping dynamics between ssRNA and ssDNA was made and discussed.

In Chapter 3, control of the triplet blinking of ATTO 647N by using 1,3,5,7-cyclooctatetraene (COT) as a triplet acceptor was explored using fluorescence correlation spectroscopy (FCS). Applications of COT-controlled triplet blinking of ATTO 647N to the studies of ssDNA looping dynamics and miRNA detection were carried out.

References

[1] D. Balchin, M. Hayer-Hartl, F. U. Hartl, *Science* **2016**, *353*, aac4354.

[2] R. Nussinov, C.-J. Tsai, *Cell* **2013**, *153*, 293–305.

[3] S. Nagashima, T. Tokuyama, R. Yonashiro, R. Inatome, S. Yanagi, *J. Biochem.* **2014**, *155*, 273–279.

[4] J. T. P. Yeeles, K. van Aelst, M. S. Dillingham, F. Moreno-Herrero, *Mol. Cell* **2011**, *42*, 806–816.

[5] E. Harrison, *"The Versatility of RNA."Operators and Promoters: The Story of Molecular Biology and Its Creators*, University Of California Press, Berkeley, **2001,** p. 218.

[6] M. R. Singleton, M. S. Dillingham, D. B. Wigley, *Annu. Rev. Biochem.* **2007**, *76*, 23–50.

[7] K. Y. Paek, K. Y. Hong, I. Ryu, S. M. Park, S. J. Keum, O. S. Kwon, S. K. Jang, *Proc. Natl. Acad. Sci. USA* **2015**, *112*, 1041–1046.

[8] T. Uzawa, R. R. Cheng, K. J. Cash, D. E. Makarov, K. W. Plaxco, *Biophys. J.* **2009**, *97*, 205–210.

[9] T. Uzawa, T. Isoshima, Y. Ito, K. Ishimori, D. E. Makarov, K. W. Plaxco, *Biophys. J.* **2013**, *104*, 2485–2492.

[10] X. Wang, W. M. Nau, *J. Am. Chem. Soc.* **2004**, *126*, 808–813.

[11] L. J. Lapidus, W. A. Eaton, J. Hofrichter, *Proc. Natl. Acad. Sci. USA* **2000**, *97*, 7220–7225.

[12] R. R. Hudgins, F. Huang, G. Gramlich, W. M. Nau, *J. Am. Chem. Soc.* **2002**, *124*, 556–564.

[13] R. Lomoth, T. Häupl, O. Johansson, L. Hammarström, *Chem. Eur. J.* **2002**, *8*, 102–110.

[14] K. Kawai, H. Yoshida, A. Sugimoto, M. Fujitsuka, T. Majima, *J. Am. Chem. Soc.* **2005**, *127*, 13232–13237.

[15] J. Duhamel, *Langmuir* **2012**, *28*, 6527–6538.

[16] J. Vogelsang, C. Steinhauer, C. Forthmann, I. H. Stein, B. Person-Skegro, T. Cordes, P. Tinnefeld, *ChemPhysChem* **2010**, *11*, 2475–2490.

[17] D. Rutkauskas, M. Petkelyte, P. Naujalis, G. Sasnauskas, G. Tamulaitis, M. Zaremba, V. Siksnys, *J. Phys. Chem. B* **2014**, *118*, 8575–8582.

[18] R. Lamichhane, G. M. Daubner, J. Thomas-Crusells, S. D. Auweter, C. Manatschal, K. S. Austin, O. Valniuk, F. H.-T. Allain, D. Rueda, *Proc. Natl. Acad. Sci. USA* **2010**, *107*, 4105–4110.

[19] R. Zhao, D. Rueda, *Methods* **2009**, *49*, 112–117.

[20] G. Bokinsky, D. Rueda, V. K. Misra, M. M. Rhodes, A. Gordus, H. P. Babcock, N. G. Walter, X. Zhuang, *Proc. Natl. Acad. Sci. USA* **2003**, *100*, 9302–9307.

[21] A. Gansen, A. R. Hieb, V. Böhm, K. Tóth, J. Langowski, *PLoS One* **2013**, *8*, e57018.

[22] H. Yang, G. Luo, P. Karnchanaphanurach, T.-M. Louie, I. Rech, S. Cova, L. Xun, X. S. Xie, *Science* **2003**, *302*, 262–266.

Chapter 1 Sulfonated Pyrene as Both a Probe and a Photoregulator for Single-Stranded DNA Looping

Abstract

Controlling the conformation and function of biomolecules through photoregulators holds great promise as a spatiotemporally controllable tool for disease control. In addition, introducing photoregulators into biomolecules has also found applications in constructing smart nanomaterials. In spite of the astonishing advances that have been made in the past few years, realizing highly controllable and efficient regulation over the conformation and function of biomolecules under physiological conditions is still challenging. Herein, sulfonated pyrene, **SPy**, was synthesized and used as a photoregulator to control the looping of single-stranded DNAs (ssDNAs) in aqueous solution. Due to its water solubility, **SPy** merits use in the study of biomolecules in aqueous solution. The looping of the doubly **SPy**-modified ssDNAs is stimulated by irradiation and regulated by **SPy**. Photoionization generates the radical cation of **SPy** (**SPy**$^{\bullet+}$). The association of **SPy**$^{\bullet+}$ with its neutral counterpart, **SPy**, gives rise to the dimer radical cation of **SPy** (**SPy**$_2^{\bullet+}$). During the association process, the stabilization energy released to form **SPy**$_2^{\bullet+}$ provides a driving force for the looping of ssDNAs. Conversely, the formed loop conformations were trapped by the formation of **SPy**$_2^{\bullet+}$, and this allows the looping dynamics to be investigated. The results shown herein suggest the potential of **SPy** as a photoregulator for controlling the conformation and function of biomolecules under physiological conditions.

Introduction

Biomolecules such as proteins, polypeptides, and nucleic acids, have several common characteristics. They all exhibit a fundamental relationship between their conformations and functions, and they all have transient conformations that are dependent on time and the surrounding environment. Using external stimuli to regulate the conformations and thereby the functions of biomolecules could provide a way to explore cellular processes in addition to providing insight into the progression and control of various diseases,[1] which is of growing importance in pharmacological studies.[2] Photostimulation has an important advantage over other external stimuli, because it allows spatial and temporal control,[1–7] which are well suited to the

spatiotemporal characteristics of the activities of biomolecules.[8] Therefore, photostimulation has garnered increasing attention as a highly controllable tool for the spatiotemporal regulation of biomolecules.

Over the past several decades, various photoregulators for regulating the conformation and function of biomolecules have been developed.[1,4–9] One major strategy to introduce the photosensitive component into biomolecules is caging a key functional group of biomolecules by a photosensitive protecting group (caging group). The caged biomolecules are active only if the caging group is removed by photoirradiation.[3,6] Once the biomolecules are uncaged, they remain active. This irreversible strategy has been exploited by using caging groups such as ortho-nitrobenzyl and its derivatives to protect the functional groups of proteins, peptides, nucleic acids, small molecules, and so on.[3,6] On the other hand, another strategy of introducing molecular photoswitches into biomolecules is reversible. This strategy is based on the two distinct structures of the molecular photoswitch introduced into the biomolecules (*trans* and *cis* isomers for isomerization; closed and open forms for electrocyclic interconversion).[1] The predominant structure of the molecular photoswitch introduced into biomolecules is controlled by photoirradiation. On photoirradiation, the molecular photoswitch switches or interconverts between the two distinct structures with changes in geometry, rigidity, dipole moment, and other properties.[1,4] The changes occurring in the molecular photoswitches induce conformational changes occurring in the biomolecules. Introducing molecular photoswitches into biomolecules permits reversible photochemistry and highly regulated on/off cycles corresponding to the dynamic activation and deactivation of biological processes.[8]

The most extensively studied and widely used molecular photoswitches by far are azobenzene and its derivatives (hereinafter azobenzenes), which undergo *cis*-*trans* photoisomerization. The use of azobenzenes as molecular photoswitches for biological applications can be traced back to the pioneering work of Yamana *et al*., who employed azobenzene as a photoisomerizable linker to connect two oligonucleotide segments.[10] Following this pioneering work, Asanuma, Komiyama, and co-workers reported the control of DNA or RNA hybridization and gene expression by using azobenzene as a molecular photoswitch.[2,11–17] The utility of azobenzenes for photoregulating the conformation and function of peptides[18–22] and proteins,[23] photocontrolling ion channels,[24,25] and photorestoring human vision have also been

reported.[9,26] The main reasons for the wide use of azobenzenes as photoswitches in biological applications are their easy synthesis, relatively high photostationary states and quantum yields, fast photoisomerization, and low rate of photobleaching.[1] However, it has been reported that solvent, temperature, and substituent effects have a notable impact on the photoisomerization rate, the photostationary state, and quantum yields, as well as the *cis*-to-*trans* thermal isomerization rate of azobenzene-based molecular photoswitches.[1,5] There are two types of photoswitches: photochemically reversible (p-type) and thermally reversible (t-type) photoswitches; the two types are different but not mutually exclusive.[9] P-type photoswitches are defined as being driven by absorption of light, while t-type photoswitches can thermally relax back to their lower-energy isomer over time.[9] In fact, the p-type and t-type processes coexist in many photoswitches. For azobenzenes, the thermal *cis*-to-*trans* relaxation rate varies with the substituent, solvent, and temperature, on orders of magnitude from milliseconds to days.[5,9,27] The preferred thermal relaxation rate will depend on the application.[9,28] In addition, the fact that azobenzenes undergo reduction under physiological conditions in vivo may limit their use in certain applications.[1]

By virtue of the prominent feature of controllable switching when using molecular photoswitches, photoregulating the conformation and functions of biomolecules has been developing over the past decades with astonishing results; this field is playing an important role in the elucidation of cellular processes, the clarification of disease progression, and most importantly, the potential control of these processes.[1,9,29] Additionally, introducing molecular photoswitches into biomolecules has been an inspiring approach for the construction of smart biomolecule-based nanomaterials.[30–33] In spite of the many advances achieved in the past decades, high controllability and efficiency, and eligibility for physiological applications remain significant problems. This has inspired various groups to explore novel photoregulating approaches in the hope of mimicking the natural molecular motors observed in living organisms.[28,34–36] Because most photoswitching molecules are hydrophobic, a main challenge for photoregulating the conformation and function of biomolecules under physiological conditions is the design of water-soluble photoregulators.[35]

Pyrene (Py) is one of the most commonly used photosensitive probes; indeed, it is referred to as “the fruit fly of photochemists”.[37] Since its discovery in 1837 by Laurent,[37,38] Py has attracted considerable attention[37,39–42] and become one of the most studied organic molecules

because of its distinctive photophysical properties.[37] Py can form an excimer with high fluorescence quantum yields, long-lived excited state, and resolvable fluorescence bands relative to the monomer.[37,43] The formation of Py excimer is exceptionally sensitive to the surrounding microenvironment, making Py a gold probe of microenvironmental change.[37] Hence, and owing to its chemical stability and charge-carrier mobility, Py and its derivatives (Pys) have been widely used for studying the assembly, conformation, and dynamics of macromolecules and supramolecular assemblies of varied size, composition, and architecture.[39,44–54] In most cases, techniques involving the processes of fluorescence resonance energy transfer (FRET),[54–57] or changes in fluorescence (intensity and/or lifetime) from the singlet excited state of monomer ($^1Py^*$) and excimer ($^1Py_2^*$), were employed.[39,42,49–51,58,59] The above-mentioned techniques are dependent on the photophysical properties of $^1Py^*$ and $^1Py_2^*$, the lifetimes of which are reported to be around 400 ns (680 ns was also reported[60]) and 60 ns (90 ns was also reported[60]) in deoxygenated cyclohexane, respectively.[61–63] Distinct from these techniques, in our previous works, we reported using the formation of the Py dimer radical cation ($Py_2^{\bullet+}$) to explore the conformation and dynamical information of transiently formed double-stranded DNAs (dsDNAs) and the end-to-end collision dynamics of single-stranded DNAs (ssDNAs).[44,47,48] The results showed that, in stark contrast to using $^1Py^*$ and $^1Py_2^*$, the approach of forming $Py_2^{\bullet+}$ enables kinetics study over a much wider time window ranging from 10 ns to 1 ms.[44,47,48] $Py_2^{\bullet+}$ is produced owing to the association of Py radical cation ($Py^{\bullet+}$) generated after one-electron oxidation of Py with its neutral counterpart (Py), which features a diagnostic charge resonance absorption band of about 1300–1700 nm in the near-infrared (NIR) region. Compared with $^1Py^*$ and $^1Py_2^*$, the much longer lifetimes of $Py^{\bullet+}$ and $Py_2^{\bullet+}$ in the time range of 0.1–100 μs (measured in organic solvents)[63–65] allows the observation of $Py_2^{\bullet+}$ formation in doubly Py-modified biomolecules over a long timescale.[44,47,48] Thus, the method of observing $Py_2^{\bullet+}$ formation is a better choice compared with using $^1Py^*$ and $^1Py_2^*$, as well as the excited states of other fluorescent probes with short excited-state lifetimes, when the events of biomolecules occur at comparable rates to the decay of the excited states.[66]

The method of observing $Py_2^{\bullet+}$ formation provides a way to trace not only information about the surrounding environment of the Py probes introduced into the biomolecules but also the conformational dynamics of the biomolecules by trapping the transient conformations of biomolecules formed after transformation from one state to another.[44,47,48] In our previous works,

by introducing one Py at the 5'-end of one DNA strand and another Py near the 3'-end of the complementary DNA strand,[44] by introducing two Pys in the internal sites of two DNA strands,[47] or by introducing two Pys at the 5'-end and 3'-end positions of ssDNAs,[48] we found that: 1) the $Py_2^{\bullet+}$ formation rate reflects the end fraying of duplex dsDNAs,[44] the kinetics of internal sites in duplex dsDNAs,[47] and the end-to-end contact dynamics of ssDNAs,[48] and 2) the transient states of DNAs transformed from the initial states are trapped by $Py_2^{\bullet+}$, and this phenomenon reveals the conformation dynamical information.[48] These findings indicate that the transiently formed DNA conformations can be trapped by $Py_2^{\bullet+}$. At the same time, they provide hints regarding the potential regulating impact of the hydrophobic Py on the conformational transition of DNAs, which let us consider whether it would be possible to use Py to photoregulate the conformation and function of biomolecules. With this in mind, and taking the necessity of water solubility into consideration, in the present work we designed and synthesized a water-soluble Py derivative, namely sulfonated pyrene (**SPy**, Scheme 1-1), and introduced it at both the 5'-end and 3'-end positions of ssDNAs. The reason to choose **SPy** lies in the facts that, on one hand, sulfonic acid is a strong acid and **SPy** would dissociate into ions under physiological conditions, and on the other hand, the electrostatic repulsion between the negatively charged **SPy** and the phosphate group in ssDNA would avoid the potentially unwanted effects on the conformation of ssDNA, which would be otherwise induced when using positively charged Pys. The kinetics of the photostimulated and **SPy**-regulated looping of ssDNAs was studied by trapping the transiently formed loop conformation with the dimer radical cation of **SPy** ($\mathbf{SPy_2^{\bullet+}}$). After photoirradiation, the radical cation of **SPy** ($\mathbf{SPy^{\bullet+}}$) was first generated by a two-photon ionization process. Then, concomitant with the decay of $\mathbf{SPy^{\bullet+}}$, $\mathbf{SPy_2^{\bullet+}}$ arose through the association of the $\mathbf{SPy^{\bullet+}}$ located at one end of the ssDNA molecule with the unoxidized **SPy** located at the other end of the same molecule. The association kinetics is dependent on the looping dynamics of the ssDNAs and offers a concomitant propelling force for the looping of ssDNAs because of the stabilization energy to form $\mathbf{SPy_2^{\bullet+}}$.[67,68] Herein, the water-soluble **SPy** provides a possible solution to the major obstacle impeding the use of Py under physiological conditions. By observing $\mathbf{SPy_2^{\bullet+}}$ formation in aqueous solution, we can study the internal dynamics of biomolecules over a wider time window than when using $^1Py^*$ and $^1Py_2^*$ or the singlet excited states of other fluorescent probes with short excited-state lifetimes. The regulation of ssDNA looping by **SPy** under photoirradiation in aqueous solution may foreshadow **SPy** as a new photoregulator for controlling the conformation and function of biomolecules.

Results and Discussion

Although Py has been widely used as a light-sensitive probe for exploring the conformation, dynamics, flexibility, and assembly of macromolecules and supramolecules, one impediment to its further application is its insolubility in water, since most biomolecules are water-soluble.[42] Therefore, a water-soluble Py is highly desired. Herein, a water-soluble derivative of Py, namely **SPy**, was synthesized and used as probe and photoregulator. The sulfonation of 1-pyrenebutyric acid (PyBA) by chlorosulfonic acid gave the sulfonated Py, **SPy**, with a yield of 15% (Scheme 1-1). In addition to the **SPy** shown in Scheme 1-1 (Product 3 in Figure 1-1), some other byproducts were also produced after the sulfonation (Figure 1-1), of which the two main byproducts (Products 4 and 5 in Figure 1-1) are potentially positional isomers of **SPy**. To gain knowledge about the formation efficiency of the corresponding dimer radical cations of the three main products, pulse radiolysis measurements were carried out for each main product (Scheme 1-2 and Figure 1-2). It was found that the **SPy** shown in Scheme 1-1 has the highest efficiency to form the dimer radical cation (Figure 1-2). Therefore, we chose Product 3 to use as the **SPy**, and characterized its structure by NMR spectroscopy (Appendix), as shown in Scheme 1-1. The activation of **SPy** with N-hydroxysuccinimide (NHS) generated the reactive ester derivative, **SPy**-NHS. Finally, coupling of **SPy**-NHS with the amino groups at the 5'-end and 3'-end of ssDNAs afforded the doubly **SPy**-modified ssDNA, **SPy-ssDNA-SPy** (Scheme 1-1). The coupling efficiency for longer ssDNA is reduced in comparison with the shorter sequence. The UV-vis absorption and fluorescence spectra of **SPy** are shown in Figure 1-3, along with the spectra of PyBA. Compared with Py, the absorption bands of **SPy** show a redshift, which is especially obvious in the band corresponding to the $S_0 \rightarrow S_2$ transition (redshift of 14 nm). The synthesis of **SPy** herein provides an effective and universal way to avoid or reduce the barrier caused by the hydrophobicity of Py when it is utilized under physiological aqueous conditions.

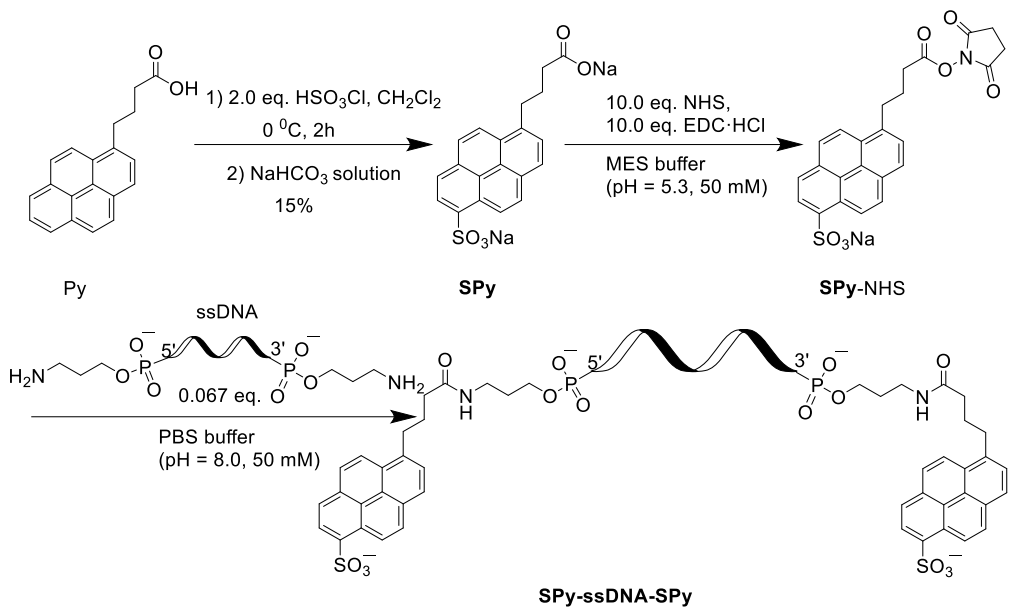

Scheme 1-1. Synthetic scheme of **SPy**, **SPy**-NHS, and **SPy-ssDNA-SPy**.

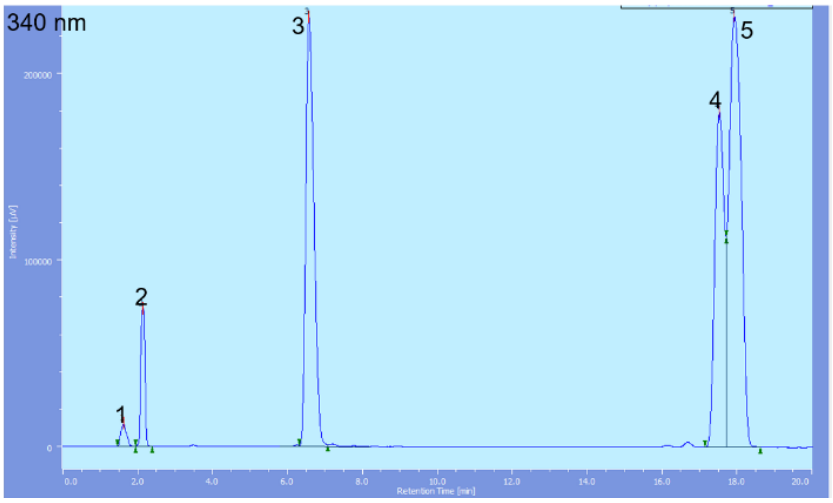

Figure 1-1. HPLC chromatogram of the crude products. Product 2 is probably a doubly sulfonate-substituted pyrene. Product 3 is identified as **SPy** as shown in Scheme 1-1 by NMR (Appendix). Product 4 and product 5 are potentially positional isomers of product 3. The HPLC settings are provided in Table 1-2 in the experimental section.

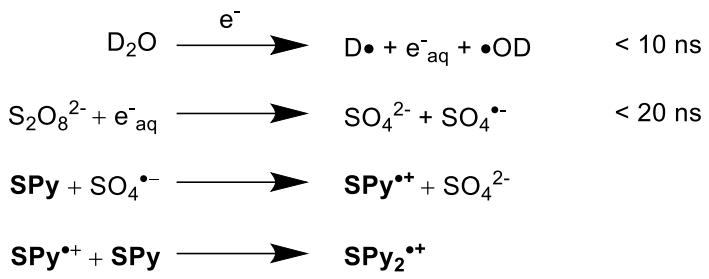

Scheme 1-2. The pulse radiolysis process of **SPy**.

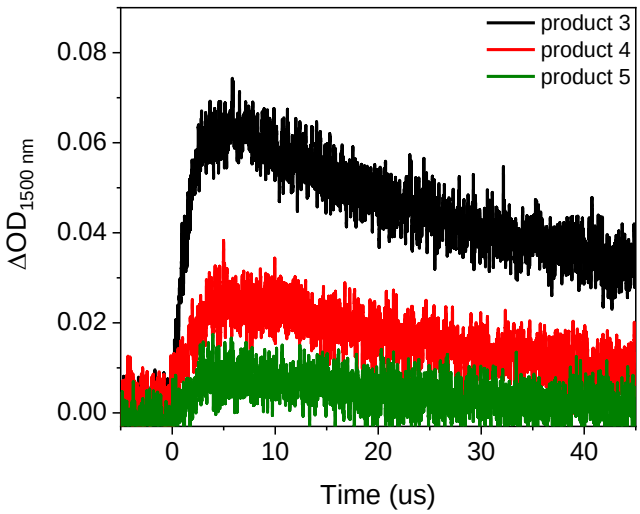

Figure 1-2. Time profiles of the transient absorption of the dimer radical cation of each main product (product 3-5 in Figure 1-1) monitored at 1500 nm during the pulse radiolysis. The sample solution contained 0.1 mM product, 10 mM $Na_2S_2O_8$, and 10 mM *t*-BuOH in 10 mM sodium phosphate buffer solution (pD 7). The sample solution was purged with Ar before the measurement. Product 3 shows the highest efficiency to form a dimer radical cation, and, therefore, was used as **SPy**.

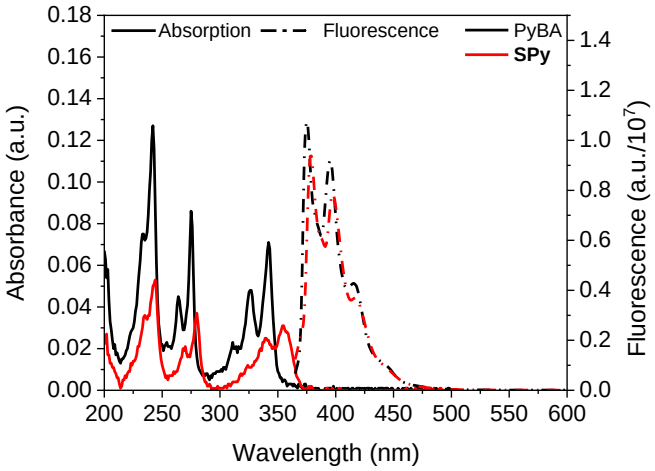

Figure 1-3. The UV-vis absorption and fluorescence spectra of PyBA and **SPy**. PyBA was measured in KCl/NaOH buffer solution (pH 13.0). **SPy** was measured in sodium phosphate buffer solution (10 mM, pH 7.0).

The oxidation of **SPy** to **SPy**$^{\bullet+}$ by two-photon ionization and the intermolecular **SPy**$_2^{\bullet+}$ formation were studied using laser flash photolysis, as shown in Scheme 1-3. Figure 1-4 shows the transient absorption spectra during the laser flash photolysis of **SPy**. The absorption of solvated electron (e_{aq}^-) was observed immediately after excitation by a 355 nm laser pulse, located at 550-650 nm in Figure 1-4A. Then the absorption featuring two main peaks at 460 nm and 470 nm and two weak peaks at 431 nm and 490–495 nm was observed and was assigned to the absorption of **SPy**$^{\bullet+}$ (Figure 1-4A).[69] The absorption showed a decay with a rate constant of (8.8 ± 0.03) × 10^4 s^{-1} (Figures 1-4A, C). Concomitantly, a band with absorption at 1400–1700 nm emerged with a rate constant of (9.3 ± 0.3) × 10^4 s^{-1} (Figures 1-4B, C). This absorption band in the NIR region was assigned to the charge resonance band of **SPy**$_2^{\bullet+}$, which originates from the intermolecular collision of **SPy**$^{\bullet+}$ and **SPy**. The transient absorption spectra of **SPy** recorded during the pulse radiolysis showed the same absorption characteristics of e_{aq}^-, **SPy**$^{\bullet+}$ and **SPy**$_2^{\bullet+}$ (Figure 1-5). By measuring the concentration dependence of the intermolecular **SPy**$^{2\bullet+}$ formation rate in the range of 0–100 μM, the rate was found to be proportional to the concentration of **SPy** (Figure 1-6). The biomolecular rate constant was calculated to be (1.8 ± 0.09) × 10^9 $M^{-1}s^{-1}$ at room temperature in N_2O-saturated sodium phosphate buffer solution (pD 7.0), in the same order of magnitude as the diffusion-controlled limit.

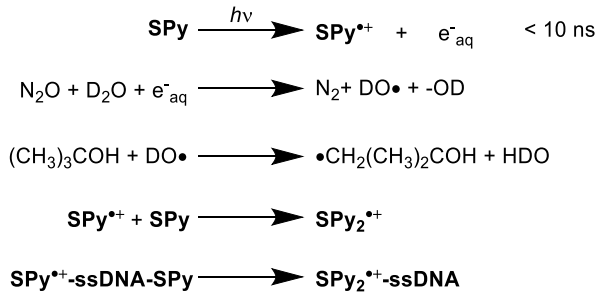

Scheme 1-3. The laser flash photolysis process of **SPy** and **SPy-ssDNA-SPy**.

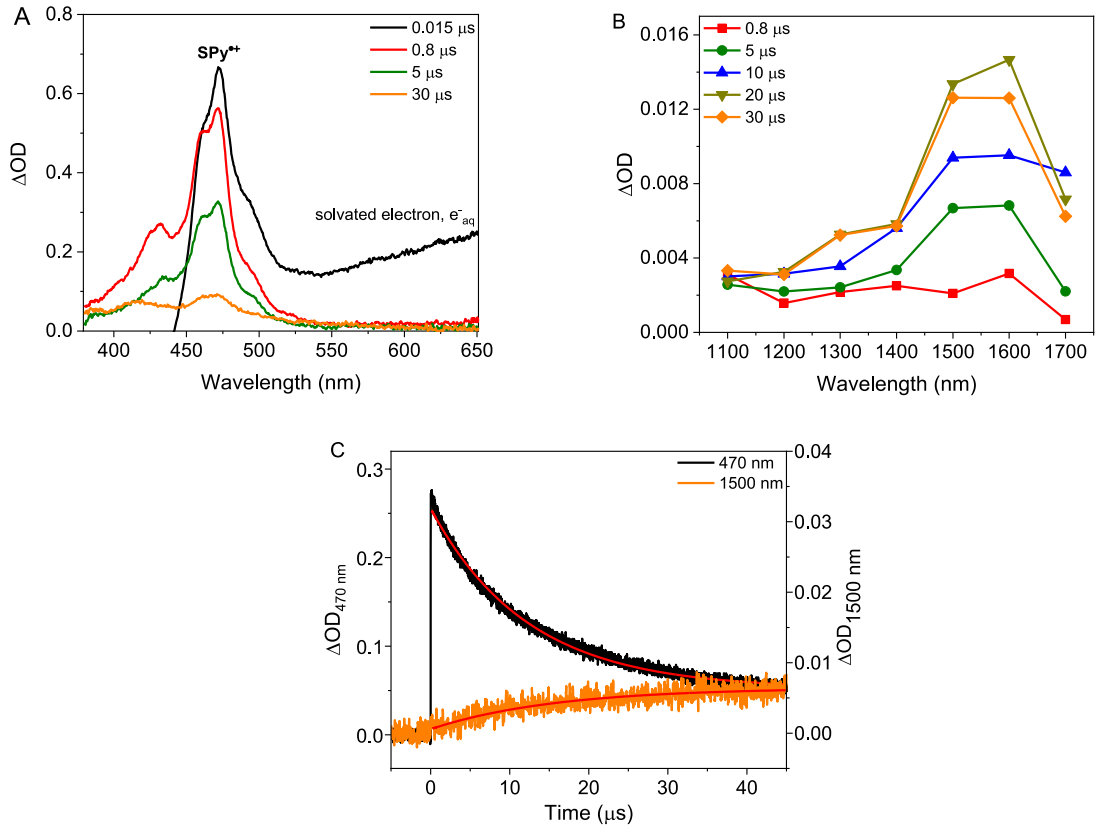

Figure 1-4. The transient absorption spectra observed during the laser flash photolysis of **SPy** in (A) the visible range at 0.015, 0.8, 5, and 30 µs; and (B) the NIR region at 0.8, 5, 10, 20, and 30 µs. (C) Time profiles of the transient absorption of $\mathbf{SPy}^{\bullet+}$ and $\mathbf{SPy_2}^{\bullet+}$ monitored at 470 nm and 1500 nm, respectively, during the laser flash photolysis of **SPy**. The solid red line is a single-phase exponential fit to the experimental time profiles. The sample solution contained 40 µM **SPy** and 10 mM *t*-BuOH in 10 mM sodium phosphate buffer solution (pD 7.0). The sample solution was purged with N_2O. A 380-nm long-pass filter was used for the visible range, and an 850-nm filter was used for the NIR region.

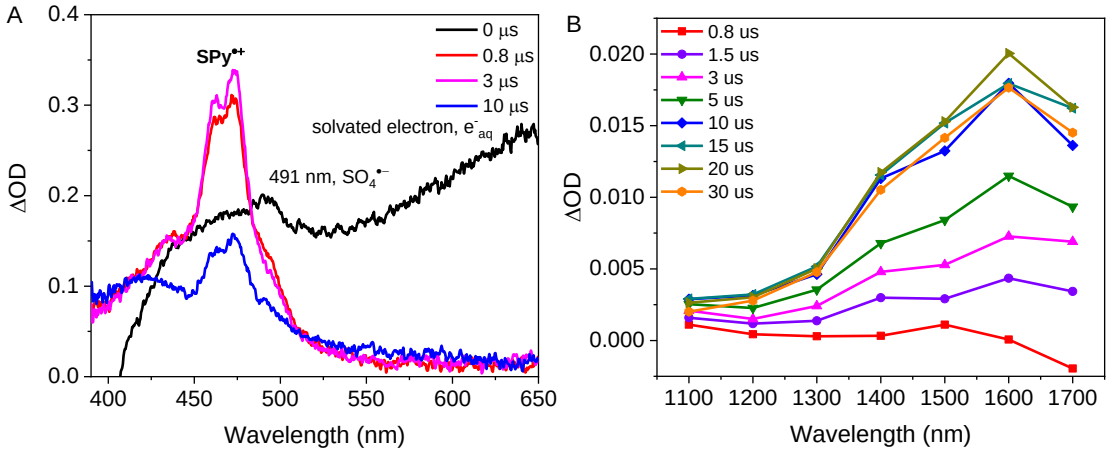

Figure 1-5. The transient absorption spectra observed during the pulse radiolysis of **SPy** in (A) visible range at 0, 0.8, 3, and 10 µs; (B) NIR region at 0.8, 1.5, 3, 5, 10, 15, 20, and 30 µs. The sample solution contained 80 µM **SPy**, 10 mM $Na_2S_2O_8$, and 20 mM *t*-BuOH in 10 mM sodium phosphate buffer solution (pD 7). The sample solution was purged with Ar before the measurement. A 380-nm long-pass filter was used for the visible-range measurement, and an 850-nm filter was used for the NIR region.

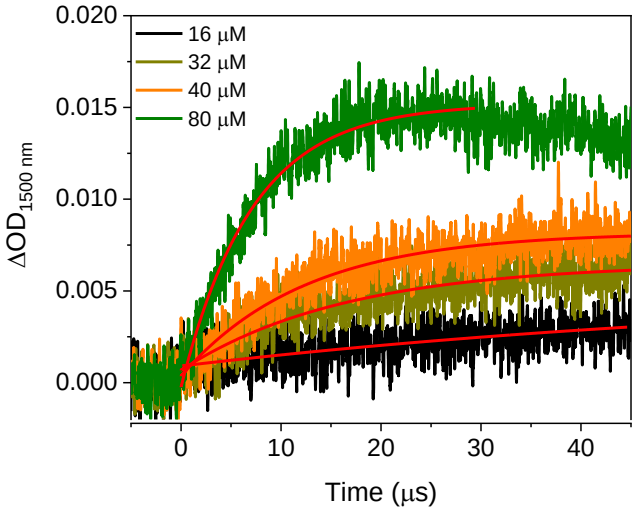

Figure 1-6. Time profiles of the transient absorption of $\mathbf{SPy_2}^{\bullet+}$ monitored at 1500 nm during the laser flash photolysis of **SPy** at four different concentrations, 16 µM, 32 µM, 40 µM, and 80 µM. The solid red line is a single-phase exponential fit to the experimental time profiles. The sample solution contained **SPy** and 10 mM *t*-BuOH in 10 mM sodium phosphate buffer solution (pD 7.0). The sample solution was purged with N_2O before the measurement.

To gain insight into the conformation of the doubly **SPy**-modified ssDNA prior to the photoionization of the end-linked **SPy**, the steady-state absorption and fluorescence spectra were examined. The absorption spectra (Figures 1-7A and B) showed the sum of the characteristic absorption bands of DNA and **SPy**. It is worth noting that, in comparison with the characteristic absorption bands of the intact **SPy**, the absorption bands after introducing **SPys** into ssDNA show a redshift, especially the band corresponding to the $S_0 \rightarrow S_2$ transition (redshift of 5 nm), which suggest that a π-stacking interaction takes place between **SPy** and the constituent bases of the ssDNA. For both A-composed ssDNAs and T-composed ssDNAs, the absorption contribution from the nucleobases increases as the length of the ssDNA increases. In the fluorescence spectra (Figures 1-7A and B), excimer emission was observed for **SPy-A$_4$-SPy** (Figure 1-7A), **SPy-T$_4$-SPy**, and **SPy-T$_8$-SPy** (Figure 1-7B); this occurred from the intramolecular excimer (^{1}**SPy$_2^*$**). It should be pointed out that the intramolecular excimer (^{1}**SPy$_2^*$**) can be formed by two processes when two **SPys** are end-linked to ssDNA: 1) excitation of the non-oxidized cofacial **SPy** dimer (the ground state dimer); 2) the dynamical formation by the excited state of **SPy** (^{1}**SPy***) associating with its neutral counterpart (**SPy**) within the short lifetime of ^{1}**SPy***.[48,61–63] The population of the ground-state conformation of the doubly **SPy**-modified ssDNA with the two end-linked **SPys** forming a non-oxidized cofacial **SPy** dimer can be deciphered through the absorbance ratio of the absorption band at 345 nm ($14A_g$ transition of $S_0 \rightarrow S_2$) to the absorption band at 360 nm (0–0 transition of $S_0 \rightarrow S_2$).[70,71] In the case of **SPy-T$_4$-SPy**, the ratio exceeds unity, suggesting that a large population of **SPy-T$_4$-SPy** molecules are in such a ground-state conformation with the two end-linked **SPys** in cofacial contact in the non-oxidized state. As the ssDNA length increases from 4 to 8, the population decreases (Figure 1-7B), and finally becomes minuscule for **SPy-T$_{16}$-SPy**. This non-oxidized cofacial **SPy** dimer would generate **SPy$_2^{\bullet+}$** immediately after two-photon ionization.

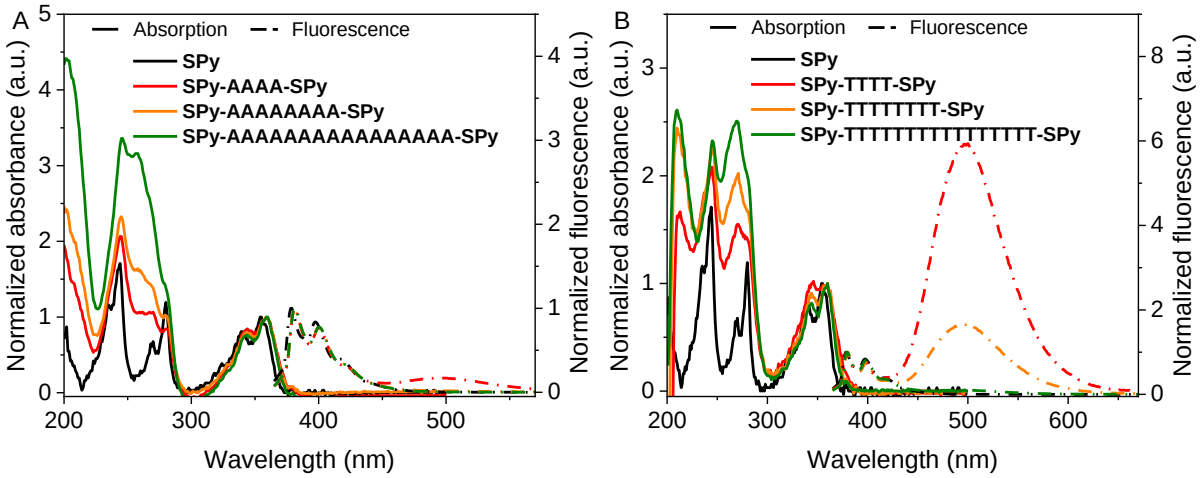

Figure 1-7. UV-vis absorption and fluorescence spectra of doubly **SPy**-modified ssDNAs. (A) **SPy-A$_n$-SPy**; (B) **SPy-T$_n$-SPy**, n = 4, 8, and 16. The fluorescence spectra were measured with excitation at 345 nm. The sample solution contained 1 μM **SPy-ssDNA-SPy** in 10 mM sodium phosphate buffer solution (pH 7.0).

Next, the regulation of ssDNA looping by two end-linked **SPys** under photoirradiation was studied by laser flash photolysis (Scheme 1-3). By exponential fitting to the time profiles in Figure 1-8, the formation rate of **SPy$_2^{\bullet+}$**, k(**SPy$_2^{\bullet+}$**), was determined (Table 1-1). Unlike in the case of the intact **SPy** monomer, the formation of **SPy$_2^{\bullet+}$** for **SPy**-modified ssDNA is an intramolecular collision process at the specified concentration herein, as shown in Scheme 1-3. This was validated by the independence of k(**SPy$_2^{\bullet+}$**) from the concentration of **SPy-A$_8$-SPy**, recorded at 20 μM and 40 μM (Figure 1-9 and Table 1-1), and by the finding that the **SPy$_2^{\bullet+}$** formation rate for the doubly **SPy**-modified ssDNA (Figure 1-8 and Table 1-1) was much faster than that for the intact **SPy** monomer.

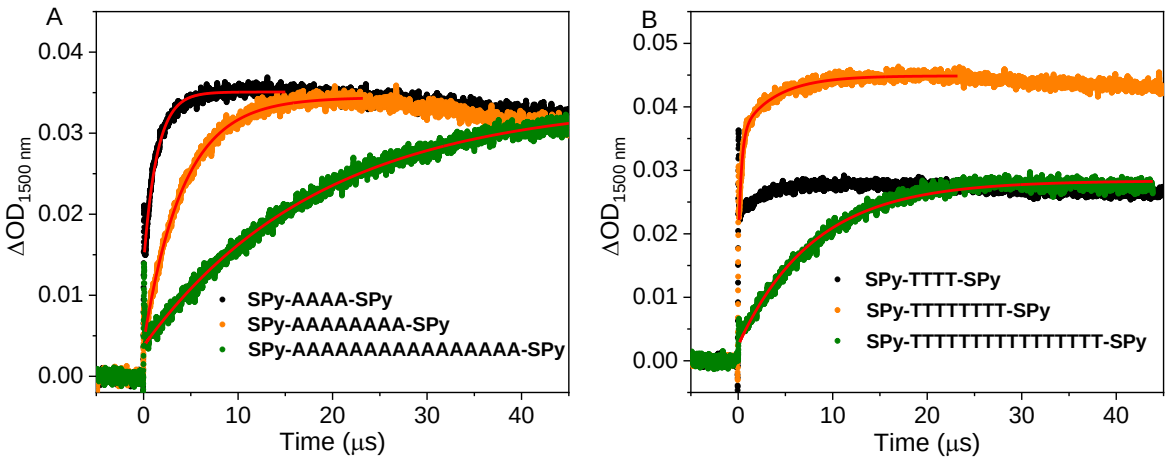

Figure 1-8. Time profiles of the transient absorption of $\mathbf{SPy_2^{\bullet+}}$ monitored at 1500 nm during the laser flash photolysis of **SPy-ssDNA-SPy**. (A) **SPy-A$_n$-SPy**; (B) **SPy-T$_n$-SPy**, n = 4, 8, and 16. The solid red line is a single-phase (for all sequences except **SPy-T$_8$-SPy**) or two-phase exponential (for **SPy-T$_8$-SPy**) fit to the experimental time profiles. The sample solution contained 40 μM **SPy-ssDNA-SPy** and 10 mM *t*-BuOH in 10 mM sodium phosphate buffer solution (pD 7.0). The sample solution was N_2O-purged.

Table 1-1. Loop formation rate ($k_{looping}$) and the population of immediately formed $\mathbf{SPy_2^{\bullet+}}$, P_{static}(%)[a]

SPy-ssDNA-SPy	C (μM)	1500 nm $k_{looping}$ (10^6 s^{-1})	P_{static} (%)[a]
SPy-A$_4$-SPy	40	0.73 ± 0.004	42
SPy-A$_8$-SPy	20	0.24 ± 0.002	–
	40	0.24 ± 0.002	–
SPy-A$_{16}$-SPy	40	0.053 ± 0.0001	–

SPy-ssDNA-SPy	C (μM)	1500 nm $k_{1\text{-looping}}$ (10^6 s^{-1})	$k_{2\text{-looping}}$ (10^6 s^{-1})	P_{static} (%)[a]
SPy-T$_4$-SPy	40	–	–	82
SPy-T$_8$-SPy	40	3.1 ± 0.06	0.27 ± 0.003	52
SPy-T$_{16}$-SPy	40	0.13 ± 0.0003		–

[a] Immediately formed $\mathbf{SPy_2^{\bullet+}}$ component P_{static} (%) = $\Delta OD_{t=10\ ns}/\Delta OD_{max}$.

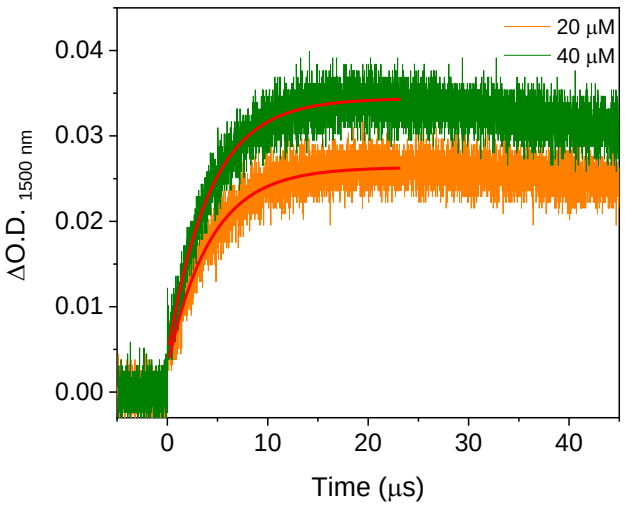

Figure 1-9. Time profiles of the transient absorption of $\mathbf{SPy}^{\bullet+}$ and $\mathbf{SPy_2}^{\bullet+}$ monitored at 1500 nm during the laser flash photolysis of **SPy-(A)$_{16}$-SPy** at different concentrations. The solid red line is a single-phase exponential fit to the experimental time profiles. The sample solution contained 20 μM or 40 μM **SPy-(A)$_{16}$-SPy** and 10 mM *t*-BuOH in 10 mM sodium phosphate buffer solution (pD 7.0). The sample solution was N_2O-purged.

As deduced from the steady-state absorption and fluorescence spectra (Figure 1-7), immediate $\mathbf{SPy_2}^{\bullet+}$ formation within the laser duration was observed for **SPy-A$_4$-SPy**, **SPy-T$_4$-SPy**, and **SPy-T$_8$-SPy**. The contribution of this immediately formed $\mathbf{SPy_2}^{\bullet+}$ component to the totally formed $\mathbf{SPy_2}^{\bullet+}$ after laser irradiation is denoted by P_{static} (%). The large population of the non-oxidized cofacial **SPy** dimer observed for **SPy-T$_4$-SPy**, as shown in Figure 1-7B, makes a significant contribution to $\mathbf{SPy_2}^{\bullet+}$ formation, with a P_{static} (%) around 82%. This is followed by **SPy-T$_8$-SPy**, with P_{static} = 52%, and **SPy-A$_4$-SPy**, with P_{static} = 42%. In addition to the immediately formed $\mathbf{SPy_2}^{\bullet+}$ component, another slower component was detected for **SPy-A$_4$-SPy** (Figure 1-8A), which corresponds to the looping dynamics ($k_{looping}$) of the doubly **SPy**-modified ssDNA composed of four adenosine residues under irradiation.

The $k_{looping}$ value of 0.7×10^6 s^{-1} for **SPy-A$_4$-SPy** is 5.8 times as fast as the end-to-end collision rate of DBO-A$_4$G (DBO, 2,3-diazabicyclo-[2.2.2]-oct-2-ene) reported by Nau *et al.*[72] The difference in the kinetics of A_4 to undergo end-to-end collision probably has its origins in the

sample component and investigation methods. Since the quencher, a purine base of G, was located next to the consecutive A bases in the work of Nau *et al*., base-stacking interaction spans the A_4G unit.[72] In the interaction between the chromophores and DNA base in this work, unlike DBO, because of the aromaticity property of Py, π-stacking interaction takes place between the two end-linked **SPys** and the constituent bases of the ssDNA, as demonstrated by the redshift of the absorption band in Figure 1-7.[73] Both the base-stacking interaction between G and its neighboring base of A in DBO-A_4G and the π-stacking interaction of the end-linked **SPy** or **SPys** with the constituent base of A in **SPy-A_4-SPy** have impacts on the loop-formation kinetics of A_4. A stronger stacking interaction would result in slower kinetics.[72,74] The enthalpy (ΔH) associated with the stacking of G over A in ssDNA was calculated to be -3.76 kcal mol^{-1} (-15.73 kJ mol^{-1}), and the intrastrand stacking energy of deoxynucleotide dimer was reported to be in the range from -5 to -0.5 kcal mol^{-1} (-20.92 to -2.09 kJ mol^{-1}).[75] With regard to the π-stacking interaction of the end-linked **SPy** or **SPys** with the constituent base of A in **SPy-A_4-SPy**, an insight can be gained from the π-stacking interaction energies between phenalenyl radical and DNA base of A, and between acenaphthylene and A. This is because Py is polycyclic aromatic hydrocarbon, like the phenalenyl radical and acenaphthylene. The interaction energies were calculated to be -36.9 kJ mol^{-1} and -36.7 to -34.0 kJ mol^{-1} for phenalenyl radical-A and acenaphthylene-A, respectively. Therefore, the π-stacking interaction of the end-linked **SPy** or **SPys** with the constituent base of A in **SPy-A_4-SPy** should not be weaker than the base-stacking interaction between G and its neighboring A. This suggests that the differences in base component and chromophores in DBO-A_4G and **SPy-A_4-SPy** are most probably not the reason for the observed faster looping kinetics of **SPy-A_4-SPy** compared with DBO-A_4G. Apart from the base component and chromophores, the length of the flexible linker attaching the probes to the ssDNA may also be a factor affecting the kinetics. The linker of ─CH_2─ was used by Nau *et al*. for attaching DBO to ssDNA. In contrast, the longer ─$(CH_2)_3NHCO(CH_2)_3$─ linker was applied herein for attaching **SPys** to ssDNA. In terms of the examination methods, intramolecular fluorescence quenching of DBO by G base was used for the end-to-end collision dynamics of A_4 in the work of Nau *et al*. This quenching follows the hydrogen atom transfer mechanism and occurs when the chromophore of DBO and the quencher of base G come into van der Waals contact distance of 2–3 Å.[72,76] In the case of the formation of $\mathbf{SPy_2^{\bullet+}}$, the $\mathbf{SPy^{\bullet+}}$ generated after oxidation of the **SPy** located at one end of the ssDNA molecule associates with its neutral counterpart, **SPy** located at the other end of the same ssDNA molecule, to form

SPy$_2$ $^{\bullet+}$,[67,68] in which the two **SPy** moieties have a specific interplanar distance within the range of 3.1–3.6 Å.[77–80] This distance is very close to the effective contact distance between the DBO probe and base G when fluorescence quenching occurs. Consequently, the faster looping kinetics observed when using the method of forming **SPy$_2$**$^{\bullet+}$ compared with using fluorescence quenching of DBO by base G does not significantly come down to the difference in the effective contact distance between the probes. In addition to the above-discussed apparent causes, another important cause stemming from the formation mechanism of **SPy$_2$**$^{\bullet+}$ should be emphasized. The intramolecular reaction rate between DBO in the singlet state and its quencher, G, is slower than that between **SPy**$^{\bullet+}$ and **SPy**, because the bimolecular rate constants of the corresponding intermolecular reaction are 5.0×10^8 $M^{-1}s^{-1}$,[72] and $(1.8 \pm 0.09) \times 10^9$ $M^{-1}s^{-1}$, respectively. The faster reaction between **SPy**$^{\bullet+}$ and **SPy** is attributed to the fact that the ground state of **SPy$_2$**$^{\bullet+}$ is more stable than that of the monomeric **SPy**$^{\bullet+}$ in solution.[68] For this reason, there exists the stabilization energy when **SPy**$^{\bullet+}$ associates with its neutral counterpart (**SPy**) to form **SPy$_2$**$^{\bullet+}$[67,68] during the ssDNA looping, which is about -30 to -40 kJ mol^{-1} ($-\Delta H$ = 30–40 kJ mol^{-1}, $-\Delta G$ = 15 kJ mol^{-1} at 20 ℃).[68,81,82] The stabilization energy is close to the stabilization energy of *cis*→*trans* isomerization of azobenzene ($-\Delta H$ = 42–50 kJ mol^{-1}),[83,84] which has been reported to be sufficient to drive substantial conformational change in proteins.[1,84] Additionally, the activation energy of 33 kJ mol^{-1} required for the end-to-end collision of DBO-A$_4$G was determined by Nau *et al*.[72] Therefore, the stabilization energy herein is believed to provide a driving force for the looping of ssDNAs.[72] In other words, **SPy** can act as a regulator driving the looping of ssDNAs under irradiation. Taking all the above-mentioned causes into account, the faster kinetics observed herein could be summarized as the result of synergy between using a flexible linker and the photoregulation effect of **SPy** on the looping dynamics of ssDNAs.

The $k_{looping}$ value showed a clear length dependence on length. For A-constituted ssDNA modified by **SPy** at both ends, $k_{looping}$ decreases by factors of 3 and 13 as the length increases from 4 to 8 and 16, respectively (Table 1-1). This is consistent with our previous observation of the length dependence of 5', 3'-bis (1-butylpyrene)-modified ssDNA (Py-AA$_n$T-Py; n = 1, 4, and7).[48] For T-constituted ssDNA, the length effect is manifested in two ways. 1) The length affects the percentage of the immediately formed **SPy$_2$**$^{\bullet+}$ component generated from the cofacial **SPys** in the non-oxidized state. As the length increases from 4 to 8 and 16, P_{static} is decreased from 82% to 52% and negligible, respectively. 2) The length affects the looping kinetics. For **SPy-T$_4$-SPy**, the

population of such a ground state conformation with cofacially-contacted **SPys** in the non-oxidized state is so high that the immediate component of $\mathbf{SPy_2^{\bullet+}}$ formation dominates the formation of $\mathbf{SPy_2^{\bullet+}}$, so that the formation component resulting from ssDNA looping after irradiation becomes indistinct and unresolvable (Figure 1-8B). When the length is extended to 8, two other components ($k_{1\text{-looping}}$ and $k_{2\text{-looping}}$) were obtained after fitting the time profiles with a two-phase exponential function, in addition to the immediate $\mathbf{SPy_2^{\bullet+}}$-formation component. The fast component, $k_{1\text{-looping}}$, is 12 times as fast as the slower component ($k_{2\text{-looping}}$) (Table 1-1). This result is very similar to that of Py-AT_8-Py reported in our previous work (3.3×10^6 s^{-1} and 0.2×10^6 s^{-1} for the faster and slower component, respectively).[48] Therefore, the present result supports our previous conclusion about the formation of a misfolded conformation during the end-to-end contact of T-rich ssDNA.[48] As the length further increased to 16, only a single component was observed, and k_{looping} was 29 times slower than the fast component of **SPy-T_8-SPy**, and 2.5 times slower than the slower component of **SPy-T_8-SPy**. Since the possibility of forming misfolded conformations increases as the length of ssDNA increases, it is believed that misfolded conformations were significantly formed during the looping of **SPy-T_{16}-SPy**, causing inefficient contacts and impeding the looping kinetics, as suggested by Ansari *et al*.[85–87] Comparison of the looping dynamics of the doubly **SPy**-modified ssDNA between A-composed strand and T-composed strand, such as **SPy-A_{16}-SPy** and **SPy-T_{16}-SPy**, reveals that the loop formation occurs on a longer time scale for the A-composed strand (Table 1-1). This can be explained by the higher rigidity (base-stacking interactions) of A-composed ssDNA compared to T-composed ssDNA.[48,74] This dependence of the looping rate on the kind of nucleotide in ssDNA is in line with the results observed by Nau *et al*.[72]

The stabilization energy released to form $\mathbf{SPy_2^{\bullet+}}$ provides a driving force for the ssDNA looping; conversely, the formed ssDNA loop is trapped by the formation of $\mathbf{SPy_2^{\bullet+}}$. This permits the investigation of the loop-formation dynamics of the doubly **SPy**-modified ssDNA regulated by **SPy** and stimulated by irradiation. Apart from this, the method of utilizing **SPy** as a photoregulator for regulating the looping of ssDNAs holds promise for the goal of achieving reversible regulation. There are two reasonable pathways for realizing reverse control, that is, the unlooping of ssDNAs. The first is to carry out a second irradiation to excite the formed $\mathbf{SPy_2^{\bullet+}}$. The energy levels of $\mathbf{SPy^{\bullet+}}$ and $\mathbf{SPy_2^{\bullet+}}$ make it energetically possible for the excited-state $\mathbf{SPy_2^{\bullet+}}$ ($\mathbf{^1SPy_2^{\bullet+*}}$) to photodissociate to the ground-state $\mathbf{SPy^{\bullet+}}$ and **SPy** (assuming that the energy levels of $\mathbf{SPy^{\bullet+}}$ and $\mathbf{SPy_2^{\bullet+}}$ are similar to those of $Py^{\bullet+}$ and $Py_2^{\bullet+}$, respectively).[68] Samori and Cai *et al*. employed a second irradiation

and directly observed the photodissociation of $Py_2^{\bullet+}$ to the ground-state $Py^{\bullet+}$ and Py,[68] and the photodissociation of $Np_2^{\bullet+}$ (NP, naphthalene) to the ground-state $Np^{\bullet+}$ and Np.[82] The regeneration of $\mathbf{SPy}^{\bullet+}$ and **SPy** would be accompanied by the unlooping of the doubly **SPy**-modified ssDNA. This would be followed by the forward looping driven by the stabilization energy released to form $\mathbf{SPy_2}^{\bullet+}$. However, the photodissociation efficiency of $\mathbf{SPy_2}^{\bullet+}$ to $\mathbf{SPy}^{\bullet+}$ and **SPy** may be low, making the regeneration of $\mathbf{SPy}^{\bullet+}$ incomplete.[68,88] The other possible approach is to reduce the formed $\mathbf{SPy_2}^{\bullet+}$ to $\mathbf{SPy_2}$ through an electron donor. The donation of a single electron can be achieved by using a chemical reductant or photosensitive electron donor. The reduction of $\mathbf{SPy_2}^{\bullet+}$ to $\mathbf{SPy_2}$ would occur in parallel with the dissociation of $\mathbf{SPy_2}$ to **SPy**, giving the original ssDNA modified by **SPy** at both ends. Then, upon a second irradiation with 355 nm light, the next cycle of ssDNA looping regulated by **SPy** under irradiation would be initiated. In the case of azobenzene, the transformation of azobenzenes from *cis* to *trans* by thermal relaxation and/or light irradiation at a specific wavelength allows the resetting of the azobenzene-based photoswitch.[5] When it comes to using **SPy** as a photosensitive regulator, the photodissociation of the formed $\mathbf{SPy_2}^{\bullet+}$ to $\mathbf{SPy}^{\bullet+}$ and **SPy** by exciting $\mathbf{SPy_2}^{\bullet+}$ with a second irradiation, or the reduction of the formed $\mathbf{SPy_2}^{\bullet+}$ by electron donors, enables resetting of the doubly **SPy**-modified ssDNA. Therefore, theoretically, utilization of **SPy** as a photoregulator can achieve on/off dual regulation over the looping and unlooping of ssDNAs (Scheme 1-4). Additionally, electrochemical oxidation and re-reduction of **SPy** may also offer another option for reversibly controlling the conformation and function of biomolecules.

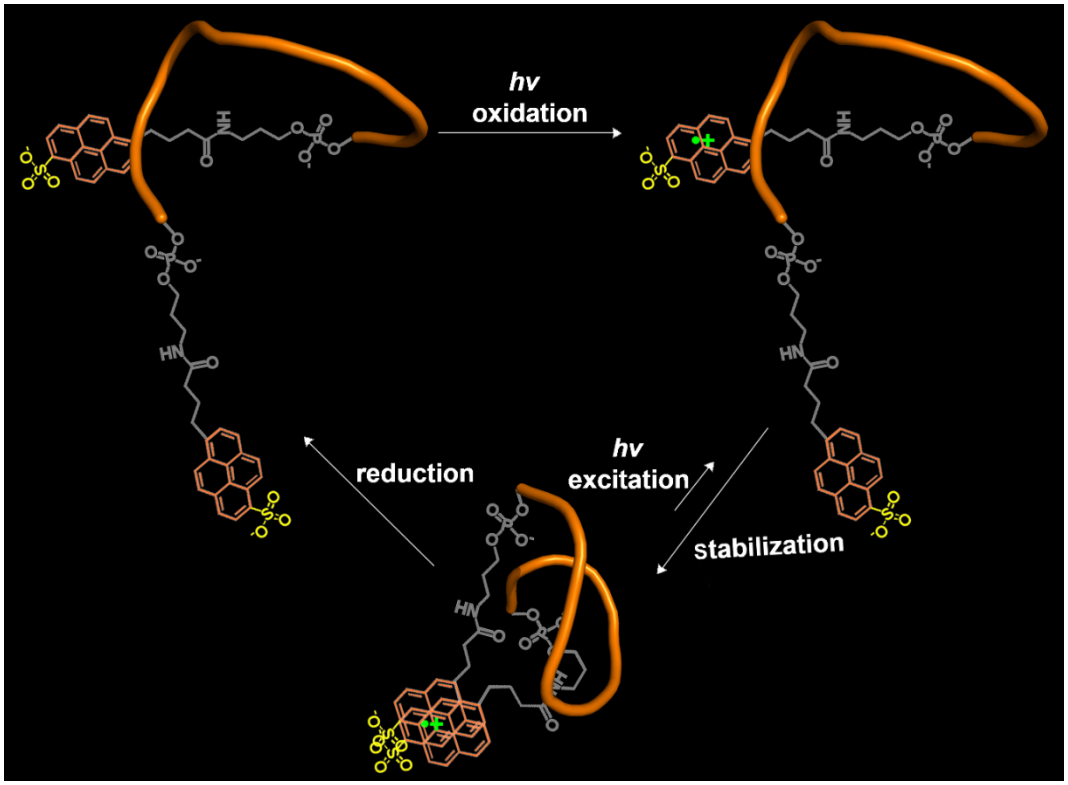

Scheme 1-4. Schematic illustration of the photoregulated looping of ssDNA by **SPy** under photoirradiation and the unlooping through photoirradiation or reduction.

Conclusion

In summary, sulfonated pyrene, **SPy**, was synthesized, characterized, and used as both a probe and photoregulator for the looping of ssDNA. In contrast to the more frequently used hydrophobic Pys, the water solubility of **SPy** would make it ideal for use in aqueous solution to study the conformation, dynamics, flexibility, and assembly of biomolecules, macromolecules, and supramolecules. This offers an effective solution to the barrier caused by the hydrophobicity of Pys. When two **SPys** were attached to the 5'-end and 3'-end positions of ssDNA by a flexible alkyl chain, they functioned as both a probe and a photosensitive regulator for the looping of the modified ssDNA. After photoionization, the generated $\mathbf{SPy}^{\bullet+}$ located at one end of the modified ssDNA molecule associates with the **SPy** located at the other end of the same molecule, because of the stabilization energy released to form $\mathbf{SPy}_2^{\bullet+}$. This stabilization energy provides a driving force for the looping of the modified ssDNA. Conversely, the transiently formed loop

conformation of the modified ssDNA is trapped by the formation of $\mathbf{SPy_2}^{\bullet+}$, which enables the investigation of the loop-formation dynamics of the doubly **SPy**-modified ssDNA regulated by **SPy** and stimulated by photoirradiation. The looping dynamics support our previous conclusion about the formation of misfolded conformations during the end-to-end contact of T-rich ssDNA and the configurational model proposed by Ansari *et al*.[85,87] Moreover, it is demonstrated that, as the length of T-composed ssDNA increases, the significant formation of misfolded intermediates impedes the looping dynamics, and only one slow component being observed for $\mathbf{SPy\text{-}T_{16}\text{-}SPy}$. The photodissociation of the formed $\mathbf{SPy_2}^{\bullet+}$ to $\mathbf{SPy}^{\bullet+}$ and **SPy** by exciting $\mathbf{SPy_2}^{\bullet+}$ with a second irradiation, or the reduction of the formed $\mathbf{SPy_2}^{\bullet+}$ by electron donors, makes it possible to reset the photoregulated system and achieve on/off dual regulation, that is, ssDNA looping and unlooping. More effort is being devoted to consolidate the reversible regulation. For the future use of **SPy** in a specific system with multiple on/off cycles, it is desirable to realize highly controllable and reversible regulation. More comprehensive studies pertinent to the highly regulated on/off cycles when using **SPy** as a photoregulator are ongoing.

Experimental Section

Materials. 1-Pyrenebutyric acid (PyBA), 1-pyrenemethanol, 1-pyrenesulfonic acid sodium salt, chlorosulfonic acid (HSO_3Cl), and other reagents and solvents were purchased from standard suppliers and used without further purification. 5', 3'-bis (3-aminopropyl) bis(phosphate)-modified ssDNAs were purchased from GeneDesign, Inc. and used as received without further purification.

Synthesis of sulfonated pyrene. PyBA and HSO_3Cl were used for the sulfonation. The sulfonation is according to the method reported by Lu and Tanemura *et al*.[89,90] In detail, in an ice-water bath, and with stirring under Ar atmosphere, a solution of HSO_3Cl (0.06 mL, 0.9 mmol) in super dehydrated dichloromethane (DCM) (7.5 mL) was dropwise added to the solution of PyBA in DCM (0.13 g, 0.45 mmol). After the dropwise addition, the mixture was stirred for 2 h. Precipitation was observed during the reaction. Then the saturated sodium hydrogen carbonate ($NaHCO_3$) solution was added to dissolve the precipitate and neutralize the solution. The mixed water phase and organic phase were separated, and the organic phase was washed by water for three times. All water phase solution was collected and evaporated under reduced pressure. Three main products (products 3-5 in Figure 1-1) were detected by HPLC, and they may be constitutional isomers. These three main products were isolated by HPLC and lyophilized.

Table 1-2. HPLC settings for analysis and isolation of sulfonated products

Reverse-phase HPLC settings		
	Analysis	Purification
Column	5C18-MS-II, 1.0 mm I.D. × 15 cm, particle size of 5 μm (nacalai tesque, Japan)	5C18-MS-II, 8.0 mm I.D. × 15 cm, particle size of 5 μm (nacalai tesque, Japan)
Flow rate	1 mL / min	3 mL / min
Detection wavelength	340 nm, 274 nm	
Column temperature	40 ℃	
Mobile phase	acetonitrile	
	50 mM ammonium formate solution	
Gradient elution	acetonitrile from 15% to 24% in 20 min	acetonitrile from 13% to 22% in 30 min

NMR and MS characterization of SPy

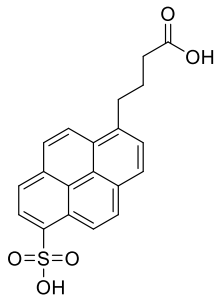

Chemical structure of product 3 (Figure 1-1) was characterized. NMR characterization was carried out on a JEOL-ECA600MHz spectrometer. The sample (**SPy**, product 3 in Figure 1-1) was

dissolved in DMSO-d_6 with TMS as the internal standard. The MS spectrum was obtained on MALDI-TOF spectrometer of Bruker Ultraflex III in negative mode, with 3-hydroxypicolinic acid as the matrix. ^{1}H NMR (600 MHz, DMSO-d_6) δ 9.06 (d, J = 9.5 Hz, 1H), 8.45 (d, J = 8.1 Hz, 1H), 8.37 (d, J = 9.5 Hz, 1H), 8.20 (d, J = 7.9 Hz, 1H), 8.16 (d, J = 8.1 Hz, 1H), 8.15 (d, J = 9.5 Hz, 1H), 8.11 (d, J = 9.5 Hz, 1H), 7.91 (d, J = 7.9 Hz, 1H), 3.27 (br, 2H), 2.35 (t, J = 7.2 Hz, 2H), 2.00-1.95 (m, 2H). ^{13}C NMR (151 MHz, DMSO-d_6) δ 175.00, 142.35, 137.08, 131.56, 129.38, 128.74, 128.15, 127.75, 127.66, 127.32, 126.59, 125.75, 125.34, 125.08, 124.71, 124.24, 123.98, 33.98, 32.71, 27.50. MALDI-TOF-MZ m/z. calcd. for $[M-H]^-$: 367.065, found: 367.017.

Concentration determination of SPy. The precise concentration of **SPy** was determined by NMR using 1-pyrenemethanol as a reference. The purified **SPy** was dissolved in DMSO-d_6. A solution of 1-pyrenemethanol in DMSO-d_6 (accurate concentration) was prepared. The solution of **SPy** and the solution of 1-pyrenemethanol were mixed with a ratio of 1/1. The ^{1}H NMR spectrum was recorded for the mixed samples of **SPy** and 1-pyrenemethanol. By comparing the number of H from the methylene group of 1-pyrenemethanol with the number of H from one methylene group of **SPy**, the concentration of **SPy** can be calculated. Using this **SPy** solution, a standard curve of absorbance *vs.* concentration was plotted and used for the concentration determination of **SPy**-modified ssDNAs.

Pulse radiolysis measurement. The time profiles of the transient absorption of the dimer radical cation of each main product (products 3-5 in Figure 1-1) monitored at 1500 nm and the transient absorption spectra of product 3 in Figure 1-1 (identified as **SPy**) upon oxidation were recorded by pulse radiolysis. During the pulse radiolysis (28 MeV, 8 ns), the probe light was afforded by a xenon flash lamp (XBO-450, Osram, Berlin). The lamp was synchronized with the electron pulse and focused into the sample solution. The absorption spectra in the NIR region were recorded in kinetic mode by recording the time profiles in the specific wavelength. An interference filter (CVI, transmittance of 40%, bandwidth of 10 nm) was used for the recording in the NIR region. The intensity of the probe light in the NIR region was monitored by a fast InGaAs PIN photodiode equipped with an amplifier (Thorlabs, PDA255) and a digital oscilloscope (Tektronix, TDS 580D). The time profiles are the results of single-shot irradiation.

Structure Characterization of SPy. The chemical structure of product 3 (Figure 1-1, identified as **SPy**) was characterized by NMR and MALDI-TOF. NMR characterization was carried out on

a JEOL-ECA600MHz spectrometer. The sample was dissolved in DMSO-d_6 with TMS as the internal standard. The MS spectrum was obtained on MALDI-TOF spectrometer of Bruker Ultraflex III in negative mode, with 3-hydroxypicolinic acid as the matrix.

Synthesis of SPy-NHS. Mixture of **SPy** (1 eq.) solution in milliQ, N-hydroxysuccinimide (NHS) (10 eq.) solution in MilliQ and 1-(3-dimethylaminopropyl)-3-ethylcarbodiimide hydrochloride (EDC•HCl, 10 eq.) solution in MilliQ was stirred in 2-(N-morpholino) ethanesulfonic acid (MES) buffer (50 mM, pH 5) for 2 h at room temperature. The crude product was analyzed and purified by reverse-phase HPLC.

Table 1-3. HPLC settings for analysis and isolation of **SPy**-NHS

<table>
<tr><td colspan="3">Reverse-phase HPLC settings</td></tr>
<tr><td></td><td>Analysis</td><td>Purification</td></tr>
<tr><td>Column</td><td>5C18-AR-II, 1.0 mm I.D. × 15 cm, particle size of 5 μm (nacalai tesque, Japan)</td><td>5C18-AR-II, 10.0 mm I.D. × 15 cm, particle size of 5 μm (nacalai tesque, Japan)</td></tr>
<tr><td>Flow rate</td><td>1 mL / min</td><td>4 mL / min</td></tr>
<tr><td>Detection wavelength</td><td colspan="2">340 nm, 274 nm</td></tr>
<tr><td>Column temperature</td><td colspan="2">40 ℃</td></tr>
<tr><td rowspan="2">Mobile phase</td><td colspan="2">acetonitrile</td></tr>
<tr><td colspan="2">0.1% Trifluoroacetic acid (TFA) solution</td></tr>
<tr><td>Gradient elution</td><td>acetonitrile from 5% to 65% in 20 min</td><td>acetonitrile from 5% to 65% in 30 min</td></tr>
</table>

Synthesis of doubly SPy-ssDNA-SPy. SPy-NHS (15 eq.) was dissolved in MilliQ and added into the solution of ssDNA (1 eq.). The coupling reaction was carried out in phosphate buffer (50 mM, pH 8.0). The reaction was traced by reverse-phase HPLC. When the complete consumption of **SPy**-NHS was observed, the coupling was terminated. The crude product was analyzed and purified by reverse-phase HPLC.

Table 1-4. HPLC settings for analysis and isolation of **SPy-ssDNA-SPy**

<table>
<tr><td colspan="3">Reverse-phase HPLC settings</td></tr>
<tr><td></td><td>Analysis</td><td>Purification</td></tr>
<tr><td>Column</td><td>5C18-AR-II, 1.0 mm I.D. × 15 cm, particle size of 5 μm (nacalai tesque, Japan)</td><td>5C18-AR-II, 10.0 mm I.D. × 15 cm, particle size of 5 μm (nacalai tesque, Japan)</td></tr>
<tr><td>Flow rate</td><td>1 mL / min</td><td>4 mL / min</td></tr>
<tr><td>Detection wavelength</td><td colspan="2">340 nm, 260 nm</td></tr>
<tr><td>Column temperature</td><td colspan="2">40 ℃</td></tr>
<tr><td rowspan="2">Mobile phase</td><td colspan="2">acetonitrile</td></tr>
<tr><td colspan="2">50 mM ammonium formate solution</td></tr>
<tr><td>Gradient elution</td><td>acetonitrile from 5% to 65%
in 20 min</td><td>acetonitrile from 5% to 25%
in 40 min</td></tr>
</table>

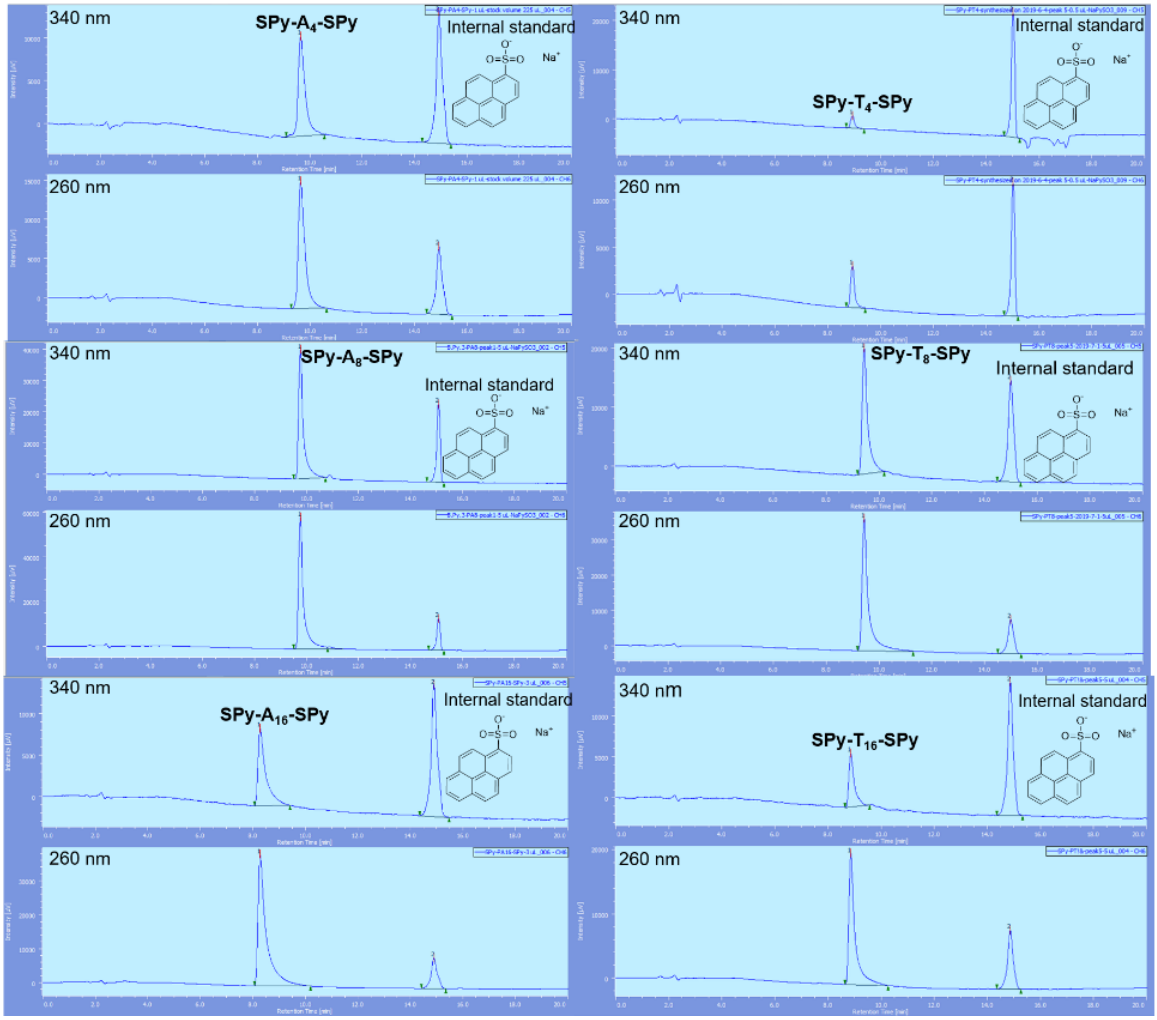

Figure 1-10. HPLC chromatograms of **SPy-ssDNA-SPy**. Left: **SPy-A$_n$-SPy**; right: **SPy-T$_n$-SPy**, n = 4, 8, and 16. The HPLC settings are shown in Table 1-4.

Identification of SPy-ssDNA-SPy. The synthesized **SPy-ssDNA-SPy** was identified by MALDI-TOF mass spectrometry (Ultraflex III, Bruker) in negative mode, with 3-hydroxypicolinic acid as the matrix.

Table 1-5. MALDI-TOF-MS results of **SPy-ssDNA-SPy**

SPy-ssDNA-SPy	Calculated (Exact mass)	Found (m/z)
SPy-AAAA-SPy	2163.440	2166.440
SPy-AAAAAAAA-SPy	3414.665	3420.339
SPy-AAAAAAAAAAAAAAA-SPy	5919.131	5925.011
SPy-TTTT-SPy	2126.386	2132.695
SPy-TTTTTTTT-SPy	3342.573	3348.289
SPy-TTTTTTTTTTTTTTTT-SPy	5774.945	5781.163

Laser flash photolysis measurement. The measurement was carried out in sodium phosphate buffer (10 mM, pD 7.0) at room temperature. The concentration of **SPy** for transient absorption spectrum measurement and time profile recording was 40 μM. The concentration of **SPy-ssDNA-SPy** sample was 40 μM. The excitation of **SPy** was achieved by the third-harmonic oscillation (355 nm, full width at half-maximum of 4 ns, 20 mJ per pulse) from Q-switched Nd: YAG laser (Surelight, Continuum, Santa Clara, CA). A xenon flash lamp (XBO-450, Osram, Berlin) was focused into the sample solution as the probe light. The recording in the UV-visible region was measured with a monochromator (G250, Nikon) equipped with a photomultiplier (R928, Hamamatsu Photonics, Hamamatsu City, Japan) and digital oscilloscope (TDS-580D, Tektronix). The measurement in the NIR region was obtained with a monochromator (SG-100, Koken) and the probe light intensity was monitored by a fast InGaAs PIN photodiode equipped with an amplifier (Thorlabs, PDA255) and digital oscilloscope. All the time profiles of **SPy** and **SPy-ssDNA-SPy** are the results of single-shot irradiation.

UV-vis absorption and fluorescence spectrometry measurement. The UV-vis absorption and fluorescence spectra were measured on SHIMADZU UV-3600 plus UV-VIS-NIR spectrophotometer and Horiba Fluoromax-4 spectrofluorometer, respectively. **SPy** and **SPy-ssDNA-SPy** were measured in PBS buffer (10 mM, pH 7.0) at room temperature. PyBA was measured in KCl/NaOH buffer (pH 13.0).

References

[1] W. Szymański, J. M. Beierle, H. A. V. Kistemaker, W. A. Velema, B. L. Feringa, *Chem. Rev.* **2013**, *113*, 6114–6178.

[2] H. Asanuma, X. Liang, H. Nishioka, D. Matsunaga, M. Liu, M. Komiyama, *Nat. Protoc.* **2007**, *2*, 203-212.

[3] X. Tang, I. J. Dmochowski, *Mol. Biosyst.* **2007**, *3*, 100–110.

[4] A. S. Lubbe, W. Szymanski, B. L. Feringa, *Chem. Soc. Rev.* **2017**, *46*, 1052–1079.

[5] A. A. Beharry, G. A. Woolley, *Chem. Soc. Rev.* **2011**, *40*, 4422–4437.

[6] G. Mayer, A. Heckel, *Angew. Chem. Int. Ed.* **2006**, *45*, 4900–4921.

[7] Z. L. Pianowski, *Chem. Eur. J.* **2019**, *25*, 5128–5144.

[8] N. Ankenbruck, T. Courtney, Y. Naro, A. Deiters, *Angew. Chem. Int. Ed.* **2018**, *57*, 2768–2798.

[9] I. Tochitsky, M. A. Kienzler, E. Isacoff, R. H. Kramer, *Chem. Rev.* **2018**, *118*, 10748–10773.

[10] K. Yamana, A. Yoshikawa, H. Nakano, *Tetrahedron Lett.* **1996**, *37*, 637–640.

[11] Y. Kamiya, T. Takagi, H. Ooi, H. Ito, X. Liang, H. Asanuma, *ACS Synth. Biol.* **2015**, *4*, 365–370.

[12] H. Asanuma, T. Ito, T. Yoshida, X. Liang, M. Komiyama, *Angew. Chem. Int. Ed.* **1999**, *38*, 2393–2395.

[13] H. Ito, X. Liang, H. Nishioka, H. Asanuma, *Org. Biomol. Chem.* **2010**, *8*, 5519–5524.

[14] H. Asanuma, T. Takarada, T. Yoshida, D. Tamaru, X. Liang, M. Komiyama, *Angew. Chem. Int. Ed.* **2001**, *40*, 2671–2673.

[15] H. Nishioka, X. Liang, H. Asanuma, *Chem. Eur. J.* **2010**, *16*, 2054–2062.

[16] H. Asanuma, T. Ishikawa, Y. Yamano, K. Murayama, X. Liang, *ChemPhotoChem* **2019**, *3*, 418–424.

[17] B. Cheng, H. Kashida, N. Shimada, A. Maruyama, H. Asanuma, *ChemBioChem* **2017**, *18*,

1568–1572.

[18] J. Bredenbeck, J. Helbing, A. Sieg, T. Schrader, W. Zinth, C. Renner, R. Behrendt, L. Moroder, J. Wachtveitl, P. Hamm, *Proc. Natl. Acad. Sci. USA* **2003**, *100*, 6452–6457.

[19] J. Bredenbeck, J. Helbing, J. R. Kumita, G. A. Woolley, P. Hamm, *Proc. Natl. Acad. Sci. USA.* **2005**, *102*, 2379–2384.

[20] C. Renner, L. Moroder, *ChemBioChem* **2006**, *7*, 868–878.

[21] B. Buchli, S. A. Waldauer, R. Walser, M. L. Donten, R. Pfister, N. Blöchliger, S. Steiner, A. Caflisch, O. Zerbe, P. Hamm, *Proc. Natl. Acad. Sci. USA* **2013**, *110*, 11725–11730.

[22] J. A. Ihalainen, B. Paoli, S. Muff, E. H. G. Backus, J. Bredenbeck, G. A. Woolley, A. Caflisch, P. Hamm, *Proc. Natl. Acad. Sci. USA* **2008**, *105*, 9588–9593.

[23] B. Jankovic, A. Gulzar, C. Zanobini, O. Bozovic, S. Wolf, G. Stock, P. Hamm, *J. Am. Chem. Soc.* **2019**, *141*, 10702–10710.

[24] A. Mourot, C. Herold, M. A. Kienzler, R. H. Kramer, *Br. J. Pharmacol.* **2018**, *175*, 2296–2311.

[25] W.-C. Lin, R. H. Kramer, *Bioconjug. Chem.* **2018**, *29*, 861–869.

[26] I. Tochitsky, Z. Helft, V. Meseguer, R. B. Fletcher, K. A. Vessey, M. Telias, B. Denlinger, J. Malis, E. L. Fletcher, R. H. Kramer, *Neuron* **2016**, *92*, 100–113.

[27] J. Garcia-Amorós, M. Díaz-Lobo, S. Nonell, D. Velasco, *Angew. Chem. Int. Ed.* **2012**, *51*, 12820–12823.

[28] A. S. Lubbe, Q. Liu, S. J. Smith, J. W. de Vries, J. C. M. Kistemaker, A. H. de Vries, I. Faustino, Z. Meng, W. Szymanski, A. Herrmann, B. L. Feringa, *J. Am. Chem. Soc.* **2018**, *140*, 5069–5076.

[29] S. Crespi, N. A. Simeth, B. König, *Nat. Rev. Chem.* **2019**, *3*, 133–146.

[30] M. Škugor, J. Valero, K. Murayama, M. Centola, H. Asanuma, M. Famulok, *Angew. Chem.* **2019**, *131*, 7022–7025.

[31] J. Valero, M. Centola, Y. Ma, M. Škugor, Z. Yu, M. W. Haydell, D. Keppner, M. Famulok,

Nat. Protoc. **2019**, *14*, 2818–2855.

[32] Y. Kamiya, H. Asanuma, *Acc. Chem. Res.* **2014**, *47*, 1663–1672.

[33] J. Chen, F. K.-C. Leung, M. C. A. Stuart, T. Kajitani, T. Fukushima, E. van der Giessen, B. L. Feringa, *Nat. Chem.* **2017**, *10*, 132.

[34] C. Poloni, M. C. A. Stuart, P. van der Meulen, W. Szymanski, B. L. Feringa, *Chem. Sci.* **2015**, *6*, 7311–7318.

[35] A. S. Lubbe, C. Böhmer, F. Tosi, W. Szymanski, B. L. Feringa, *J. Org. Chem.* **2018**, *83*, 11008–11018.

[36] K. Murayama, Y. Yamano, H. Asanuma, *J. Am. Chem. Soc.* **2019**, *141*, 9485–9489.

[37] T. M. Figueira-Duarte, K. Müllen, *Chem. Rev.* **2011**, *111*, 7260–7314.

[38] J. Wisniak, *Educ. Química* **2009**, *20*, 166–175.

[39] G. Bains, A. B. Patel, V. Narayanaswami, *Molecules.* **2011**, *16*, 7909-7935.

[40] P. Conlon, C. J. Yang, Y. Wu, Y. Chen, K. Martinez, Y. Kim, N. Stevens, A. A. Marti, S. Jockusch, N. J. Turro, W. Tan, *J. Am. Chem. Soc.* **2008**, *130*, 336–342.

[41] A. Okamoto, T. Ichiba, I. Saito, *J. Am. Chem. Soc.* **2004**, *126*, 8364–8365.

[42] J. Duhamel, *Langmuir* **2012**, *28*, 6527–6538.

[43] J. Merz, J. Fink, A. Friedrich, I. Krummenacher, H. H. Al Mamari, S. Lorenzen, M. Haehnel, A. Eichhorn, M. Moos, M. Holzapfel, H. Braunschweig. C. Lambert, A. Steffen, L. Ji, T. B. Marder, *Chem. Eur. J.* **2017**, *23*, 13164–13180.

[44] K. Kawai, K. Miyamoto, S. Tojo, T. Majima, *J. Am. Chem. Soc.* **2003**, *125*, 912–915.

[45] H. Tang, C. S. de Oliveira, G. Sonntag, C. L. D. Gibb, B. C. Gibb, C. Bohne, *J. Am. Chem. Soc.* **2012**, *134*, 5544–5547.

[46] M. Vybornyi, A. V Rudnev, S. M. Langenegger, T. Wandlowski, G. Calzaferri, R. Häner, *Angew. Chem. Int. Ed.* **2013**, *52*, 11488–11493.

[47] K. Kawai, H. Yoshida, T. Takada, S. Tojo, T. Majima, *J. Phys. Chem. B* **2004**, *108*, 13547–

13550.

[48] K. Kawai, H. Yoshida, A. Sugimoto, M. Fujitsuka, T. Majima, *J. Am. Chem. Soc.* **2005**, *127*, 13232–13237.

[49] D. Sahoo, V. Narayanaswami, C. M. Kay, R. O. Ryan, *Biochemistry* **2000**, *39*, 6594–6601.

[50] A. B. Patel, P. Khumsupan, V. Narayanaswami, *Biochemistry* **2010**, *49*, 1766–1775.

[51] C. Mizuguchi, M. Hata, P. Dhanasekaran, M. Nickel, M. C. Phillips, S. Lund-Katz, H. Saito, *Biochemistry* **2012**, *51*, 5580–5588.

[52] T. Hall, G. Whitton, R. Casier, M. Gauthier, J. Duhamel, *Macromolecules* **2018**, *51*, 7914–7923.

[53] S. Karuppannan, J.-C. Chambron, *Chem. Asian J.* **2011**, *6*, 964–984.

[54] H. Kashida, A. Kurihara, H. Kawai, H. Asanuma, *Nucleic Acids Res.* **2017**, *45*, e105.

[55] H. Kashida, T. Takatsu, K. Sekiguchi, H. Asanuma, *Chem. Eur. J.* **2010**, *16*, 2479–2486.

[56] R. Zhou, C. Xu, J. Dong, G. Wang, *Biosens. Bioelectron.* **2015**, *65*, 103–107.

[57] M. S. Shchepinov, V. A. Korshun, *Nucleosides, Nucleotides and Nucleic Acids* **2001**, *20*, 369–374.

[58] R. Casier, J. Duhamel, *Macromolecules* **2018**, *51*, 3450–3457.

[59] G. K. Bains, S. H. Kim, E. J. Sorin, V. Narayanaswami, *Biochemistry* **2012**, *51*, 6207–6219.

[60] J. B. Birks, D. J. Dyson, I. H. Munro, B. H. Flowers, *Proc. R. Soc. London. Ser. A. Math. Phys. Sci.* **1963**, *275*, 575–588.

[61] P. C. Johnson, H. W. Offen, *J. Chem. Phys.* **1973**, *59*, 801–806.

[62] D. A. Van Dyke, B. A. Pryor, P. G. Smith, M. R. Topp, *J. Chem. Educ.* **1998**, *75*, 615.

[63] M. Hara, S. Tojo, K. Kawai, T. Majima, *Phys. Chem. Chem. Phys.* **2004**, *6*, 3215–3220.

[64] N. Getoff, S. Solar, U.-B. Richter, M. W. Haenel, *Radiat. Phys. Chem.* **2003**, *66*, 207–214.

[65] M. A. J. Rodgers, *Chem. Phys. Lett.* **1971**, *9*, 107–108.

[66] W. M. Nau, X. Wang, *ChemPhysChem* **2002**, *3*, 393–398.

[67] A. Kira, S. Arai, M. Imamura, *J. Phys. Chem.* **1972**, *76*, 1119–1124.

[68] S. Samori, M. Fujitsuka, T. Majima, *Res. Chem. Intermed.* **2013**, *39*, 449–461.

[69] Y. Mori, H. Shinoda, T. Nakano, T. Kitagawa, *J. Phys. Chem. A* **2002**, *106*, 11743–11749.

[70] I. Benkyi, E. Tapavicza, H. Fliegl, D. Sundholm, *Phys. Chem. Chem. Phys.* **2019**, *21*, 21094–21103.

[71] C. M. Jones, S. A. Asher, *J. Chem. Phys.* **1988**, *89*, 2649–2661.

[72] X. Wang, W. M. Nau, *J. Am. Chem. Soc.* **2004**, *126*, 808–813.

[73] J. S. Mann, Y. Shibata, T. Meehan, *Bioconjug. Chem.* **1992**, *3*, 554–558.

[74] N. L. Goddard, G. Bonnet, O. Krichevsky, A. Libchaber, *Phys. Rev. Lett.* **2000**, *85*, 2400–2403.

[75] D. Chakraborty, N. Hori, D. Thirumalai, *J. Chem. Theory Comput.* **2018**, *14*, 3763–3779.

[76] W. M. Nau, F. Huang, X. Wang, H. Bakirci, G. Gramlich, *Chim. Int. J. Chem.* **2003**, *57*, 161–167.

[77] T. Devic, M. Yuan, J. Adams, D. C. Fredrickson, S. Lee, D. Venkataraman, *J. Am. Chem. Soc.* **2005**, *127*, 14616–14627.

[78] J. K. Kochi, R. Rathore, P. Le Maguères, *J. Org. Chem.* **2000**, *65*, 6826–6836.

[79] M. Jørgensen, T. Bjørnholm, K. Bechgaard, *Synth. Met.* **1990**, *38*, 77–86.

[80] J. Hoche, H.-C. Schmitt, A. Humeniuk, I. Fischer, R. Mitrić, M. I. S. Röhr, *Phys. Chem. Chem. Phys.* **2017**, *19*, 25002–25015.

[81] M. A. J. Rodgers, *J. Chem. Soc. Faraday Trans. 1 Phys. Chem. Condens. Phases* **1972**, *68*, 1278–1286.

[82] A. Kira, S. Arai, M. Imamura, *J. Chem. Phys.* **1971**, *54*, 4890–4895.

[83] A. R. Dias, M. E. Minas Da Piedade, J. A. Martinho Simões, J. A. Simoni, C. Teixeira, H. P. Diogo, Y. Meng-Yan, G. Pilcher, *J. Chem. Thermodyn.* **1992**, *24*, 439–447.

[84] F. Zhang, A. Zarrine-Afsar, M. S. Al-Abdul-Wahid, R. S. Prosser, A. R. Davidson, G. A. Woolley, *J. Am. Chem. Soc.* **2009**, *131*, 2283–2289.

[85] A. Ansari, S. V Kuznetsov, Y. Shen, *Proc. Natl. Acad. Sci. USA* **2001**, *98*, 7771–7776.

[86] A. Ansari, S. V Kuznetsov, *J. Phys. Chem. B* **2005**, *109*, 12982–12989.

[87] S. V. Kuznetsov, A. Ansari, *Biophys. J.* **2012**, *102*, 101–111.

[88] X. Cai, S. Tojo, M. Fujitsuka, T. Majima, *J. Phys. Chem. A* **2006**, *110*, 9319–9324.

[89] W. Lu, D. Yuan, J. Sculley, D. Zhao, R. Krishna, H.-C. Zhou, *J. Am. Chem. Soc.* **2011**, *133*, 18126–18129.

[90] K. Tanemura, T. Suzuki, T. Horaguchi, *J. Appl. Polym. Sci.* **2013**, *127*, 4524–4536.

Appendix: NMR spectra of SPy

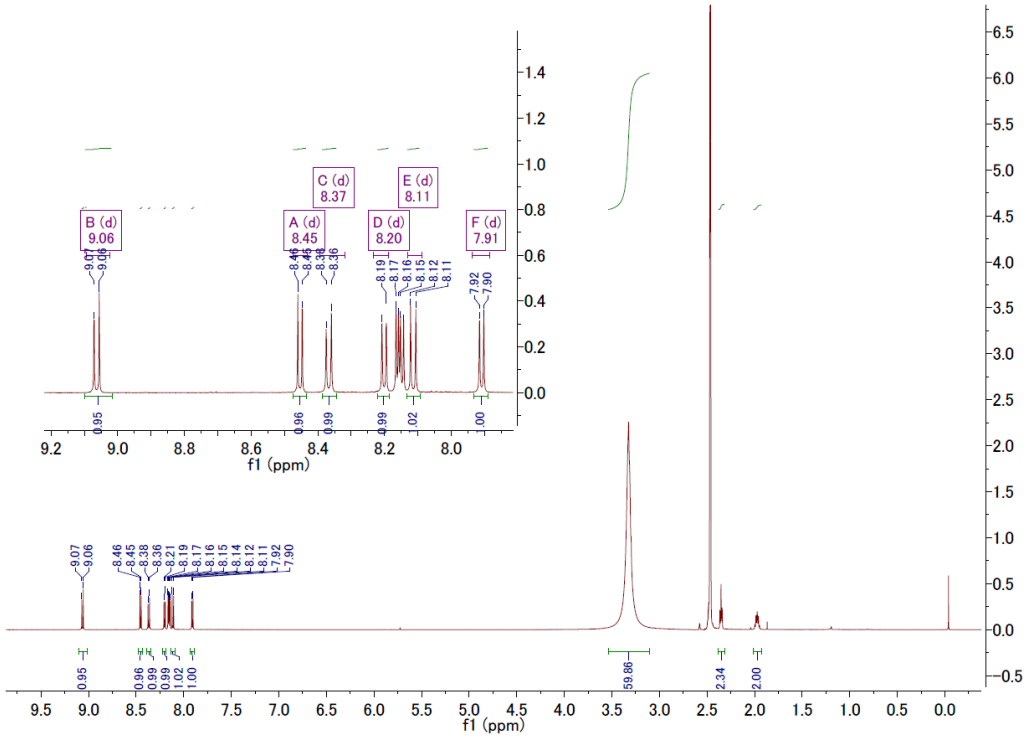

Figure 1-11. 600 MHz ^{1}H NMR spectrum of **SPy** in DMSO-d_6.

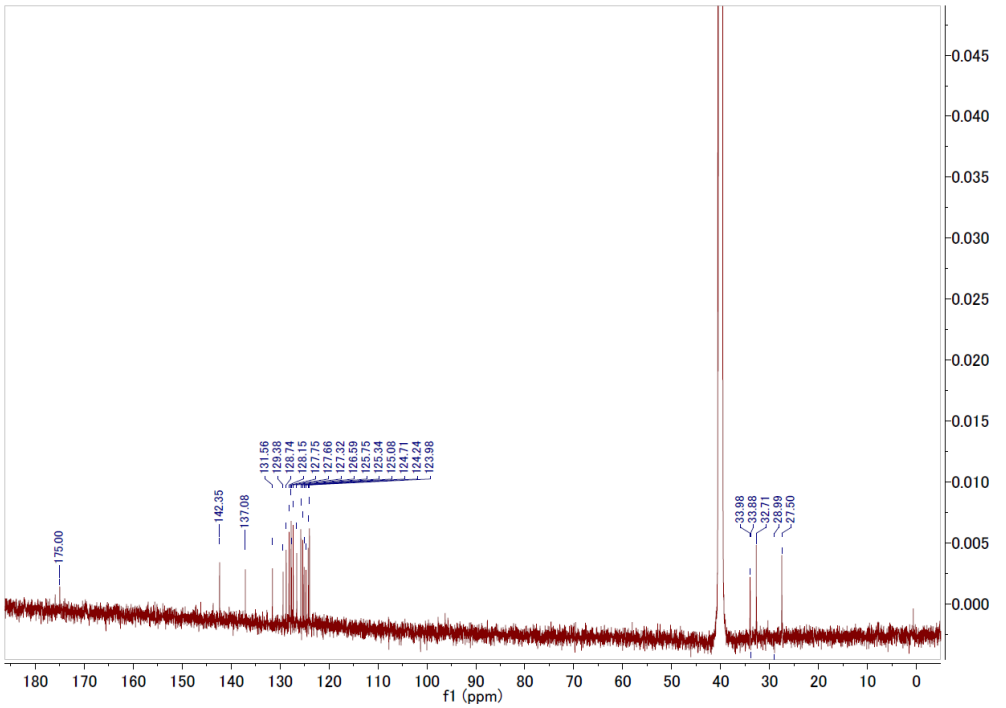

Figure 1-12. 151 MHz ^{13}C NMR spectrum of **SPy** in DMSO-d_6.

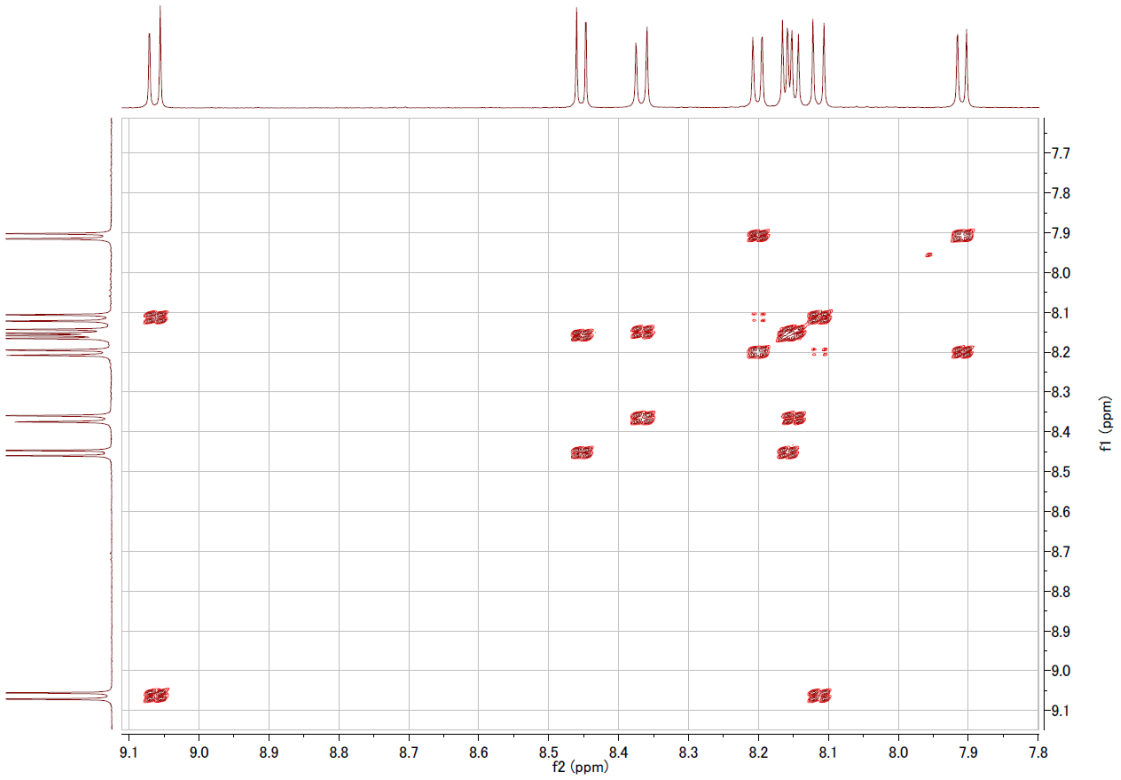

Figure 1-13. COSY spectrum of **SPy** in DMSO-d_6.

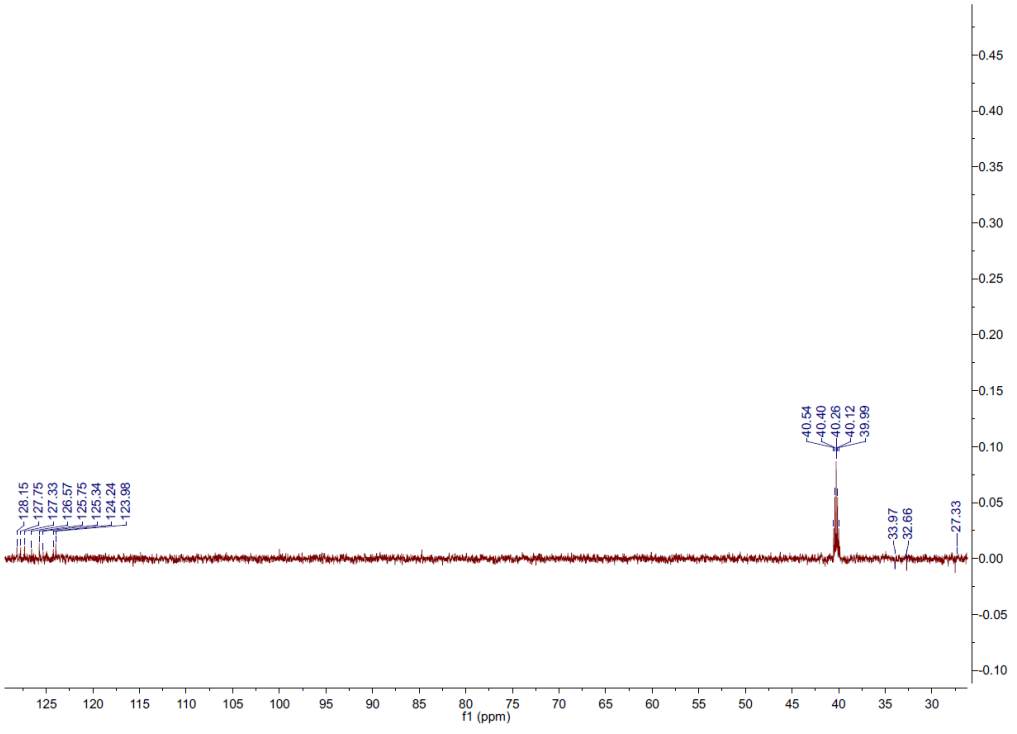

Figure 1-14. DEPT spectrum of **SPy** in DMSO-d_6.

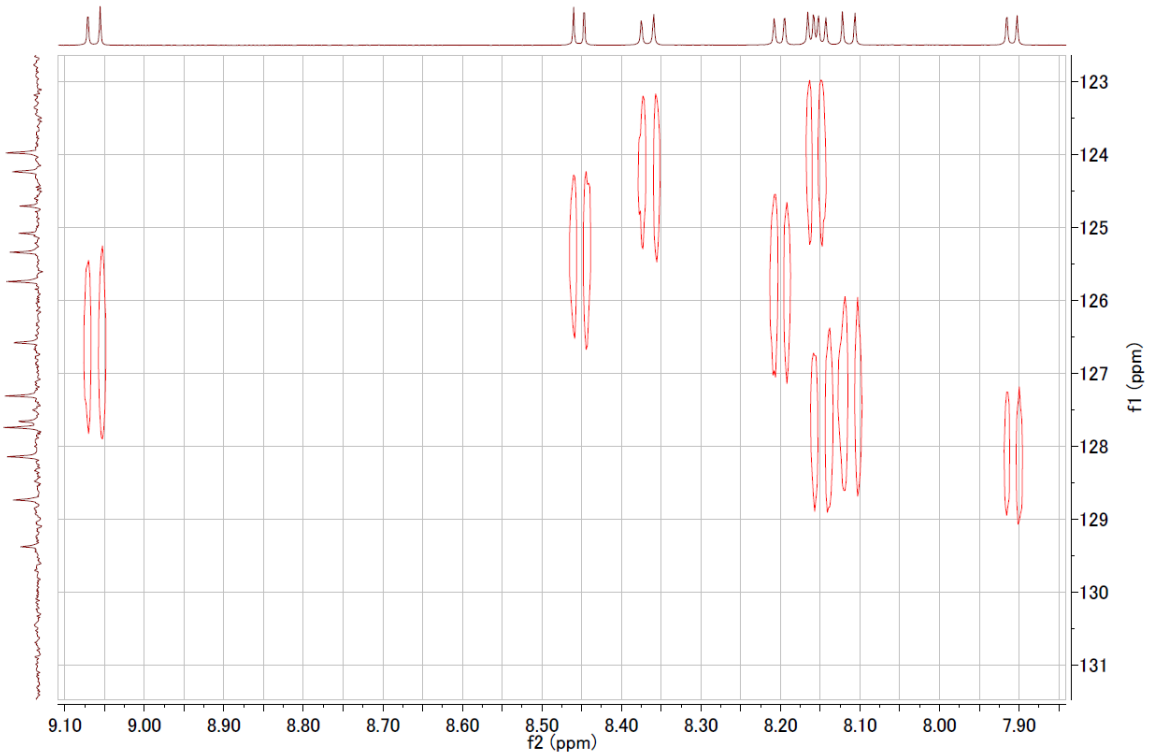

Figure 1-15. HMQC spectrum of **SPy** in DMSO-d_6.

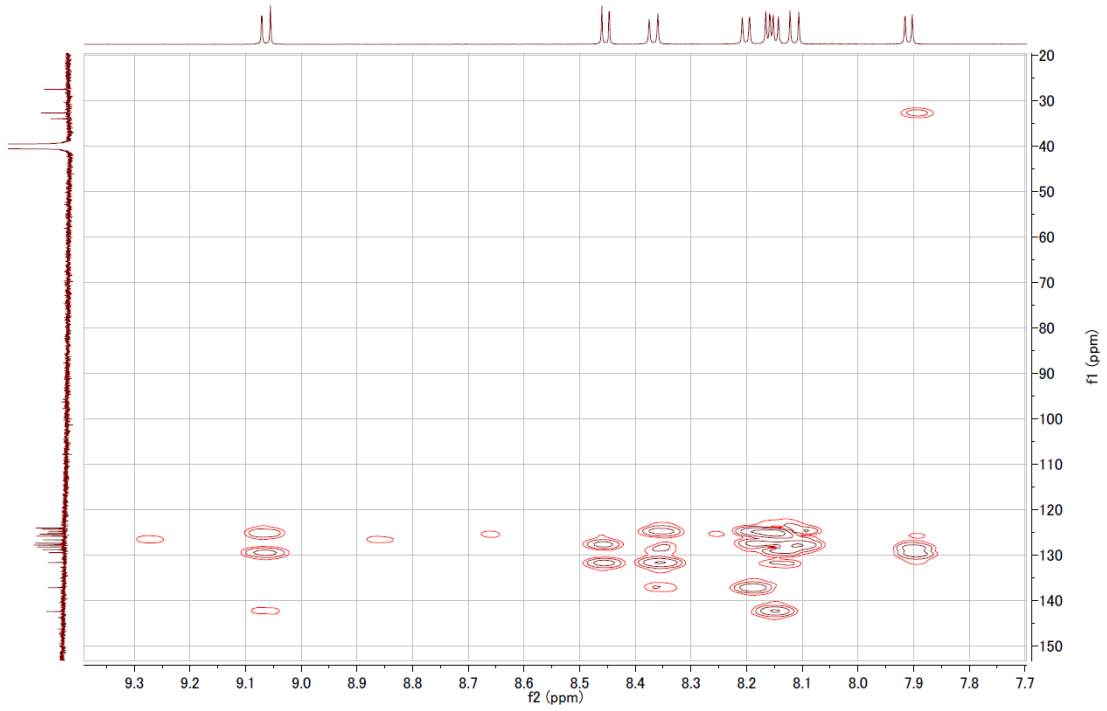

Figure 1-16. HMBC spectrum of **SPy** in DMSO-d_6.

Chapter 2 Dynamics of Single-Stranded RNA Looping Probed and Photoregulated by Sulfonated Pyrene

Abstract

RNAs especially the noncoding RNAs which lack protein-coding capacity but have critical functions in a wide range of cellular processes have received increased attention. They are reported to be associated with the normal development and physiology, and their disruption would cause cancer. RNAs are dynamic molecules and the structural transition of them is fundamental to many RNA-involved cellular processes. The study of transition dynamics is critical to gaining knowledge on how the transition occurs, what factors govern the transition, and how to externally regulate the transition. Previously, we have reported the synthesis of sulfonated pyrene, **SPy**, and its application as a photoregulator for single-stranded DNA (ssDNA) looping. Herein, we studied the dynamics of single-stranded RNA (ssRNA) looping in aqueous solution by using **SPy** as both a probe and photoregulator. The rate of end-to-end loop formation in ssRNA regulated by **SPy** upon photostimulation suggests a retarding impact of the ribose 2'-OH. The results also attest that $(rU)_n$ sequences are endowed with higher flexibility compared with $(dT)_n$ sequences and demonstrate the slowing down effect of C5-CH_3 group in thymine base on the looping dynamics of polythymine sequences. The photoregulated ssRNA looping observed herein occurs at μs to tens of μs timescales. All the findings provide important insight into the flexibility and structural transition dynamics of oligonucleotides.

Introduction

Both DNA and RNA are biomolecules carrying the genetic information necessary to create life and specify the function of any particular organism. Both of them are composed of alternating phosphate, sugar, and nucleobase. It is these distinctive chemical components they shared that allow them to store hereditary molecular information. In spite of the fact that they have very similar chemical components, their structures and biological roles are demonstrated to be different in many aspects. The study on the structure of RNA was initially alongside DNA and the biological role of RNA was regarded to be subordinated to that of DNA called the blueprint of life. Since the discovery of the catalysis role of RNA in the 1980s, the field of RNA chemistry has undergone an

astounding explosion. Nowadays, it is found that the initially underestimated molecules feature much greater structural and functional versatility compared with DNA.[1,2] By virtue of both canonical and noncanonical base pairing, single-stranded RNA (ssRNA) folds into a variety of secondary structural motifs, the common elements of which include hairpin loops and internal loops, stems, bulges, junctions.[1,3,4] The formed secondary structural motifs of RNA then further interact between distinct elements and assemble into complex hierarchical tertiary structures with highly conserved motifs such as pseudoknot, A-minor motif, tetraloops, ribose zippers, and kink-turns.[1,3,4] The folding is guided by hydrogen bonding, base stacking, and van der Waals contact. These are interactions among distant nucleotides and interactions involving ribose 2'-OH groups and phosphate groups. The folding is stabilized by binding of basic proteins, or small molecules, or monovalent and/or divalent metal ions. In this manner, RNA can fold into a remarkable variety of structures. It is this feature and the ability of RNA to pair with DNA that grants RNA versatile biological functions.[5] Apart from the role as genetic carriers for the genetic information transfer from DNA to proteins (the roles of messenger RNA and transfer RNA), RNA has versatile important roles in a wide range of cellular processes, including (1) working as primers in DNA replication, (2) acting as the building block for ribosomes and contributing to the central functions of ribosome such as decoding mRNA, catalyzing the formation of peptide bonds and the hydrolysis of peptidyl-tRNA bonds (the role of ribosome RNA),[6,7] (3) catalyzing the reaction along the pathway of gene expressions such as RNA self-replication, splicing, and degradation (the role of ribozyme),[1,8] (4) binding small molecules to control gene expression (the role of riboswitch),[9] (5) targeting mRNA to control the translation of messenger RNA (the role of microRNA), (6) repressing transposon and making DNA methylated (the role of PIWI-interacting RNA),[10] (7) DNA damage response and repair,[11–17] just to name a few. More functions with relevance to non-coding RNA are being explored.[10,18,19]

As mentioned above, it is the ability of RNA to fold into intricate secondary and tertiary structures that affords them versatile critical functions for maintaining the fundamental processes of life. From another perspective, RNA is a dynamic molecule and any changes to the preexisting structures adopted by RNA would lead to functional change.[20] From this point of view, the function realization of many RNAs in the sophisticated biological processes is through their structural transition upon being triggered by other effectors and/or the surrounding environment change.[20,21] In other words, the structural transition of RNAs is the basis of many RNA-involved

physiological activities. Gaining insight into the structural transition dynamics of RNAs is undoubtedly the key to understanding the factors controlling the transition and the possible mechanism and pathway of transition.[22–30] Furthermore, this can provide valuable information on how to externally control the transition of RNAs for achieving RNA function control.[31]

Pyrene and its derivatives (hereinafter Py) are acknowledged gold probes of microenvironmental change.[32] They are widely used for studying the structure and structural dynamics of macromolecules and supramolecular assemblies with varied sizes, compositions, and architectures at < 1 μs timescales.[33–42] Formation and decay of singlet-excited state of pyrene, $^1Py^*$, and excimer, $^1Py_2^*$, are involved in these studies, the lifetimes of which are hundreds of ns and tens of ns, respectively.[43–47] They would not be suitable when the molecular dynamics have a comparable rate to the decay rates of $^1Py^*$ and $^1Py_2^*$.[48] In stark contrast to the approaches based on $^1Py^*$ and $^1Py_2^*$, the method utilizing the formation of pyrene dimer radical cation, $Py_2^{\bullet+}$, enables tracing the molecular dynamics over a wider time window from 10 ns to 1 ms.[47,49–51] $Py^{\bullet+}$ is first formed after one-electron oxidation by photostimulation. It associates with its neutral counterpart, Py, and gives rise to $Py_2^{\bullet+}$. Due to the much longer lifetimes of $Py^{\bullet+}$ and $Py_2^{\bullet+}$ in comparison with $^1Py^*$, $^1Py_2^*$ and other common fluorescence probes, which is in the time range of 0.1–100 μs,[45,52,53] molecular events taking place at long timescales can be traced by observing $Py_2^{\bullet+}$ formation. Using this method, we have previously studied the end fraying of duplex double-stranded DNA (dsDNA),[50] the kinetics of internal sites in duplex dsDNAs[51] and the end-to-end contact dynamics of single-stranded DNA (ssDNA).[49] In our very recent work, by introducing sulfonated pyrene (**SPy,** Figure 2-1), a water-soluble pyrene derivative, into ssDNA, the looping kinetics of ssDNA was traced. It was demonstrated that the two end-linked **SPys** play as both probes and photoregulators for ssDNA looping upon photostimulation.[47] Given the structural and functional versatility of RNA, bearing in mind that it is through structure transition that many functions of RNA are realized,[10,18] and considering the fact that loop is an inextricable element in both the secondary and tertiary motifs of RNAs, it is believed that the study on the dynamics of loop formation in RNA would provide valuable insight on loop-involved RNA structural transition. Moreover, it is found that RNA looping can trigger translation.[54] Therefore, we herein studied the dynamics of photoregulated ssRNA looping by introducing **SPy** at both the 5'-end and 3'-end positions of ssRNA. The looping kinetics was traced by observing the formation rate of the dimer

radical cation of **SPy** (k**SPy**$_2^{\bullet+}$). A comparison of the observed dynamics with the previously reported ssDNA results was fully discussed.

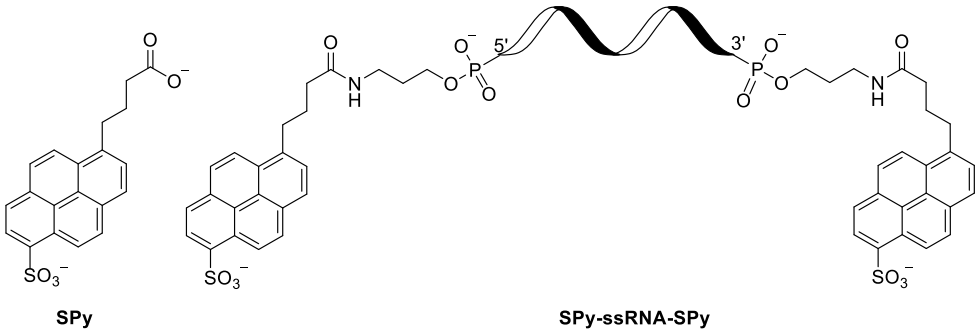

Figure 2-1. Chemical structures of **SPy** and **SPy-ssRNA-SPy**.

Results and Discussion

Chemical structures of **SPy** and doubly **SPy**-modified ssRNA are shown in Figure 2-1. The absorption spectrum of **SPy** measured in phosphate buffer was shown in Figure 2-2. Compared with hydrophobic Py, the absorption bands of **SPy** displayed a redshift,[47] and the photon harvesting ability is reduced, with a molar absorption coefficient of 2928 m^2 mol^{-1} at 354 nm (the molar absorption coefficient of pyrene in cyclohexane at 335 nm is 5400 m^2 mol^{-1}).[55]

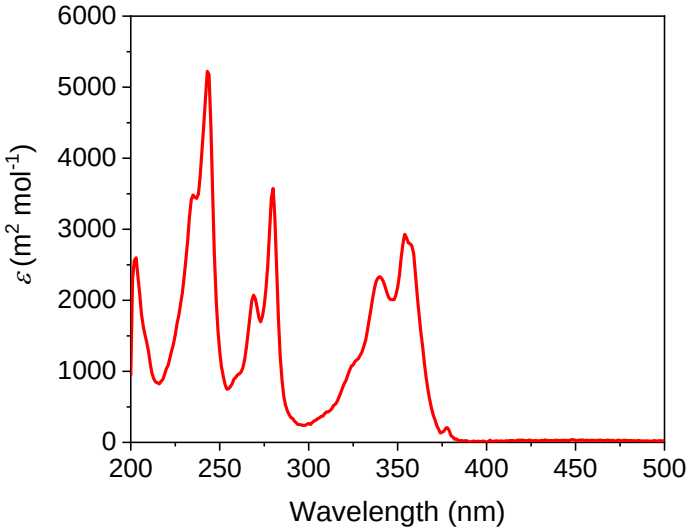

Figure 2-2. UV-vis absorption spectrum of **SPy**. The absorption spectra of a dilution series of SPy in phosphate buffer (pH 7.0) were measured for the determination of the molar absorption coefficient at each wavelength.

The structure of the doubly **SPy**-modified ssRNA before photostimulation was first studied. The structure of a given RNA molecule in solution is an ensemble of many interconverting structural forms.[21] After two **SPys** were introduced into ssRNA, the interplay between the structural diversity of ssRNA and the interaction of end-linked **SPys** with nucleobases in ssRNA probably makes the two end-linked **SPys** having a cofacial contact before photostimulation. For one doubly **SPy**-modified ssRNA molecule, this structural form with the two end-linked **SPys** forming a non-oxidized cofacial **SPy** dimer constitutes a part of the ensemble structures. The population of this sort of structural form depends on the kind of nucleobase in ssRNA and the length. To gain insight into the difference of this population among doubly **SPy**-modified ssRNAs, the steady-state absorption and fluorescence spectra were examined. As shown in Figures 2-3A and B, for each sequence of doubly **SPy**-modified ssRNA, the absorption spectrum in its entirety is the assembled characteristic absorption bands from RNA bases and **SPys**. A redshift (6 nm) was observed for the absorption bands featured by **SPys** in **SPy-ssRNA-SPy** compared with the intact **SPy** monomer. This is the indication of the π-stacking interaction between the end-linked **SPy** and the constituent bases of ssRNA. As the length of ssRNA increases, the absorption contribution from the nucleobases in $(rA)_n$ and $(rU)_n$ increases. Particular attention should be paid to the absorbance ratio of the absorption band at 345 nm (14Ag transition of $S_0 \rightarrow S_2$) to the absorption band at 360 nm (0–0 transition of $S_0 \rightarrow S_2$).[56,57] The ratio varies by the constituent bases and length of ssRNA. From this ratio, the population of such structural forms of **SPy-ssRNA-SPy** that the two end-linked **SPys** form a non-oxidized cofacial **SPy** dimer can be deciphered.[47,49–51] For **SPy-$(rA)_n$-SPy**, the ratio is less than unity and shows a visible decrease as the increase of n from 4 to 8 and 16. In the case of **SPy-$(rU)_4$-SPy**, the ratio exceeds unity, similar to that reported for **SPy-$(dT)_4$-SPy**.[47] This implies a large percentage of non-oxidized cofacial **SPy** dimers in the ensemble structures of **SPy-$(rU)_4$-SPy**. As the length increases from 4 to 8 and 16, the ratio dwindles. In the fluorescence spectra (Figures 2-3A and B), concomitant with the variance in absorbance ratio of 345 nm to 360 nm, the excimer emission also shows dependence on nucleobases and length. This intramolecular excimer emission arises from the direct excitation of the non-oxidized cofacial **SPy** dimer formed in **SPy-ssRNA-SPy**, and additionally from the association of singlet excited-state **SPy** (^{1}**SPy***) generated after excitation with its neutral counterpart, **SPy**, located at the other end of the same **SPy-ssRNA-SPy** molecule. In line with the decrease of the absorbance ratio of 345 nm to 360 nm as the increase of **SPy-ssRNA-SPy** length, for both (rA)-composed and (rU)-

composed doubly **SPy**-modified ssRNAs, the intensity of excimer emission decreases as the length of ssRNA increases. The sequences of **SPy-(rU)$_n$-SPy** exhibited much higher excimer emission compared with (rA)$_n$, especially when n is 4 or 8. This suggests that such structures that the two-end-linked **SPys** form a cofacial **SPy** dimer predominate the structures of **SPy-(rU)$_4$-SPy** and **SPy-(rU)$_8$-SPy**. When comparing **SPy-(rU)$_n$-SPy** and the corresponding ssDNA counterpart, **SPy-(dT)$_n$-SPy**, we found the former is more likely to form non-oxidized cofacial **SPy** dimer than the latter.[47] The results suggested the higher flexibility of (rU)$_n$ sequences.

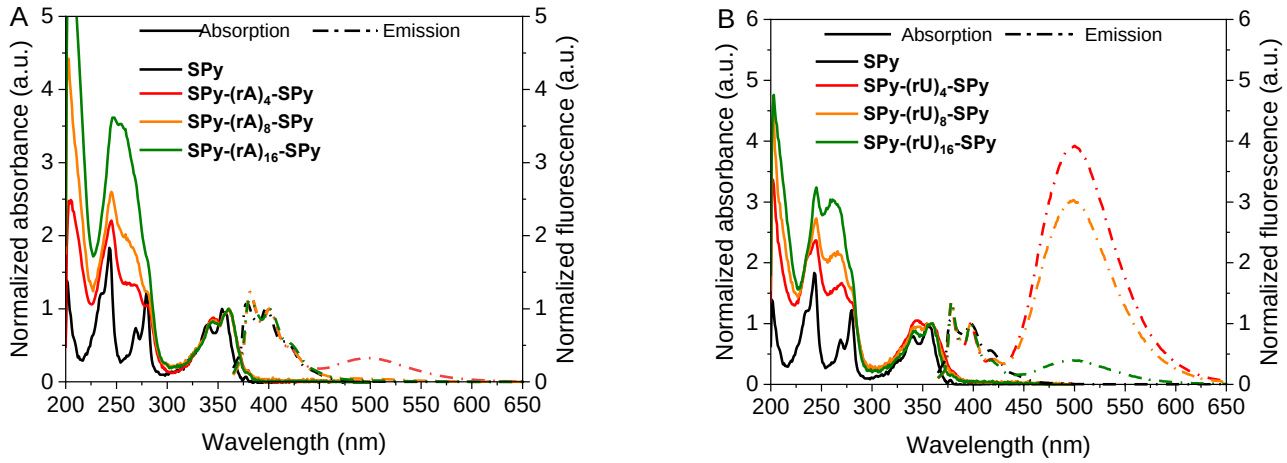

Figure 2-3. UV-vis absorption and fluorescence spectra of **SPy-ssRNA-SPy**. (A) **SPy-(rA)$_n$-SPy**. (B) **SPy-(rU)$_n$-SPy**, n = 4, 8, and 16. The fluorescence spectra were measured with excitation at 345 nm. The sample solution contained 1 μM **SPy-ssRNA-SPy** in 10 mM phosphate buffer solution (pH 7.0).

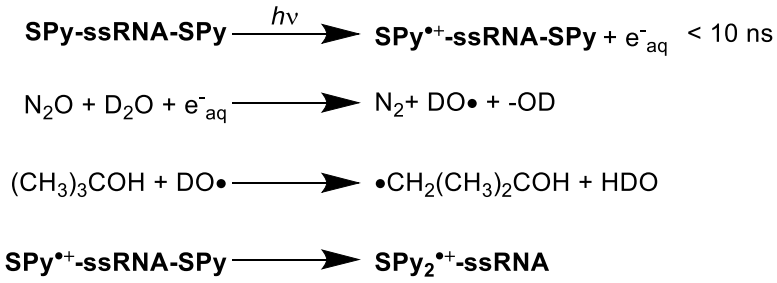

Scheme 2-1. Laser flash photolysis process of **SPy-ssRNA-SPy**.

The looping of ssRNA regulated by two end-linked **SPys** under photostimulation was explored using the laser flash photolysis technique. The formation of $\mathbf{SPy_2^{\bullet+}}$ is a consecutive reaction, as shown in Scheme 2-1. Upon excitation with two photons, one of the end-linked **SPy** was ionized to $\mathbf{SPy^{\bullet+}}$. The association of $\mathbf{SPy^{\bullet+}}$ with its neutral counterpart, **SPy** located at another end of the same molecule, gives rise to $\mathbf{SPy_2^{\bullet+}}$. Therefore, as $\mathbf{SPy^{\bullet+}}$ decays, $\mathbf{SPy_2^{\bullet+}}$ arises. Looping of ssRNA brings the pre-formed $\mathbf{SPy^{\bullet+}}$ located at one end of the molecule and its neutral counterpart, **SPy**, located at the other end of the same molecule close to each other with an interplanar distance of 3.1–3.6 Å.[58–61] The stabilization energy released during the association of $\mathbf{SPy^{\bullet+}}$ and **SPy**, in turn, provides a driving force for ssRNA looping.[47] As a result, by measuring the formation rate of $\mathbf{SPy_2^{\bullet+}}$, the information of photoregulated ssRNA looping dynamics is obtained. The corresponding bimolecular rate constant of **SPy** monomer is $(1.8 \pm 0.09) \times 10^9$ M^{-1} s^{-1}, in the same order of magnitude as the diffusion-controlled limit.[47] The fast dynamics originated from the fact that the energy level of ground-state $\mathbf{SPy_2^{\bullet+}}$ is lower than that of $\mathbf{SPy^{\bullet+}}$.[62]

It should be stressed that for the **SPy-ssRNA-SPy** molecules having such structural forms that the two end-linked **SPys** form a non-oxidized cofacial **SPy** dimer before photostimulation the **SPy** dimer would immediately give rise to $\mathbf{SPy_2^{\bullet+}}$ upon two-photon excitation. For these molecules, the observed totally formed $\mathbf{SPy_2^{\bullet+}}$ is comprised of the immediately formed component and the component formed by ssRNA looping occurring at a longer time scale.

From the time profiles shown in Figures 2-4A and B, it can be seen that the immediate $\mathbf{SPy_2^{\bullet+}}$-formation component appears for **SPy-(rA)$_4$-SPy** and all **SPy-(rU)$_n$-SPy** sequences. This is the manifestation of non-oxidized cofacial **SPy** dimer formed in the ensemble structures of these doubly **SPy**-modified ssRNA sequences before photostimulation. At the same time, a distinct slower $\mathbf{SPy_2^{\bullet+}}$-formation component was observed in the time profiles of all **SPy-(rA)$_n$-SPy** sequences and **SPy-(rU)$_{16}$-SPy**. The rate of this slower $\mathbf{SPy_2^{\bullet+}}$-formation component ($k\mathbf{SPy_2^{\bullet+}}$) is indicative of ssRNA looping dynamics (k_{looping}). After exponential fitting to the time profiles shown in Figures 2-4A and B, the looping dynamics of the doubly **SPy**-modified ssRNA was obtained (Table 2-1). The contribution of the immediate $\mathbf{SPy_2^{\bullet+}}$-formation component to the totally formed $\mathbf{SPy_2^{\bullet+}}$ was denoted by P_{static} (%). **SPy-(rA)$_4$-SPy** has a P_{static} of 45%, very close to that determined for the ssDNA counterpart, **SPy-(dA)$_4$-SPy** (42%).[47] The k_{looping} of **SPy-(rA)$_4$-SPy** is 0.55×10^6 s^{-1}. The looping rate decelerates to 1/3 and 1/14 as the length of ssRNA increases from

4 to 8 and 16 (Table 2-1), respectively. Different from **SPy-(rA)$_n$-SPy**, for **SPy-(rU)$_n$-SPy**, when n is 4 and 8, the slower **SPy$_2^{\bullet+}$**-formation component corresponding to the ssRNA looping dynamics is too small to be isolated from the dominated component, the immediate **SPy$_2^{\bullet+}$**-formation component. The P_{static} values for both are all over 80%. This is well correlated with the results of absorption and fluorescence spectra. When the length extends to 16, a negligible contribution from the immediate **SPy$_2^{\bullet+}$**-formation component to the totally formed **SPy$_2^{\bullet+}$** was found, and a $k_{looping}$ of 0.18×10^6 s^{-1} was determined. To corroborate that the observed looping dynamics herein is an intramolecular collision process, a concentration dependence study was carried out for **SPy-(rA)$_{16}$-SPy**. The independence of $k_{looping}$ on the concentration of **SPy-(rA)$_{16}$-SPy**, recorded at 20 μM, and 40 μM (Table 2-1 and Figure 2-5) validated that herein observed ssRNA looping dynamics is an intramolecular collision process.

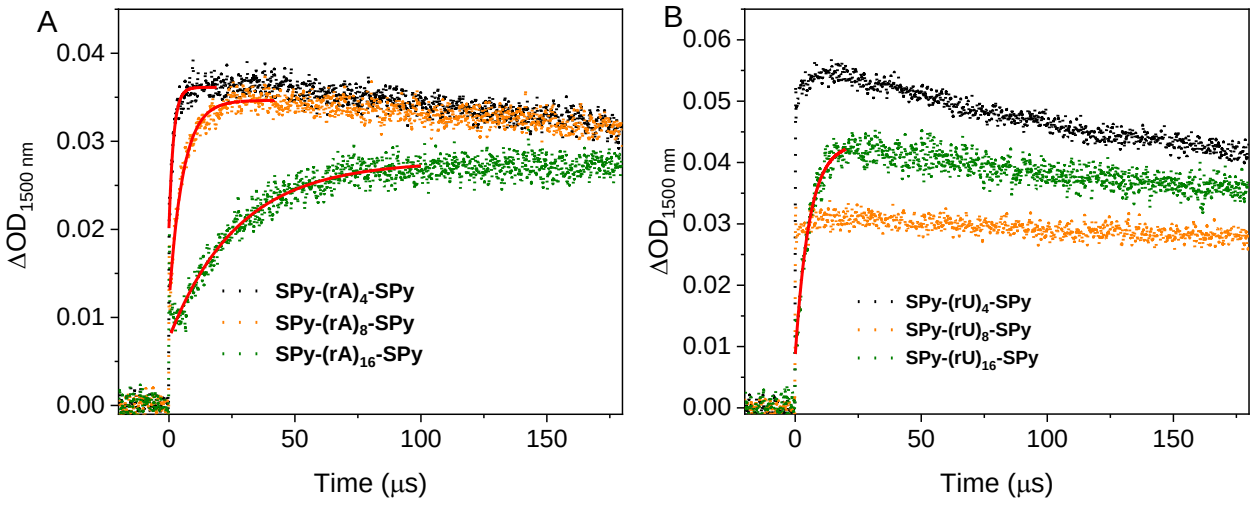

Figure 2-4. Time profiles of the transient absorption of **SPy$_2^{\bullet+}$** monitored at 1500 nm during the laser flash photolysis of **SPy-ssRNA-SPy**. (A) **SPy-(rA)$_n$-SPy**. (B) **SPy-(rU)$_n$-SPy**, n = 4, 8, and 16. The solid red line is a single-phase exponential fit to the experimental time profiles. The sample solution contained 40 μM **SPy-ssRNA-SPy** and 10 mM *t*-BuOH in 10 mM phosphate buffer solution (pD 7.0). The sample solution was N_2O-purged.

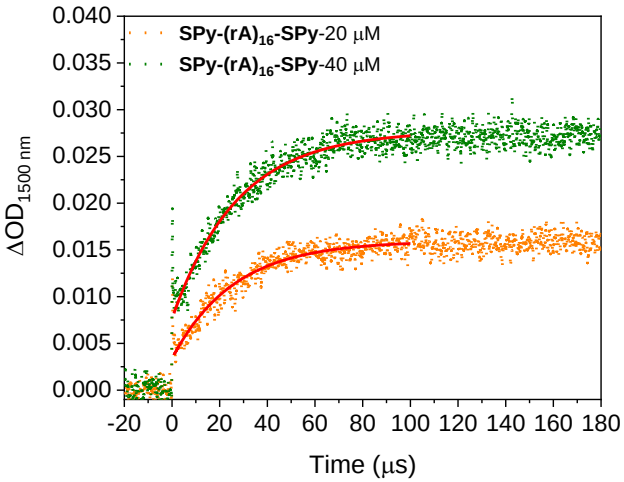

Figure 2-5. Time profiles of the transient absorption of $\mathbf{SPy_2^{\bullet+}}$ monitored at 1500 nm during the laser flash photolysis of **SPy-(rA)$_{16}$-SPy** at two different concentrations, 20 μM and 40 μM. The solid red line is a single-phase exponential fit to the experimental time profiles. The sample solution contained **SPy-(rA)$_{16}$-SPy** and 10 mM *t*-BuOH in 10 mM phosphate buffer solution (pD 7.0). The sample solution was N_2O-purged.

Table 2-1. Loop-formation rate $k_{looping}$ (1500 nm) and the population of immediately formed $\mathbf{SPy_2^{\bullet+}}$, P_{static}(%)[a]

Doubly **SPy**-modified ssRNA sequences	C (μM)	1500 nm $k_{looping}$ (10^6 s^{-1})	P_{static} (%)[a]
SPy-(rA)$_4$-SPy	40	0.55 ± 0.01	45
SPy-(rA)$_8$-SPy	40	0.18 ± 0.002	–
SPy-(rA)$_{16}$-SPy	40	0.037 ± 0.0003	–
	20	0.039 ± 0.0004	–
SPy-(rU)$_4$-SPy	40	–	>80
SPy-(rU)$_8$-SPy	40	–	>80
SPy-(rU)$_{16}$-SPy	40	0.18 ± 0.0003	–

[a] Immediately formed $\mathbf{SPy_2^{\bullet+}}$ component P_{static} (%) = $\Delta OD_{t=10\ ns}/\Delta OD_{max}$.

The looping dynamics observed herein for both (rA)-composed and (rU)-composed ssRNAs occurred at μs to tens of μs time scales, in the same range as the secondary structural dynamics in the hierarchical RNA dynamics occurring in biological processes.[21,30] In addition to the above-discussed length dependence, the results herein also indicate the nucleotide dependence of the looping dynamic of oligonucleotides. For all (rA)-composed doubly **SPy**-modified ssRNA sequences, the observed looping dynamics herein is subtly slower than their ssDNA counterpart, all with a typical difference of 1.3 times.[47] This identical trend suggests the role of ribose 2'-OH in ssRNA looping, since it is the sole chemical composition difference between DNA and RNA. The energy barrier involved in the end-to-end collision dynamics of a polymer is determined by both solvent friction and internal friction.[25,63–66] The ribose 2'-OH group in RNA could provide a basis for hydrogen bonding formation and hence induces extra hydrogen bond between it and the surrounding water molecules at low temperature,[67–70] or the nearby base, which is associated with the complex tertiary structure formation in RNA. The ribose 2'-OH is also known in connection with the important catalysis role of RNA. In view of the herein observed looping dynamics difference between **SPy-(rA)$_n$-SPy** and the corresponding ssDNA counterpart, the interaction between 2'-OH and the water molecules (D_2O) is apparently at the origin. The distribution of water molecules around biomolecules forms the hydration shells which is of critical structural and functional importance for biological systems.[68] The hydration pattern around 2'-OH site in **SPy-(rA)$_n$-SPy** is unknown. A few insights can be gained from the reported hydration sites around unpaired RNA nucleobases based on a statistical analysis of water molecule distribution in high-resolution X-ray structures of unpaired RNA nucleotides.[71] A water cluster is connected to the ribose ring of adenosine through interaction with O2' and O3' oxygen atoms, and a water cluster bridges the N3 nitrogen atom from adenosine and the oxygen atom from ribose 2'-OH.[71] However, the hydration shell is labile and dynamic.[68,72] Therefore, the weak interaction between ribose 2'-OH and the water molecule is probably the reason for the observed slightly retarded looping dynamics of **SPy-(rA)$_n$-SPy** relative to the corresponding ssDNA counterpart. Aside from this factor, two important facts during the looping of doubly **SPy**-modified ssRNA must be mentioned: i) oligonucleotide of polyadenine has high intrinsic rigidity and it's the energy cost for the internal friction that limits its end-to-end collision dynamics;[25,63] ii) The stabilization energy ($-\Delta H$ = 30–40 kJ mol^{-1}) released during the association of **SPy**$^{\bullet+}$ generated after photoionization of **SPy** located at one end of the modified ssRNA with its neutral counterpart,

SPy, located at the other end of the same molecule provides a driving force for the looping of ssRNA.[47] This driving force is probably similar to the energy barrier for the end-to-end collision of polyadenine sequences, according to the reported values of 46.7 kJ mol^{-1} for Dab(dT)-$(dA)_n$-(dT)Ru (n = 12, 15, 20, and 25, Dab = 4-Dimethylaminoazobenzene-4'-sulfonyl, Ru = Bis(2,2'-bipyridine)-4'-methyl-4-carboxybipyridine-ruthenium (II)) and 33 kJ mol^{-1} for DBO-$(dA)_4$-dG (DBO = 2,3-diazabicyclo[2.2.2]-oct-2-ene).[25,63] The above factors in all explain the restricted difference in looping dynamics between **SPy-$(rA)_n$-SPy** and **SPy-$(dA)_n$-SPy**. Contrary to **SPy-$(rA)_n$-SPy**, slightly enhanced looping dynamics was observed for **SPy-$(rU)_{16}$-SPy** relative to **SPy-$(dT)_{16}$-SPy**. The effect of ribose 2'-OH hydration is believed to hold true for (rU)-composed sequences.[71,72] However, since this effect is weak, the energy cost to overcome the solvent friction which is the control factor during the end-to-end collision of polypyrimidine sequences is not much influenced by this effect. Moreover, the above-mentioned stabilization energy is enough to overcome the energy barrier during the looping of polypyrimidine sequences. Compared with the activation energy for solvent viscous flow in H_2O and the reported activation energy of Dab(dT)-$(dT)_n$-(dT)Ru (n = 12, 15, 20, and 25), which are around 16 kJ mol^{-1} (the value is believed slightly higher in D_2O) and 27.7 kJ mol^{-1}, respectively, the driving force is sufficient.[25,63] Therefore, retarded dynamics is not observed for **SPy-$(rU)_{16}$-SPy**. The slightly enhanced looping dynamics of **SPy-$(rU)_{16}$-SPy** relative to **SPy-$(dT)_{16}$-SPy** is most probably correlated with the absence of C5-CH_3 group in uracil base, which can lead to extra steric hindrance when bond rotations (internal friction) occur in the dynamics of $(dT)_n$ sequences[63] as observed by Nau *et al.* that the end-to-end collision rate of DBO-$(dU)_4$-G is 1.5 times as fast as DBO-$(dT)_4$-G.[63]

The nucleotide dependence of the looping dynamics of oligonucleotides is manifested not only on the difference between ssRNA and the corresponding ssDNA counterpart but also on the difference between pyrimidine sequences and purine sequences, as observed in our previous works and other DNA works.[25,47,49,63] In this work, the looping dynamics of **SPy-$(rU)_{16}$-SPy** is 5 times as fast as **SPy-$(rA)_{16}$-SPy**. This is consistent with the common observation that the end-to-end collision of polypurine sequences is dominated by solvent friction with a faster collision rate, while the dynamics of polypyrimidine sequences is limited by internal friction with a slower collision rate.

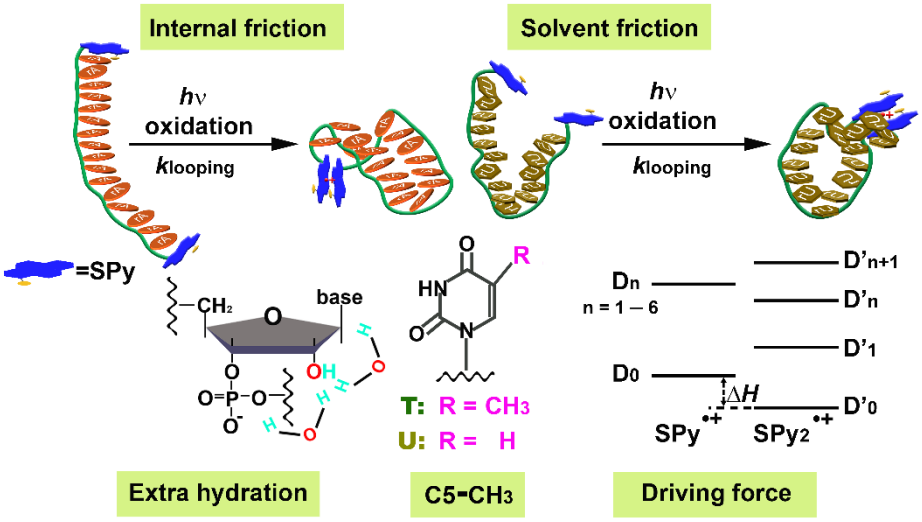

Scheme 2-2. Schematic illustration of the main factors affecting the looping dynamics of ssRNA regulated by **SPy** upon photostimulation. The looping dynamics differ substantially with respect to the intrinsic flexibility or rigidity of oligonucleotides, which determines the looping to be limited by internal friction or solvent friction. The extra hydration around ribose 2'-OH in ssRNA causes a retarding effect on looping dynamics. Lack of C5-CH_3 group in uracil base grants polyuracil sequences higher flexibility and thereby faster looping dynamics than polythymine sequences. $\mathbf{SPy_2}^{\bullet+}$ is energetically more stable than $\mathbf{SPy}^{\bullet+}$[62] and this provides a driving force for oligonucleotide looping.

Take collectively and given the fact that the stabilization energy released during the association of $\mathbf{SPy}^{\bullet+}$ with its neutral counterpart, **SPy**, offers a driving force of 30–40 kJ mol^{-1} for the looping of oligonucleotides, the above results suggest: i) the retarding effect of ribose 2'-OH on the looping dynamics of short ssRNA; ii) the retarding effect leads to a subtle change in looping dynamics between short ssRNA and ssDNA; iii) the extra hydration around ribose 2'-OH can not take over from the intrinsic rigidity or flexibility of an oligonucleotide to control the looping dynamics of short ssRNA; iv) the polyuracil sequences are more intrinsically flexible than polythymine sequences, due to lack of C5-CH_3 group; the effect of nucleotide on the looping dynamics of oligonucleotides displays an order of dU > rU > dT > dA > rA.[63] The looping dynamics of doubly **SPy**-modified oligonucleotides are determined by the combined effects from

solvent friction, internal friction, the extra hydration at ribose 2'-OH, C5-CH_3 group, and the regulation by **SPys**, as depicted in Scheme 2-2.

Conclusion

In this work, we explored the looping dynamics of ssRNA using sulfonated pyrene, **SPy**, as both a probe and a photoregulator. Two **SPys** were end-linked to both the 5'-end and 3'-end positions of ssRNA by flexible alkyl chains. Upon photoirradiation, $\mathbf{SPy}^{\bullet+}$ was first generated at one end of the doubly **SPy**-modified ssRNA. Then $\mathbf{SPy}^{\bullet+}$ associated with its neutral counterpart, **SPy** located at the other end of the same molecule, to form $\mathbf{SPy_2}^{\bullet+}$, because $\mathbf{SPy_2}^{\bullet+}$ is energetically more stable. The released stabilization energy during the association process provides a driving force for ssRNA looping. The looping dynamics of ssRNA regulated by **SPy** was studied by laser flash photolysis technique. The results observed herein in doubly **SPy**-modified $(rA)_n$ show retarded looping dynamics relative to the corresponding ssDNA counterpart, all with the same difference of 1.3 times. Contrarily, the end-to-end collision rate of **SPy-(rU)$_{16}$-SPy** is 1.3 times faster than **SPy-(dT)$_{16}$-SPy**. A thorough discussion of the difference in looping dynamics between ssRNA and ssDNA is made by taking into account the extra hydration of ribose 2'-OH, the intrinsic flexibility or rigidity of oligonucleotides, and the driving force associated with $\mathbf{SPy_2}^{\bullet+}$ formation. The extra hydration around ribose 2'-OH gives rise to a retarding effect on the looping dynamics of ssRNA in comparison with the corresponding ssDNA counterpart. However, the intrinsic rigidity or flexibility is the decisive factor for the dynamics of doubly **SPy**-modified oligonucleotides. The faster looping dynamics of **SPy-(rU)$_{16}$-SPy** compared with **SPy-(dT)$_{16}$-SPy** presents direct proof that $(rU)_n$ sequences move faster than $(dT)_n$ sequences in solution. This correlates with the higher flexibility of polyuracil sequences which is due to the absence of C5-CH_3 group in uracil base and demonstrates the slowing down effect of C5-CH_3 group in thymine base on the dynamics of polythymine sequences. The herein observed effects of extra hydration around ribose 2'-OH group and C5-CH_3 group on ssRNA looping dynamics offer valuable experimental evidence on the role of 2'-OH and C5-CH_3 in RNA flexibility and structural transition dynamics.

Experimental Section

Materials. All reagents and solvents were purchased from the standard suppliers and used without further purification. 5', 3'-Bis(3-aminopropyl) bis(phosphate)-modified ssRNAs were purchased from GeneDesign, Inc. and used as received without further purification.

Synthesis of SPy-ssRNA-SPy. SPy-ssRNA-SPy was prepared in the same way as described in Chapter 1.[47] The reverse-phase HPLC settings for analysis and isolation of **SPy-ssRNA-SPy** are shown in Table 2-2. The purity of the prepared sequence was checked by reverse-phase HPLC (Figure 2-6).

Table 2-2. HPLC settings for analysis and isolation of **SPy-ssRNA-SPy**

<table>
<tr><td colspan="4">Reverse-phase HPLC settings</td></tr>
<tr><td></td><td colspan="2">Analysis</td><td>Purification</td></tr>
<tr><td>Column</td><td colspan="2">5C18-AR-II, 1.0 mm I.D. × 15 cm, particle size of 5 μm (nacalai tesque, Japan)</td><td>5C18-AR-II, 10.0 mm I.D. × 15 cm, particle size of 5 μm (nacalai tesque, Japan)</td></tr>
<tr><td>Flow rate</td><td colspan="2">1 mL / min</td><td>4 mL / min</td></tr>
<tr><td>Detection wavelength</td><td colspan="3">340 nm, 260 nm</td></tr>
<tr><td>Column temperature</td><td colspan="3">40 ℃</td></tr>
<tr><td rowspan="2">Mobile phase</td><td colspan="3">acetonitrile</td></tr>
<tr><td colspan="2">100 mM Triethylammonium acetate buffer</td><td>50 mM ammonium formate solution</td></tr>
<tr><td>Gradient elution</td><td colspan="2">acetonitrile from 5% to 65%
in 20 min</td><td>acetonitrile from 5% to 20%
in 40 min</td></tr>
</table>

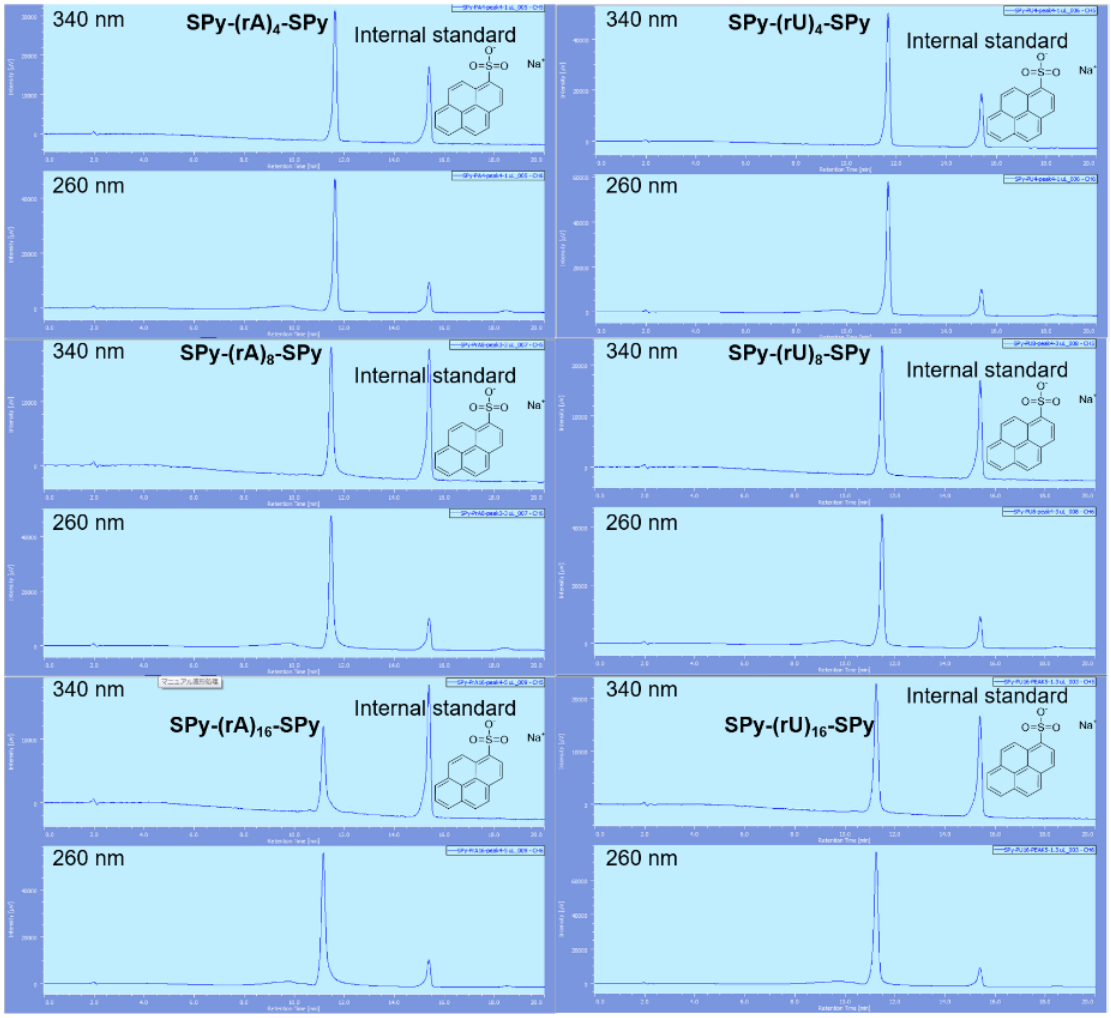

Figure 2-6. HPLC chromatograms of **SPy-ssRNA-SPy**. Left: **SPy-(rA)$_n$-SPy**; right: **SPy-(rU)$_n$-SPy**, n = 4, 8, and 16. The HPLC settings are shown in Table 2-2.

Identification of SPy-ssRNA-SPy. SPy-ssRNA-SPy was identified as the same as described in Chapter 1.

Table 2-3. MALDI-TOF-MS results of **SPy-ssRNA-SPy**

Doubly **SPy**-modified ssRNA sequences	Formula	Calculated	Found (m/z)
SPy-(rA)$_4$-SPy	$C_{86}H_{93}N_{22}O_{36}P_5S_2$	2228.425	2229.889
SPy-(rA)$_8$-SPy	$C_{126}H_{141}N_{42}O_{60}P_9S_2$	3544.635	3548.870
SPy-(rA)$_{16}$-SPy	$C_{206}H_{237}N_{82}O_{108}P_{17}S_2$	6177.055	6173.101
SPy-(rU)$_4$-SPy	$C_{82}H_{89}N_{10}O_{44}P_5S_2$	2136.316	2137.157
SPy-(rU)$_8$-SPy	$C_{118}H_{133}N_{18}O_{76}P_9S_2$	3360.418	3363.888
SPy-(rU)$_{16}$-SPy	$C_{190}H_{221}N_{34}O_{140}P_{17}S_2$	5808.620	5812.672

UV-vis absorption and fluorescence spectra measurement. The UV-vis absorption and fluorescence spectra were measured as the same as described in Chapter 1.

Laser flash photolysis measurement. The measurement was carried out as the same as described in Chapter 1.

References

[1] E. Harrison, *"The Versatility of RNA."Operators and Promoters: The Story of Molecular Biology and Its Creators*, University Of California Press, Berkeley, **2001,** p. 218.

[2] M. G. Caprara, T. W. Nilsen, *Nat. Struct. Biol.* **2000**, *7*, 831–833.

[3] H. H. Gan, S. Pasquali, T. Schlick, *Nucleic Acids Res.* **2003**, *31*, 2926–2943.

[4] R. T. Batey, R. P. Rambo, J. A. Doudna, *Angew. Chem. Int. Ed.* **1999**, *38*, 2326–2343.

[5] R. C. Spitale, R. A. Flynn, E. A. Torre, E. T. Kool, H. Y. Chang, *WIREs RNA* **2014**, *5*, 867–881.

[6] S. Klinge, J. L. Woolford, *Nat. Rev. Mol. Cell Biol.* **2019**, *20*, 116–131.

[7] H. F. Noller, L. Lancaster, S. Mohan, J. Zhou, *Q. Rev. Biophys.* **2017**, *50*, e12.

[8] S. A. Strobel, J. C. Cochrane, *Curr. Opin. Chem. Biol.* **2007**, *11*, 636–643.

[9] M. Mandal, R. R. Breaker, *Nat. Rev. Mol. Cell Biol.* **2004**, *5*, 451–463.

[10] M. Esteller, *Nat. Rev. Genet.* **2011**, *12*, 861–874.

[11] W. Wei, Z. Ba, M. Gao, Y. Wu, Y. Ma, S. Amiard, C. I. White, J. M. R. Danielsen, Y.-G. Yang, Y. Qi, *Cell* **2012**, *149*, 101–112.

[12] S. Francia, F. Michelini, A. Saxena, D. Tang, M. de Hoon, V. Anelli, M. Mione, P. Carninci, F. d'Adda di Fagagna, *Nature* **2012**, *488*, 231–235.

[13] K. M. Michalik, R. Böttcher, K. Förstemann, *Nucleic Acids Res.* **2012**, *40*, 9596–9603.

[14] F. Storici, A. E. Tichon, *Nat. Cell Biol.* **2017**, *19*, 1382–1384.

[15] S. Francia, M. Cabrini, V. Matti, A. Oldani, F. d'Adda di Fagagna, *J. Cell Sci.* **2016**, *129*, 1468–1476.

[16] F. d'Adda di Fagagna, *Trends Cell Biol.* **2014**, *24*, 171–178.

[17] F. Michelini, S. Pitchiaya, V. Vitelli, S. Sharma, U. Gioia, F. Pessina, M. Cabrini, Y. Wang, I. Capozzo, F. Iannelli, V. Matti, S. Francia, G. V. Shivashankar, N. G. Walter, F. d'Adda di Fagagna, *Nat. Cell Biol.* **2017**, *19*, 1400–1411.

[18] M. Huarte, *Nat. Med.* **2015**, *21*, 1253–1261.

[19] Y. Mao, S.-B. Qian, *Nat. Cell Biol.* **2020**, *22*, 141–142.

[20] E. A. Dethoff, J. Chugh, A. M. Mustoe, H. M. Al-Hashimi, *Nature* **2012**, *482*, 322–330.

[21] A. M. Mustoe, C. L. Brooks, H. M. Al-Hashimi, *Annu. Rev. Biochem.* **2014**, *83*, 441–466.

[22] A. Ansari, S. V Kuznetsov, Y. Shen, *Proc. Natl. Acad. Sci. USA* **2001**, *98*, 7771–7776.

[23] S. V. Kuznetsov, A. Ansari, *Biophys. J.* **2012**, *102*, 101–111.

[24] A. Ansari, S. V Kuznetsov, *J. Phys. Chem. B* **2005**, *109*, 12982–12989.

[25] T. Uzawa, T. Isoshima, Y. Ito, K. Ishimori, D. E. Makarov, K. W. Plaxco, *Biophys. J.* **2013**, *104*, 2485–2492.

[26] K. Sarkar, K. Meister, A. Sethi, M. Gruebele, *Biophys. J.* **2009**, *97*, 1418–1427.

[27] T. Uzawa, R. R. Cheng, K. J. Cash, D. E. Makarov, K. W. Plaxco, *Biophys. J.* **2009**, *97*, 205–210.

[28] K. Neupane, D. B. Ritchie, H. Yu, D. A. N. Foster, F. Wang, M. T. Woodside, *Phys. Rev. Lett.* **2012**, *109*, 68102.

[29] J. Jung, A. Van Orden, *J. Am. Chem. Soc.* **2006**, *128*, 1240–1249.

[30] H. M. Al-Hashimi, N. G. Walter, *Curr. Opin. Struct. Biol.* **2008**, *18*, 321–329.

[31] M. J. E. Resendiz, A. Schön, E. Freire, M. M. Greenberg, *J. Am. Chem. Soc.* **2012**, *134*, 12478–12481.

[32] T. M. Figueira-Duarte, K. Müllen, *Chem. Rev.* **2011**, *111*, 7260–7314.

[33] G. Bains, A. B. Patel, V. Narayanaswami, *Molecules.* **2011**, *16*, 7909–7935.

[34] J. Duhamel, *Langmuir* **2012**, *28*, 6527–6538.

[35] H. Tang, C. S. de Oliveira, G. Sonntag, C. L. D. Gibb, B. C. Gibb, C. Bohne, *J. Am. Chem. Soc.* **2012**, *134*, 5544–5547.

[36] D. Sahoo, V. Narayanaswami, C. M. Kay, R. O. Ryan, *Biochemistry* **2000**, *39*, 6594–6601.

[37] A. B. Patel, P. Khumsupan, V. Narayanaswami, *Biochemistry* **2010**, *49*, 1766–1775.

[38] C. Mizuguchi, M. Hata, P. Dhanasekaran, M. Nickel, M. C. Phillips, S. Lund-Katz, H. Saito, *Biochemistry* **2012**, *51*, 5580–5588.

[39] T. Hall, G. Whitton, R. Casier, M. Gauthier, J. Duhamel, *Macromolecules* **2018**, *51*, 7914–7923.

[40] S. Karuppannan, J.-C. Chambron, *Chem. Asian J.* **2011**, *6*, 964–984.

[41] R. Casier, J. Duhamel, *Macromolecules* **2018**, *51*, 3450–3457.

[42] G. K. Bains, S. H. Kim, E. J. Sorin, V. Narayanaswami, *Biochemistry* **2012**, *51*, 6207–6219.

[43] J. B. Birks, D. J. Dyson, I. H. Munro, B. H. Flowers, *Proc. R. Soc. London. Ser. A. Sci.* **1963**, *275*, 575–588.

[44] D. A. Van Dyke, B. A. Pryor, P. G. Smith, M. R. Topp, *J. Chem. Educ.* **1998**, *75*, 615.

[45] M. Hara, S. Tojo, K. Kawai, T. Majima, *Phys. Chem. Chem. Phys.* **2004**, *6*, 3215–3220.

[46] P. C. Johnson, H. W. Offen, *J. Chem. Phys.* **1973**, *59*, 801–806.

[47] J. Xu, S. Miyamoto, S. Tojo, K. Kawai, *Chem. Eur. J.* **2020**, 26, 5075-5084.

[48] W. M. Nau, X. Wang, *ChemPhysChem* **2002**, *3*, 393–398.

[49] K. Kawai, H. Yoshida, A. Sugimoto, M. Fujitsuka, T. Majima, *J. Am. Chem. Soc.* **2005**, *127*, 13232–13237.

[50] K. Kawai, K. Miyamoto, S. Tojo, T. Majima, *J. Am. Chem. Soc.* **2003**, *125*, 912–915.

[51] K. Kawai, H. Yoshida, T. Takada, S. Tojo, T. Majima, *J. Phys. Chem. B* **2004**, *108*, 13547–13550.

[52] N. Getoff, S. Solar, U.-B. Richter, M. W. Haenel, *Radiat. Phys. Chem.* **2003**, *66*, 207–214.

[53] M. A. J. Rodgers, *Chem. Phys. Lett.* **1971**, *9*, 107–108.

[54] K. Y. Paek, K. Y. Hong, I. Ryu, S. M. Park, S. J. Keum, O. S. Kwon, S. K. Jang, *Proc. Natl. Acad. Sci. USA* **2015**, *112*, 1041–1046.

[55] I. BerIman, *Handbook of Fluorescence Spectra of Aromatic Molecules*, Academic Press, **2012**.

[56] I. Benkyi, E. Tapavicza, H. Fliegl, D. Sundholm, *Phys. Chem. Chem. Phys.* **2019**, *21*, 21094–21103.

[57] C. M. Jones, S. A. Asher, *J. Chem. Phys.* **1988**, *89*, 2649–2661.

[58] T. Devic, M. Yuan, J. Adams, D. C. Fredrickson, S. Lee, D. Venkataraman, *J. Am. Chem. Soc.* **2005**, *127*, 14616–14627.

[59] M. Jørgensen, T. Bjørnholm, K. Bechgaard, *Synth. Met.* **1990**, *38*, 77–86.

[60] J. K. Kochi, R. Rathore, P. Le Maguères, *J. Org. Chem.* **2000**, *65*, 6826–6836.

[61] J. Hoche, H.-C. Schmitt, A. Humeniuk, I. Fischer, R. Mitrić, M. I. S. Röhr, *Phys. Chem. Chem. Phys.* **2017**, *19*, 25002–25015.

[62] S. Samori, M. Fujitsuka, T. Majima, *Res. Chem. Intermed.* **2013**, *39*, 449–461.

[63] X. Wang, W. M. Nau, *J. Am. Chem. Soc.* **2004**, *126*, 808–813.

[64] P. G. de Gennes, *Scaling Concepts in Polymer Physics*, Cornell University Press, Ithaca, NY, **1979**.

[65] C. W. Manke, M. C. Williams, *Macromolecules* **1985**, *18*, 2045–2051.

[66] A. Soranno, B. Buchli, D. Nettels, R. R. Cheng, S. Müller-Späth, S. H. Pfeil, A. Hoffmann, E. A. Lipman, D. E. Makarov, B. Schuler, *Proc. Natl. Acad. Sci. USA* **2012**, *109*, 17800–17806.

[67] P. H. Bolton, D. R. Kearns, *Biochim. Biophys. Acta - Nucleic Acids Protein Synth.* **1978**, *517*, 329–337.

[68] P. Kührová, M. Otyepka, J. Šponer, P. Banáš, *J. Chem. Theory Comput.* **2014**, *10*, 401–411.

[69] J. Fohrer, M. Hennig, T. Carlomagno, *J. Mol. Biol.* **2006**, *356*, 280–287.

[70] A. Kundu, J. Schauss, B. P. Fingerhut, T. Elsaesser, *J. Phys. Chem. B* **2020**, *124*, 2132–2138.

[71] S. Kirillova, O. Carugo, *BMC Struct. Biol.* **2011**, *11*, 41.

[72] P. Auffinger, E. Westhof, *J. Mol. Biol.* **1997**, *269*, 326–341.

Chapter 3. Control of Triplet Blinking Using 1,3,5,7-Cyclooctatetraene to Access the Dynamics of Biomolecules at the Single-Molecule Level

Abstract

The triplet excited electronic state (T_1) of a fluorescent molecule has a longer lifetime (> 10^{-3} s) compared with the singlet excited electronic state (S_1, $\tau = 10^{-9}$–10^{-6} s). This makes it possible to use the T_1 state of a fluorescent molecule to access biomolecular conformational dynamics occurring at timescales from 10^{-6} to 10^{-3} s. Since a fluorescent molecule in the T_1 state does not emit, emission can only be observed after it goes back to the ground electronic state (S_0). By controlling the time it takes for the fluorescent molecule in the T_1 state to go back to the S_0 state, triplet blinking will be observed. If the time is governed by biomolecular conformational dynamics, by monitoring the kinetics of the triplet blinking of a fluorescent molecule, biomolecular conformational dynamics will be accessed. Herein, we demonstrate that by using 1,3,5,7-cyclooctatetraene (COT) as a triplet acceptor, the triplet blinking of ATTO 647N can be used to access biomolecular conformational dynamics. The herein observed significant roles of COT—as both a controller controlling triplet blinking and a photostabilizer protecting a fluorescent molecule from photobleaching—offers a way to employ triplet blinking to access biomolecular conformational dynamics at a long timescale and single-molecule level.

Introduction

Photoinduced reactions of molecules that can be controlled in a spatio-temporal fashion play an important role in fluorescent molecule-involved applications, such as bioimaging,[1–8] sensing and diagnosing,[9–13], *etc*. For a fluorescent molecule, after absorbing a photon with a certain energy, it will be excited from its ground electronic state (S_0) to the excited electronic states. Because the singlet excited electronic state (S_1) is energetically favored, the fluorescent molecule will have a dominated population in the S_1 state. The fluorescent molecule will emit a photon with energy less than the absorbed photon when it relaxes from the S_1 state to the S_0 state. Apart from emission, other reactions and radiationless transitions can occur when the fluorescent molecule is in its S_1 state, which competes with the emission process. For example, since the fluorescent molecule in the S_1 state is both a potent reducing agent and a potent oxidizing agent, an electron

transfer (ET) reaction can take place. The occurrence of ET is environment-dependent. Therefore, by studying the kinetics of ET, the surrounding local microenvironment that governs ET kinetics can be accessed. By using ET, Sunney *et al.* have studied the conformational dynamics of flavin reductase during it-catalyzed reduction of Flavin cofactors (Flavin mononucleotide, FMN, and Flavin adenine dinucleotide, FAD) by a nearby tyrosine residue.[14] However, because the lifetime of the S_1 state of a fluorescent molecule is usually at 10^{-8} s timescale, biomolecular conformational dynamics occurring at long timescales, such as conformational transitions of protein or RNA, both of which feature a hierarchy in conformational dynamics ranging from ps to s timescales,[15–17] can not be accessed by using S_1-based techniques, such as ET used by Sunney *et al.*[14]

The radiationless transition for a fluorescent molecule in the S_1 state during which process the spin symmetry of the state has a change is termed intersystem crossing (ISC).[18] ISC makes the fluorescent molecule go to its triplet electronic state (T_1). Since the spin symmetry has a change from S_1 to T_1, it is a spin-forbidden process and the lifetime of the T_1 state is relatively long, > 10^{-3} s. If the T_1 state can be used to access biomolecular conformational dynamics, a long timescale study from 10^{-6} to 10^{-3} s will be accessible, which is 10^5 times longer than using S_1-based techniques. To use the T_1 state of a fluorescent molecule to study biomolecular formational dynamics, T_1-involved triplet-triplet energy transfer (TTET) process, which is a process of exchanging both spin and energy between a triplet donor and triplet acceptor[19] and the most useful reaction via T_1 state, is brought into play. Since TTET is a short-range energy transfer and it typically occurs within a Van der Waals contact between the triplet donor and triplet acceptor, it can be used for accessing conformation change on the subnanometer scale, which is complementary to the widely used fluorescence resonance energy transfer (FRET) technique.[14] By using a xanthone moiety as a triplet donor and naphthylalanine as a triplet acceptor, Kiefhaber *et al.* have investigated the loop formation dynamics in polypeptide chains from 10^{-12} to 10^{-5} s timescales.[20–23] However, the kinetics of TTET was studied by laser flash photolysis technique which demands a substantial amount of samples (C = 20–100 μM). The requirement of the sample amount for laser flash photolysis measurement limits its use for precious samples, such as artificial mutant samples.

Compared with the laser flash photolysis technique, the fluorescence-based techniques are more preferable to biomolecular samples. On one hand, a minuscule amount of sample is enough

for the measurement, and measurement at the single-molecule level is receiving increased attention. On the other hand, it is less invasive to biomolecules than laser flash photolysis. Thus, distinctive from laser flash photolysis, by using a tiny amount of sample, the kinetics of TTET between a fluorescent molecule and a triplet acceptor can be obtained by monitoring the fluctuation of fluorescence signals at the single-molecule level. This is because TTET kinetics controls the switching of a fluorescent molecule from a non-emission state to an emission state. When the fluorescent molecule undergoes repetitive excitation and emission cycles, fluorescence is observed and it is called ON state. Occasionally, the fluorescent molecule goes to the T_1 state through ISC. Because of the long lifetime of the T_1 state, the fluorescent molecule in the T_1 state doesn't emit until it goes back to the S_0 state. The state when the fluorescent molecule doesn't emit is called the OFF state. The duration of the ON state and OFF state are denoted as τ_{ON} and τ_{OFF}, respectively. When the fluorescent molecule repeatedly switches between the ON state and OFF state, it is called fluorescence blinking. When ISC is the cause for the fluorescent molecule to go to OFF (T_1) state from ON (S_1) state, it is called triplet blinking. In triplet blinking, the time it takes for the fluorescent molecule to go back to the S_0 state from the T_1 state can be measured as τ_{OFF}. The occurrence of TTET shortens the T_1 lifetime of the fluorescent molecule. The kinetics of TTET between a fluorescent molecule and a triplet acceptor determines τ_{OFF}. Therefore, by measuring τ_{OFF}, TTET kinetics between a fluorescent molecule and a triplet acceptor can be obtained. When TTET kinetics is governed by biomolecular conformational dynamics, τ_{OFF} reflects the conformational dynamics of biomolecules.

Fluorescence correlation spectroscopy (FCS) is such a technique based on analyzing the fluctuation of the fluorescence signal (Scheme 3-1). It is a time-averaging fluorescence fluctuation analysis of small molecular ensembles with maximum sensitivity and high statistical confidence.[24] Fluctuation of the fluorescence signal is analyzed using the normalized fluctuation autocorrelation function $G(\tau)$.

$$G(\tau) = \langle \delta F(t)\ \delta F(t+\tau) \rangle / \langle F(t) \rangle^2 \qquad \text{Equation (3-1)}$$

Where $\delta F(t)$ is the fluctuation of the fluorescence signal at time t, and it is defined as the difference between the fluorescence intensity at time t and its average,

$$\delta F(t) = F(t) - \langle F(t) \rangle \text{ and } \langle F(t) \rangle = \frac{1}{T}\int_0^T F(t)dt \qquad \text{Equation (3-2)}$$

Normalized fluctuation autocorrelation $G(\tau)$ is therefore a temporal average of the fluctuation of

fluorescence intensity δF at a given time t multiplied by δF at a later time $t + \tau$, normalized by the square of the average fluorescence intensity over the acquisition time T.[25] The autocorrelation provides a measure of the self-similarity of a time signal after the lag time τ and reveals the characteristic time constants of the underlying processes.[25]

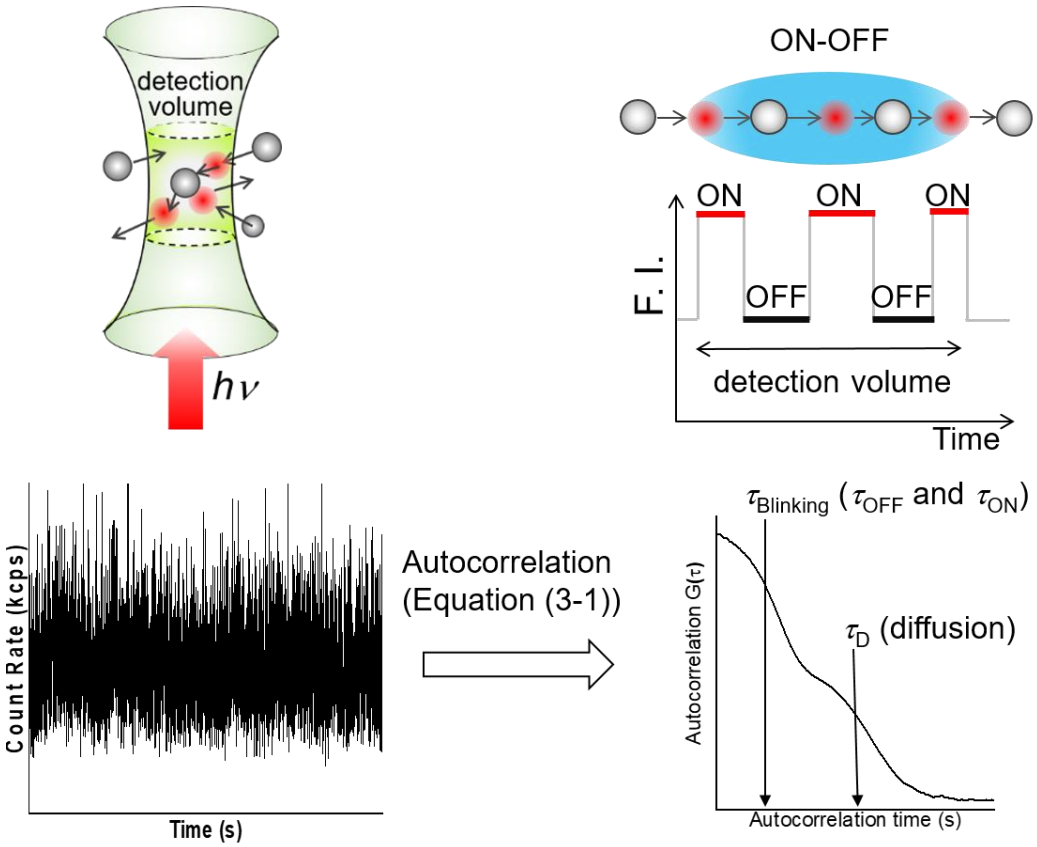

Scheme 3-1. Illustrative scheme of the principle of FCS based on a confocal microscope setup. When fluorescent molecules go through the detection volume, the random diffusions or the internal dynamics or reactions of molecules induce fluctuation of the fluorescence signal, for example, fluorescence ON-OFF cycles (top). Fluctuation of the fluorescence signal is analyzed using normalized fluctuation autocorrelation function $G(\tau)$ (Equation 3-1). The obtained FCS autocorrelation curves describe the temporal decay function of fluorescence fluctuations, from which the characteristic times having a contribution to the fluctuation of fluorescence intensity, such as τ_{OFF}, τ_{ON}, and τ_D can be obtained (bottom).

Fluctuation of the fluorescence signal can be induced by fluorescence molecules entering and leaving the detection volume (illuminated region) with random diffusion, or by reversible changes in the fluorescence capacity during a fluorescent molecule's residence time which is attributed to intramolecular or intermolecular reactions, or by reversible changes in the microenvironment of the fluorescent molecule,[24] such as having a or no close contact with a triplet acceptor. The timescale for a close contact to occur between a fluorescent molecule in its T_1 state and a triplet acceptor determines the kinetics of TTET between them and is governed by the biomolecular conformational dynamics when the biomolecule is harnessed by a fluorescent molecule and a triplet acceptor. For this reason, the blinking time obtained by FCS measurement reveals the conformational dynamics of biomolecules. The detection volume in FCS measurement is typically less than 1 μm^3 and less than 1 pmol of sample is enough for the measurement. By immobilizing the molecule on the glass surface, blinking from a single fluorescent molecule can be obtained. As a result, triplet blinking measured by FCS can be employed for ultrasensitive sensing and diagnosing.

O_2 is unique since it has a triplet electronic structure in the ground state and therefore serves as an efficient triplet acceptor. However, this TTET results in the formation of singlet oxygen ($^1O_2$).[26] $^1O_2$ is a very potent oxidizing agent and the formation of $^1O_2$ is the key mechanism of action in photodynamic therapy (PDT, type II).[27] By the same token, $^1O_2$ causes photo-bleaching of the fluorescent molecule. Thus, the depopulation of T_1 to inhibit photo-bleaching and enhance photostability of the fluorescent molecule is highly desired in fluorescence microscopy, especially in the measurement at the single-molecule level.[26]

An efficient triplet acceptor should have a low energy level of T_1 state and a high energy level of S_1 state, which provides the electronic coupling strength for TTET to occur. Moreover, the lifetime of the T_1 state of the triplet acceptor should be short enough to make the triplet acceptor quickly go back to its S_0 state for use in the next TTET turn. 1,3,5,7-cyclooctatetraene (COT), which has been one of the most popular and efficient triplet acceptors in organic liquid dye lasers,[28,29] fulfills the above-mentioned requirements. COT is a cyclic, very flexible nonaromatic polyene in the S_0 state. It shows nonvertical behavior during energy transfer.[30,31] The nonvertical excitation transfer process was envisioned as proceeding with a simultaneous change in the geometry of the acceptor to reach a distorted, "phantom", nonspectroscopic state.[32] As shown in

Scheme 3-2, COT in its S_0 state is reported having a boat (D_{2d}) conformation.[30,31,33] During TTET concerted C=C stretching and C-C torsional vibrations make the boat conformation distorted favoring a more planar geometry (a flat octagonal D_{8h} was predicted).[30,31,33] Due to the distortion, the triplet COT (^{3}COT) relaxes to a state the energy level of which is as low as 0.8 eV.[30,31] This decreases the energy required to populate ^{3}COT.[31] Besides, ^{3}COT has a short lifetime at the timescale of 10^{-4} s.[30,31] Therefore, COT is an efficient triplet acceptor.[30,31,33] In stark contrast to O_2, which leads to photobleaching when serving as a triplet acceptor, COT can enhance both the fluorescence intensity and photostability, which has been reported by Blanchard *et al.* through proximal conjugation of COT to the cyanine fluorophore Cy5.[34] Compared with other triplet acceptors, such as 4-nitrobenzyl alcohol, Trolox, ascorbic acid, which operate with ET mechanism and result in complicated photophysics and blinking kinetics,[35,36] COT depopulate the T_1 state of a fluorescent molecule through TTET and the degree of depopulation correlates with the enhancement in photostability of the fluorescent molecule.[36]

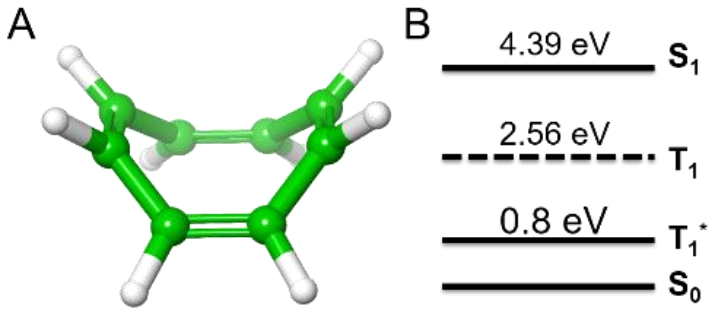

Scheme 3-2. Illustrative scheme of the conformation of COT in its ground electronic state (A) and the energy level scheme of COT (B).[30] T_1 depicted by the dashed line is the triplet state of COT (^{3}COT). Due to conformational distortion during TTET, the relaxed ^{3}COT has a lower energy level, T_1^*.

In this study, using DNA as a platform, we demonstrated that the triplet blinking of ATTO-fluorophore, ATTO 647N can be controlled by collision with COT through TTET. The collision is governed by the conformational dynamics of DNA. Thereby, by studying COT-controlled triplet blinking of ATTO 647N, conformational dynamics of DNA can be investigated in the time range from 10^{-6} to 10^{-3} s. Owing to the aspect of COT being a photostabilizer enabling improving the

photostability of ATTO 647N, the triplet blinking controlled by COT was further monitored at the single-molecule level. A molecular beacon probe bearing COT and ATTO 647N was applied to the single-molecule detection of a model microRNA (miRNA) biomarker, miR-155.

Results and Discussion

To verify whether the triplet blinking of a fluorescent molecule can be controlled by collision in its T_1 state with COT through TTET, and to have an overview of the time range of COT-controlled triplet blinking, we designed a double-stranded DNA (dsDNA) platform, in which COT was placed against the fluorescent molecule ATTO 647N with a $(dT)_n$ or $(dA)_n$ spacer (n = 3, 6, and 12) located in the middle to separate COT and ATTO 647N, as shown in Scheme 3-3.

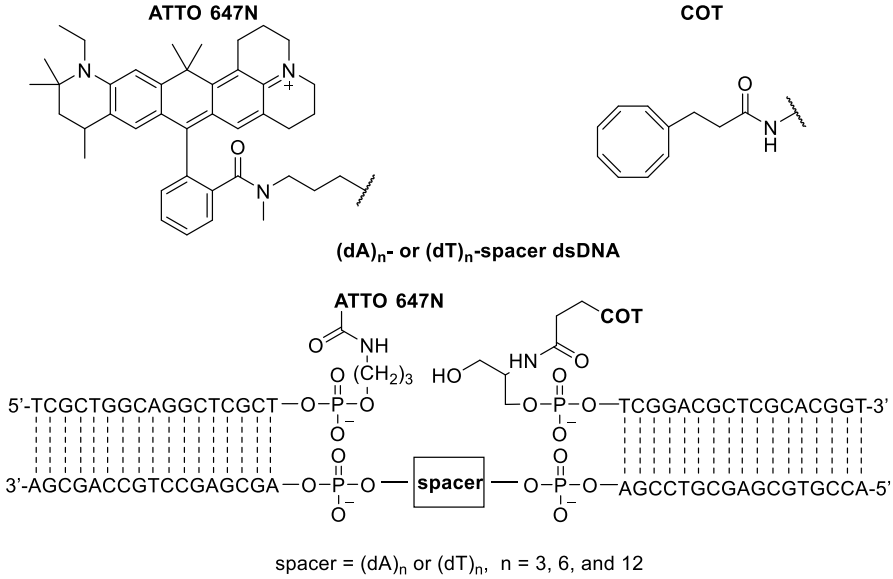

Scheme 3-3. Chemical structures of ATTO 647N and COT and the double-stranded DNA platform with the fluorescent molecule ATTO 647N and the triplet acceptor COT being separated by a spacer, $(dA)_n$ or $(dT)_n$, n = 3, 6, and 12.

First, the effect of COT on the triplet blinking of ATTO 647N was investigated by observing the FCS results of $(dA)_{12}$-spacer dsDNA in the absence and presence of COT. By using a confocal microscope setup, fluctuation of the fluorescence signal when the sample enters and leaves the detection volume was measured with a single photon counting avalanche photodiode

(spAPD). The typical fluorescence time traces for $(dA)_{12}$-spacer dsDNA in the absence and presence of COT under the deoxygenated condition are shown in Figure 3-1. The counter rate which is the number of photons detected per second shows more than 5-times enhancement in the presence of COT compared with that in the absence of COT. This suggests that ATTO 647N in its T_1 state (^{3}ATTO 647N*) is depopulated in the presence of COT. The fluctuation of the fluorescence signal was analyzed using the normalized fluctuation autocorrelation function $G(\tau)$ (Equation 3-1) and the obtained FCS autocorrelation curves in the absence and presence of COT are shown in Figure 3-2. In the presence of COT, by fitting the autocorrelation curve with equation (3-3), the blinking time, τ_{OFF} and τ_{On} were obtained. Where N is the number of molecules within the sample volume element, τ_D is the diffusion time, $S = \omega_1/\omega_0$ in which ω_0 is the radius of the measurement area and ω_1 is the half of its axial length, τ_{OFF} corresponds to the lifetime of T_1 state of ATTO 647N (^{3}ATTO 647N*) and $1/\tau_{OFF}$ is the collision rate of ^{3}ATTO 647N* with COT, and τ_{ON} is related with the intersystem crossing rate and the yield of ^{3}ATTO 647N*, which thus decreases with the increase of irradiation laser dose. In the absence of COT (Figure 3-2), there's only a single relaxation component that has a timescale that is about 20 times faster than the diffusion time, τ_D = 1 ms, measured under the aerobic condition where ^{3}ATTO 647N* is depopulated by O_2. (Figure 3-3). This indicates that in the absence of O_2, the lifetime of ^{3}ATTO 647N* is much longer than the time it takes for the dsDNA assembly to move across the detection volume of the confocal microscope, and thereby once ^{3}ATTO 647N* is formed it does not relax to the S_0 while moving through the detection volume. Thus, this fast relaxation component observed in the absence of COT is ascribed to the relaxation of immediately formed ^{3}ATTO 647N* after the dsDNA assembly enters into the detection volume under the deoxygenated condition. This is consistent with the low count rate observed in the absence of COT, which is more than 5 times as low as that in the presence of COT (Figure 3-1). In sharp contrast, two relaxation components were clearly observed in the presence of COT under the deoxygenated condition (Figure 3-2). The faster component is attributed to the triplet blinking, and the slower component with a relaxation time of 6.6 ms corresponds to the diffusion. After further studying the effect of O_2 on the triplet blinking of ATTO 647N by measuring $(dA)_{12}$-spacer dsDNA under aerobic conditions (Figure 3-3), it is evident that both the increased count rate and the well-resolved triplet blinking component from the diffusion component were only observed in the presence of COT and under the deoxygenated condition. This confirms the control of the triplet blinking of ATTO 647N by COT.

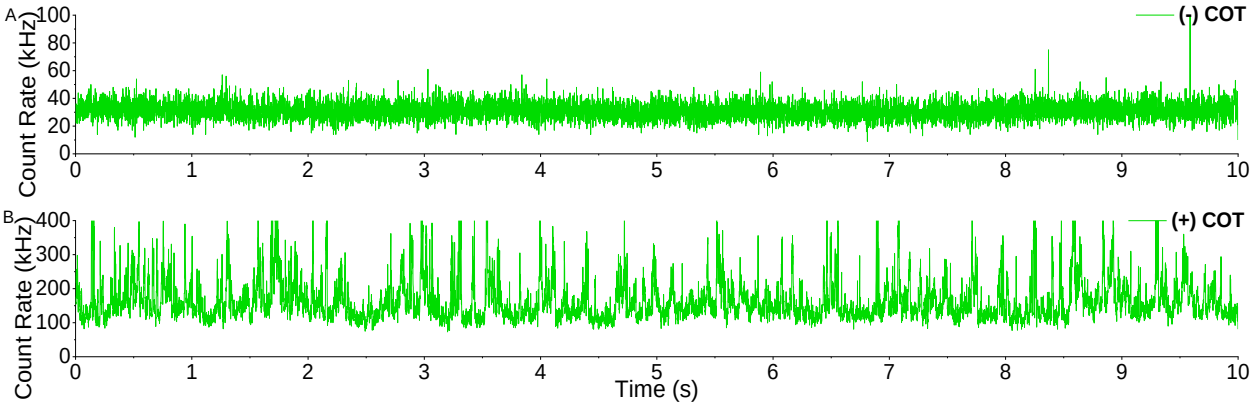

Figure 3-1. Representative fluorescence time traces obtained from $(dA)_{12}$-spacer dsDNA in the absence (A) and presence (B) of COT. Data was collected under the deoxygenated condition and continuous 637 nm excitation with a laser power of 250 μW cm^{-2}.

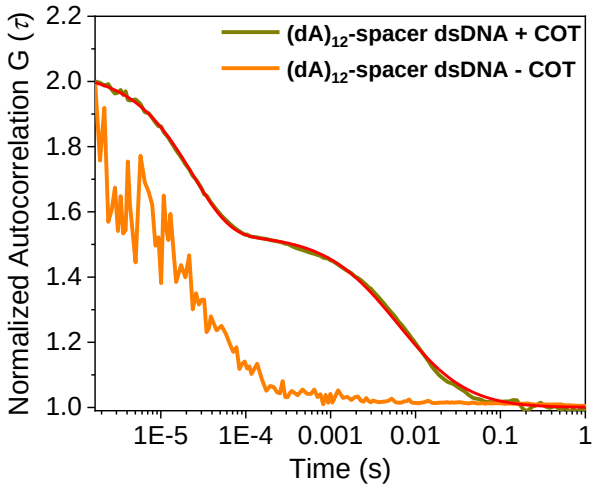

Figure 3-2. Representative FCS autocorrelation curves of $(dA)_{12}$-spacer dsDNA in the absence and presence of COT. The red line is a fitted curve to the autocorrelation curve of $(dA)_{12}$-spacer dsDNA in the presence of COT using equation (3-3). Data was collected under the deoxygenated condition and continuous 637 nm excitation with a laser power of 250 μW cm^{-2}.

$$G(\tau) = 1+\left(\frac{1}{N}\right)\left(\frac{1}{1+\tau/\tau_D}\right)\left(\frac{1}{1+(1/S^2)(\tau/\tau_D)}\right)^{1/2}\left(1+\left(\frac{\tau_{OFF}}{\tau_{ON}}\right)\exp\left(-\tau\left(\frac{1}{\tau_{OFF}}+\frac{1}{\tau_{ON}}\right)\right)\right) \qquad \text{Equation (3-3)}$$

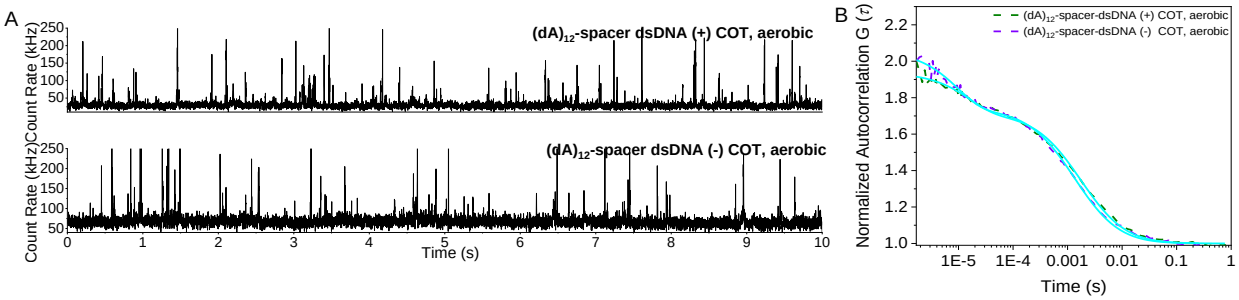

Figure 3-3. Representative fluorescence time traces (A) and FCS autocorrelation curves (B) of $(dA)_{12}$-spacer dsDNA in the absence and presence of COT under the aerobic condition. The cyan lines are fitted curves to the autocorrelation curves of $(dA)_{12}$-spacer dsDNA under the aerobic condition using equation (3-3). Data was collected under the aerobic condition and continuous 637 nm excitation with a laser power of 250 μW cm^{-2}.

Next, we investigated the effect of the spacer between ATTO 647N and COT on the triplet blinking of ATTO 647N controlled by collision with COT. The autocorrelation FCS curves are shown in Figure 3-4. After fitting the FCS curves using equation (3-3), the blinking time, τ_{OFF} and τ_{On} were obtained. Because the collision between ^{3}ATTO 647N* and COT controls the OFF time, τ_{OFF}, the collision rate between ^{3}ATTO 647N* and COT, $k_{collision}$, is thereby obtained using $k_{collision} = 1/\tau_{OFF}$. The collision shows dependence on the length of the spacer between ATTO 647N and COT. As the length of the spacer increases, the collision is slower. The collision also shows a nucleobase dependence when comparing the $(dT)_n$ spacer and $(dA)_n$ spacer with the same length. The dynamics of $(dA)_n$ is slower than that of the corresponding $(dT)_n$ to bring ^{3}ATTO 647N* into contact with COT. This is attributed to the higher rigidity of $(dA)_n$ which is composed of purine bases possessing a two-ringed structure. While the $(dT)_n$ spacer is composed of pyrimidine bases possessing a single-ringed structure. Therefore, the former having a stronger π-stacking interaction showed a τ_{OFF} value larger than that of the latter with the same length. The length and nucleobase dependences of τ_{OFF} clearly demonstrate that the triplet blinking observed herein is triggered by the collision between ^{3}ATTO 647N* and COT and more importantly the collision-controlled triplet blinking reflects the conformational dynamics of single-stranded DNA (ssDNA) spacer in dsDNA.

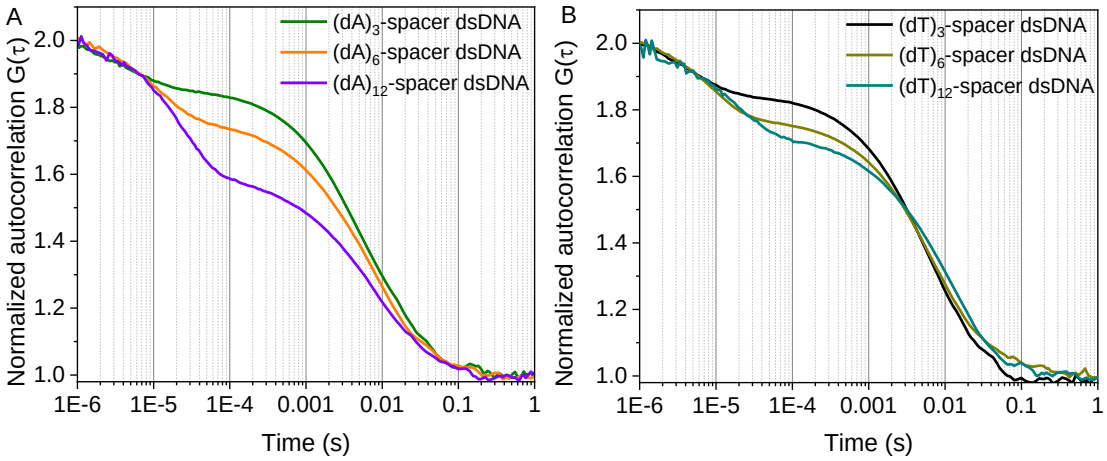

Figure 3-4. Representative FCS autocorrelation curves of $(dA)_n$-spacer dsDNA (A) and $(dT)_n$-spacer dsDNA, n = 3, 6, and 12. Data was collected under the deoxygenated condition and continuous 637 nm excitation with a laser power of 250 μW cm^{-2}.

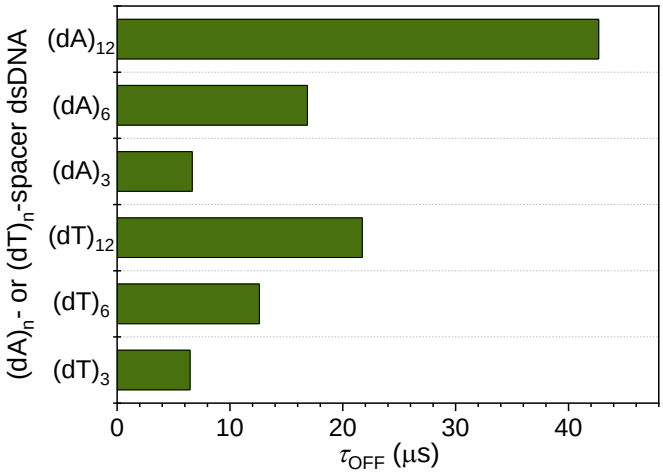

Figure 3-5. Bar graphs summarizing the τ_{OFF} values obtained by fitting the FCS autocorrelation curves in Figure 3-4 with equation (3-3).

Figures 3-6A and B show the effect of laser power on τ_{OFF} and τ_{ON}, respectively. The results suggest that τ_{OFF} for a given sample, $(dA)_n$- or $(dT)_n$-spacer dsDNA, is resistant to the change of laser power, with only slight influence being observed for $(dT)_n$-spacer dsDNA when n = 3 and 6. In contrast, τ_{ON} is affected by applied laser dose and it decreases as the laser dose increases. This is because τ_{ON} reflects the time it takes for a fluorescent molecule to transit from fluorescent S_1

(ON state) to non-fluorescent T_1 (OFF state) and ATTO 647N switches from S_1 to T_1 more often under a higher laser dose than under a lower dose. Herein we focused on $(dA)_3$- and $(dT)_3$-spacer dsDNA. The τ_{OFF} values for both are smaller than 10 μs. When the laser dose increases from 120 μW cm^{-2} to 780 μW cm^{-2}, τ_{ON} values for both shorten to less than 20 μs from around 40 μs, while only slight change was observed for τ_{OFF} values. These results indicate that after an ON time of as short as 20 μs, COT is ready for the next collision reaction with ^{3}ATTO 647N* to depopulate the T_1. Hence, it is inferred that the lifetime of the triplet excited state of COT formed after TTET reaction (^{3}COT*) under the present conditions is shorter than 20 μs, or COT can depopulate ^{3}ATTO 647N* efficiently via triplet-triplet annihilation between ^{3}ATTO 647N* and ^{3}COT*. This highlights the superior characteristics of COT as a conjugated nearby triplet acceptor to depopulate T_1 in aqueous solution.

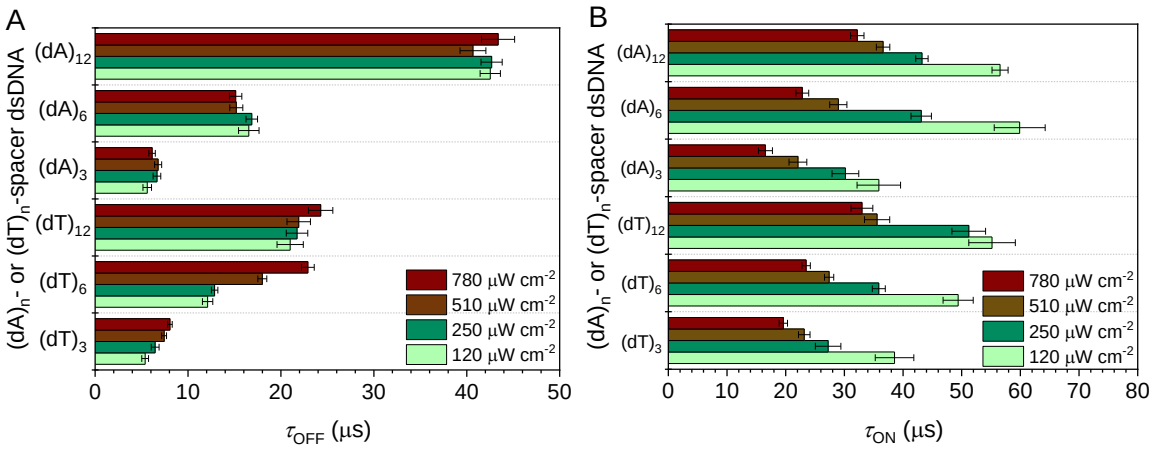

Figure 3-6. Laser power dependence of τ_{OFF} (A) and τ_{ON} (B) for $(dA)_n$ or $(dT)_n$- spacer dsDNA, n = 3, 6, and 12. Data was collected under the deoxygenated condition and continuous 637 nm excitation with different laser doses.

For a given fluorescent molecule, the average number of photons emitted during each ON state before the formation of T_1 is inherent to the fluorescent molecule. For different fluorescent molecules, it varies according to the rate and quantum yield of ISC. Using the dsDNA platform, we also tested the possibility of using other fluorescent molecules to play as a triplet donor to achieve COT-controlled triplet blinking for accessing biomolecular conformational dynamics. These are Cy5, tetramethylrhodamine (TAMRA), Alexa 568, and Alexa 633. Cy5 which was

reported by Blanchard and the co-workers having dramatically enhanced photostability after being directly or proximally conjugated with COT or other triplet quenchers showed a significant contribution from the *tran-cis* isomerization to the blinking under the employed conditions, making it difficult to distinguish the triplet blinking. The other fluorescent molecules, TAMRA, Alexa 568, and Alexa 633, didn't show a clear triplet blinking component nor a correlation between τ_{OFF} and the dynamics of the ssDNA spacers. As a result, ATTO 647N is the optimum choice under the employed conditions, by using which a clear triplet blinking was observed and used to access the conformational dynamics of biomolecules.

By attaching ATTO 647N and COT at the 3'- and 5'- ends of ssDNA (Scheme 3-4), respectively, the looping dynamics of ssDNA was accessed by observing COT-controlled triplet blinking of ATTO 647N. Because it is the looping of ssDNA that induces the collision between ^{3}ATTO 647N* and COT, which controls τ_{OFF}, the looping dynamics of ssDNA whereby can be accessed by τ_{OFF}, as shown in Scheme 3-5.

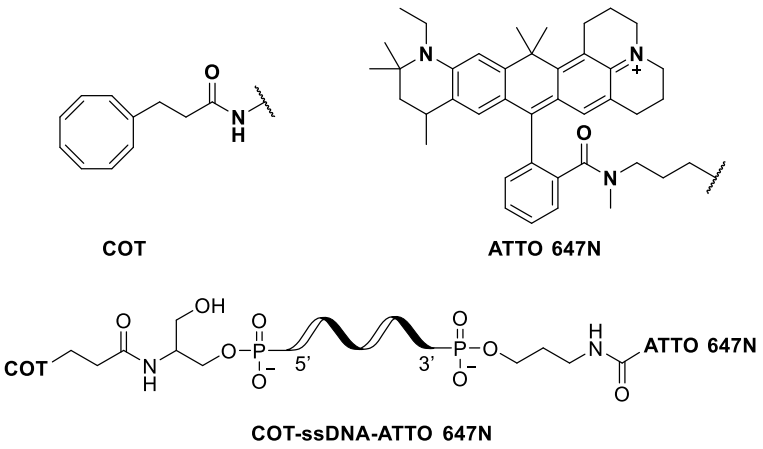

Scheme 3-4. Chemical structures of COT, ATTO 647N, and the modified ssDNA.

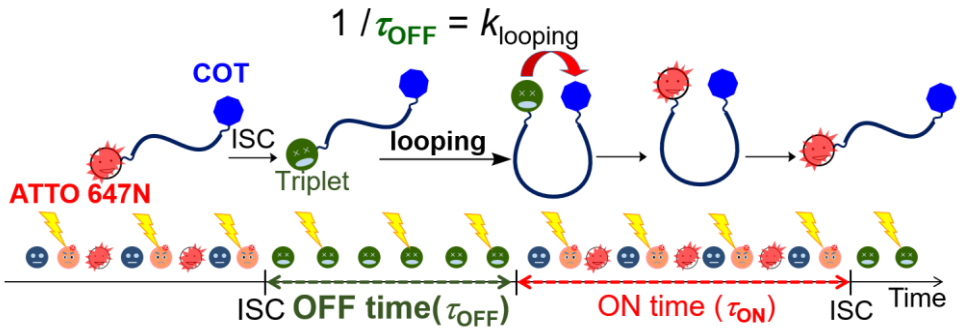

Scheme 3-5. Schematic representation of using COT-controlled triplet blinking of ATTO 647N to access the looping dynamics of ssDNA.

The looping rate of ssDNA obtained using $k_{looping} = 1/\tau_{OFF}$ shows a dependence on the length of ssDNA (Figures 3-7A and B, Table 3-1). It takes a longer time for a longer ssDNA to form an end-to-end loop. $k_{looping}$ is also nucleobase-dependent. The looping rate of $(dT)_n$ is faster than $(dA)_n$ with the same length, consistent with the rigidity difference between them. The dependence of ssDNA looping dynamics on length and nucleobase observed herein complies with that observed in doubly SPy-modified system.[37] However, the $k_{looping}$ for a given ssDNA sequence differs between the doubly SPy-modified system and the system based on COT-controlled triplet blinking of ATTO 647N, as shown in Table 3-1. The difference is mainly originated from the difference in mechanism between the two systems. For doubly SPy-modified ssDNA, the stabilization energy from $SPy^{\bullet+}$ to $SPy_2^{\bullet+}$ makes it thermodynamically favorable to form $SPy_2^{\bullet+}$, the formation of which traps the loop. For this reason, the chance for a given ssDNA to form a loop during looping is increased, which is also the reason that SPy plays as both a probe and a photoregulator. While for COT-ssDNA-ATTO 647N, because there exists no such a stabilization energy during ssDNA looping as in doubly SPy-modified ssDNA, the formation of the loop is less frequent and needs more time. In addition to the difference in mechanisms, the non-identical linkers used in the two systems and the difference in induced interaction between end-linked probes and nucleobase are also possible reasons. The above-mentioned reasons probably also explain the varying of the length dependence of $k_{looping}$ on the length of $(dA)_n$ between two systems. The discrepancy in the observed conformational dynamics afforded from different studying methods is common[38–40] and a method-unifying view is expected.[40]

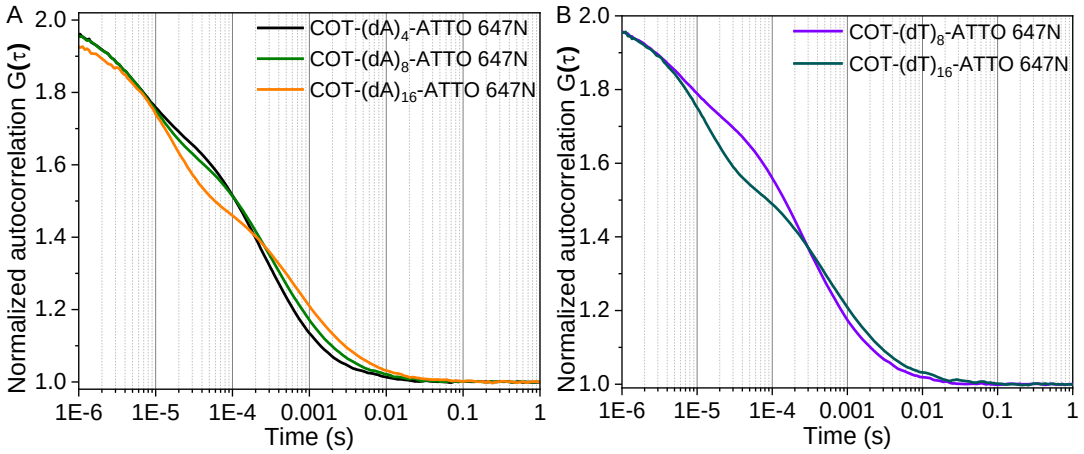

Figure 3-7. Representative FCS autocorrelation curves of COT-$(dA)_n$-ATTO 647N, n = 4, 8, and 16 (A) and COT-$(dT)_n$-ATTO 647N, n = 8 and 16 (B). Data was collected under the deoxygenated condition and continuous 637 nm excitation with a laser power of 250 μW cm^{-2}.

Table 3-1. Comparison of the looping rate between the COT-ssDNA-ATTO 647N system and the doubly SPy-modified ssDNA system

Sequence	$k_{looping}$ (10^6 s^{-1})	Sequence	$k'_{looping}$ (10^6 s^{-1})	$k'_{looping}/k_{looping}$
COT-$(dA)_4$-ATTO 647N	0.11	SPy-$(dA)_4$-SPy	0.73	6.6
COT-$(dA)_8$-ATTO 647N	0.070	SPy-$(dA)_8$-SPy	0.24	3.4
COT-$(dA)_{16}$-ATTO 647N	0.032	SPy-$(dA)_{16}$-SPy	0.053	1.7
COT-$(dT)_8$-ATTO 647N	0.092	SPy-$(dT)_8$-SPy	0.27	2.9
COT-$(dT)_{16}$-ATTO 647N	0.042	SPy-$(dT)_{16}$-SPy	0.13	3.1

The COT-controlled triplet blinking of ATTO 647N was further applied to the detection of miRNA. miRNAs play vital roles in many biological processes such as cell differentiation and apoptosis and the development of cancer.[41–46] The levels of miRNAs can be used as biomarkers for cellular events or diagnosis of early diseases. miR-155 has been reported being a typical miRNA with multiple functions in various physiological and pathological processes, and it has been found over-expressed in many neoplastic diseases and can be used as an important biomarker

for diagnosis, staging, progression, and prognosis of cancers.[47,48] Given the above-mentioned significance of miR-155, studies on the detection of miR-155 and the decrease of its level would be very intriguing and inspiring. Herein, by virtue of COT being a photostabilizer enabling improving the photostability of ATTO 647N, the detection of miR-155 was carried out at the single-molecule level. We used a molecular beacon probe that bears ATTO 647N and COT and undergoes a conformational change upon binding to the target, biomarker miR-155 (Figure 3-8).

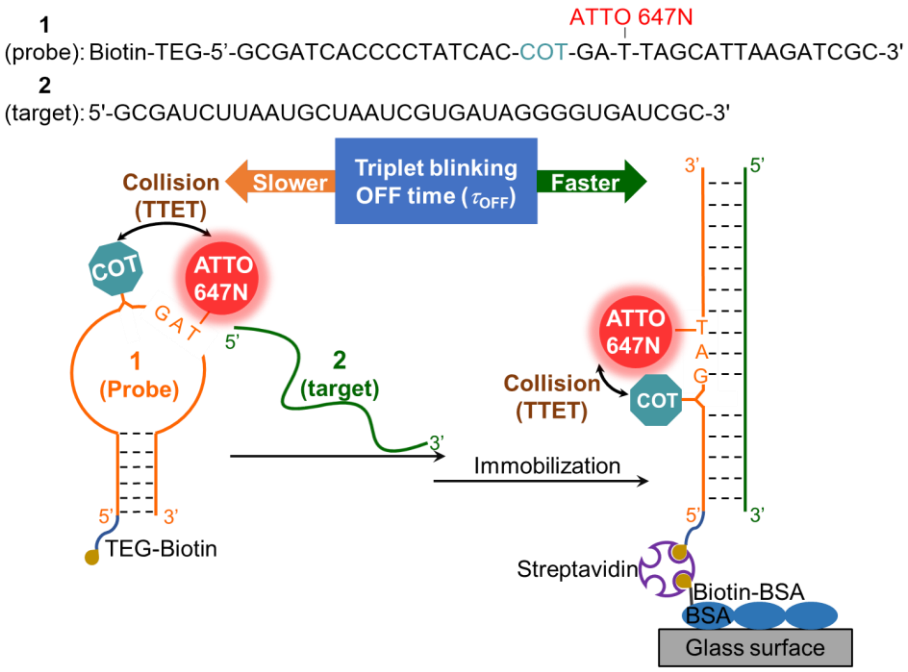

Figure 3-8. Design of a molecular beacon probe **1**, target **2**, and the schematic illustration of the mechanism of detecting target **2** at the single-molecule level.

The molecular beacon probe often bears a pair of a fluorescent molecule and its quencher, and it probes the target based on the increase or decrease in the fluorescence intensity upon binding to the target. Herein, by measuring the COT-controlled triplet blinking of ATTO 647N in both the absence and presence of the target, we can monitor the function of the molecular beacon probe. Owing to the fact that COT protects ATTO 647N from photo-bleaching, the detection was achieved at the single-molecule level.

To detect miR-155, a molecular beacon probe **1** was designed. It has the miR-155 complementary sequence at its hairpin loop region and also bears ATTO 647N and COT in this region (Figure 3-8). The 5' end of probe **1** was modified with biotin allowing the probe to be anchored on a glass surface via well-established streptavidin−biotin chemistry. To avoid the ambiguity arising from the dissociation of the target miRNA, target **2** having both miR-155 and the complementary sequence of the stem of probe **1** was used as a model of miR-155 (Figure 3-8). Probe **1** was so designed that the spatial locations of ATTO 647N and COT in the presence of target **2** differ from those in the absence of target **2.** This would give rise to a difference in COT-controlled triplet blinking of ATTO 647N in the presence and absence of target **2**.

The typical time-dependent fluorescence signals of probe **1** in the absence and presence of target **2** are shown in Figure 3-9A. Two-state ON-OFF blinking and one-step bleaching were observed (Figure 3-9A), indicating that the signals are from a single molecule bearing ATTO 647N and COT. The fluctuation of fluorescence intensity was analyzed using the autocorrelation function G(τ) (Equation 3-1). The normalized autocorrelation curves are shown in Figure 3-9B. The τ_{OFF} value corresponding to the lifetime of ^{3}ATTO 647N* was obtained by fitting the autocorrelation curves using the following equation (3-4),

$$G(\tau)=1+\left(\frac{\tau_{OFF1}}{\tau_{ON1}}\right)\exp\left(-\tau\left(\frac{1}{\tau_{OFF1}}+\frac{1}{\tau_{ON1}}\right)\right)+\left(\frac{\tau_{OFF2}}{\tau_{ON2}}\right)\exp\left(-\tau\left(\frac{1}{\tau_{OFF2}}+\frac{1}{\tau_{ON2}}\right)\right) \qquad \text{Equation (3-4)}$$

where τ_{ON1} and τ_{OFF1} are the durations of ON state and OFF state, respectively, in the major faster-blinking component, COT-controlled triplet blinking of ATTO 647N; τ_{ON2} and τ_{OFF2} originate from a minor slower-blinking component, most probably attributed to the remaining O_2-induced blinking of ATTO 647N. Since τ_{ON1} is hundreds of μs (the average values of τ_{ON1} for probe **1** in the absence and presence of target **2** were 270 and 110 μs, respectively) and τ_{ON2} is over 1ms with an average value of tens of ms (60 and 10 ms for probe **1** in the absence and presence of target **2**, respectively), the yield of the faster triplet blinking component is 100 times as high as that of the

slower component. As a result, the slower component is a minor process. Because τ_{OFF2} is on the order of 10^{-4} s and it has been reported that the oxygen scavenger system

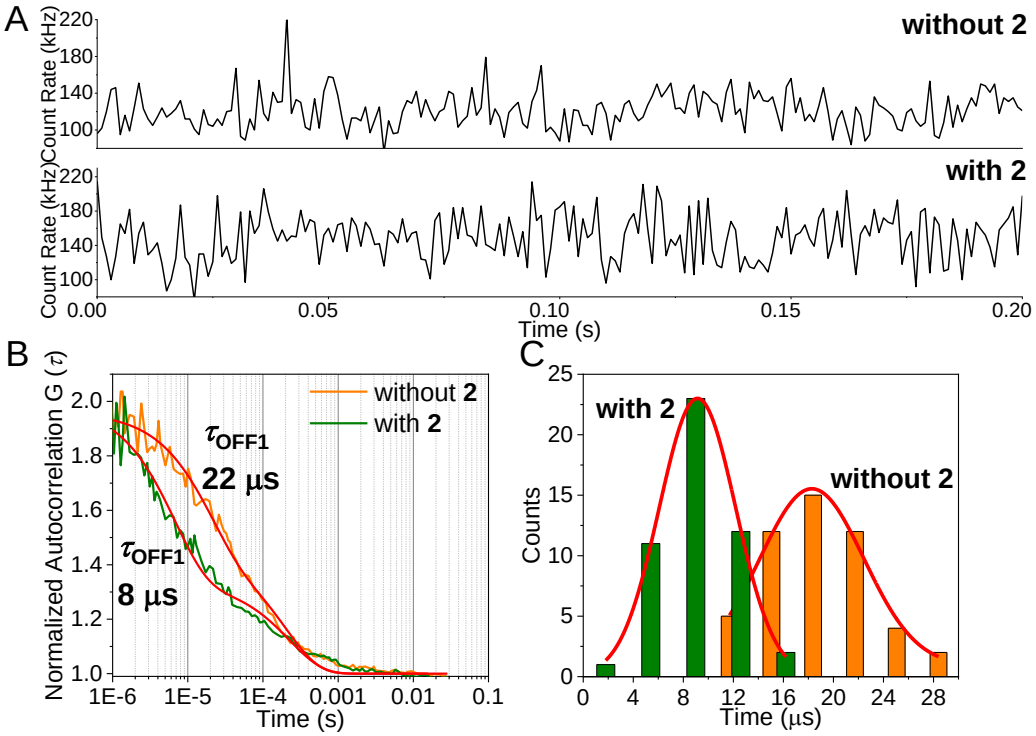

Figure 3-9. (A) Representative fluorescence time traces obtained from a single **1** molecule attached to the glass surface in the presence and absence of target **2**. (B) Autocorrelation analyses of fluorescence time traces in A. (d) Histograms of τ_{OFF1} value measured from more than 50 individual **1** molecule in the presence and absence of target **2**.

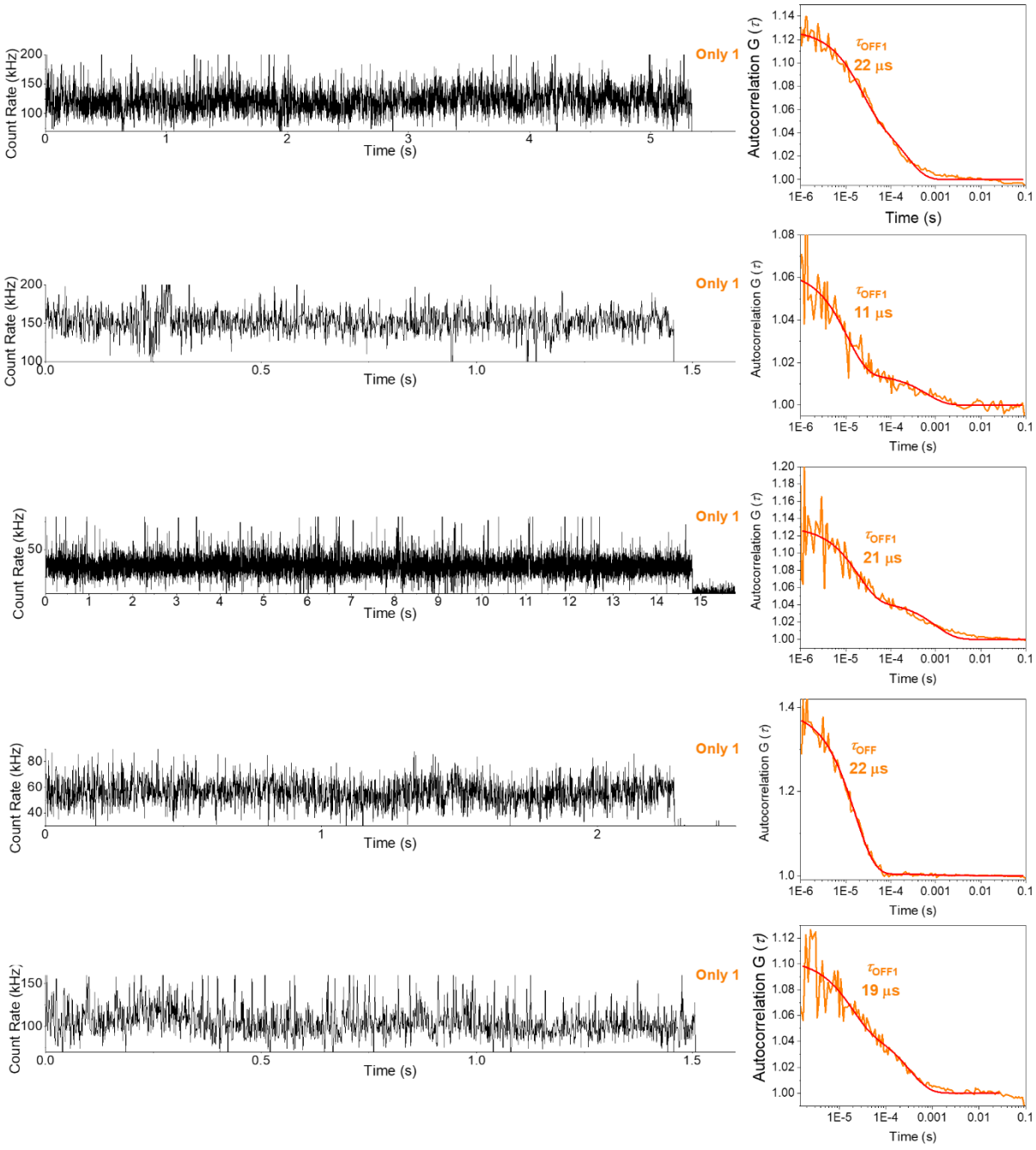
Only 1
Count Rate (kHz)
Time (s)
Autocorrelation G (τ)
τOFF1
22 µs
Only 1
Count Rate (kHz)
Time (s)
Autocorrelation G (τ)
τOFF1
11 µs
Only 1
Count Rate (kHz)
Time (s)
Autocorrelation G (τ)
τOFF1
21 µs
Only 1
Count Rate (kHz)
Time (s)
Autocorrelation G (τ)
τOFF
22 µs
Only 1
Count Rate (kHz)
Time (s)
Autocorrelation G (τ)
τOFF1
19 µs

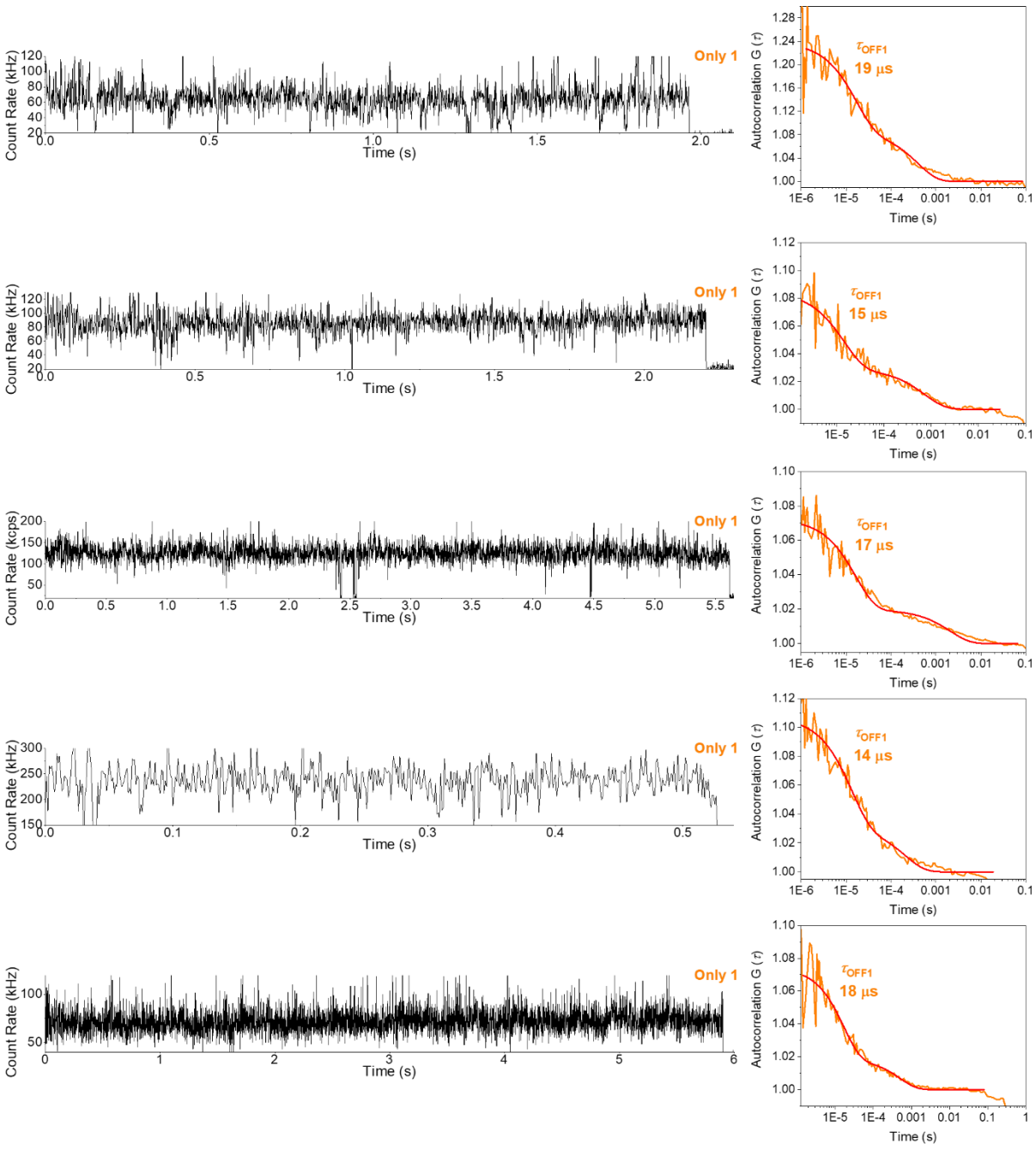

Figure 3-10. Representative fluorescence time traces (Left) obtained from a single **1** molecule attached to the glass surface and the corresponding autocorrelation analyses (Right).

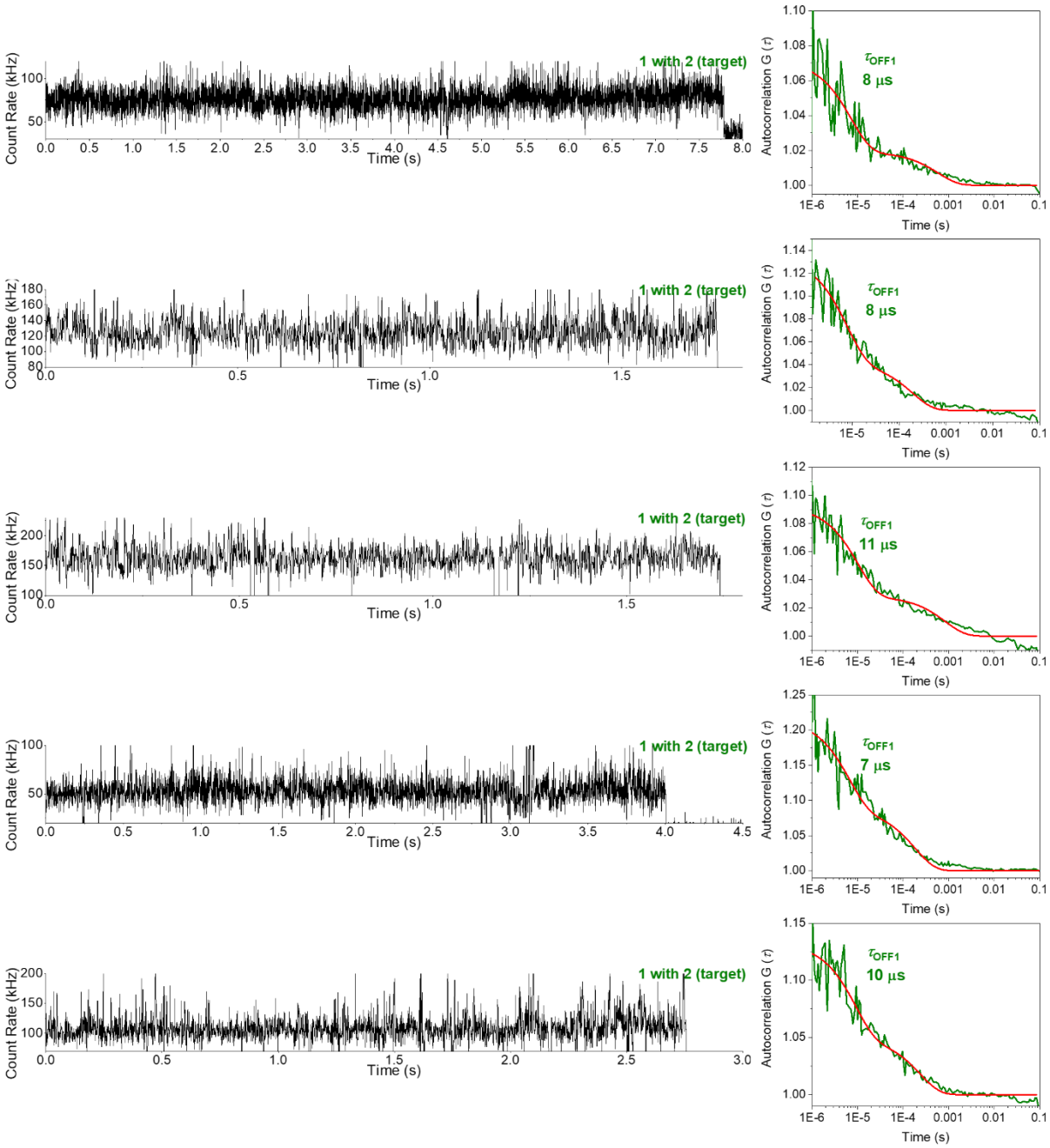
1 with 2 (target)
Count Rate (kHz)
Time (s)
Autocorrelation G (τ)
τOFF1
8 µs
1 with 2 (target)
Count Rate (kHz)
Time (s)
Autocorrelation G (τ)
τOFF1
8 µs
1 with 2 (target)
Count Rate (kHz)
Time (s)
Autocorrelation G (τ)
τOFF1
11 µs
1 with 2 (target)
Count Rate (kHz)
Time (s)
Autocorrelation G (τ)
τOFF1
7 µs
1 with 2 (target)
Count Rate (kHz)
Time (s)
Autocorrelation G (τ)
τOFF1
10 µs

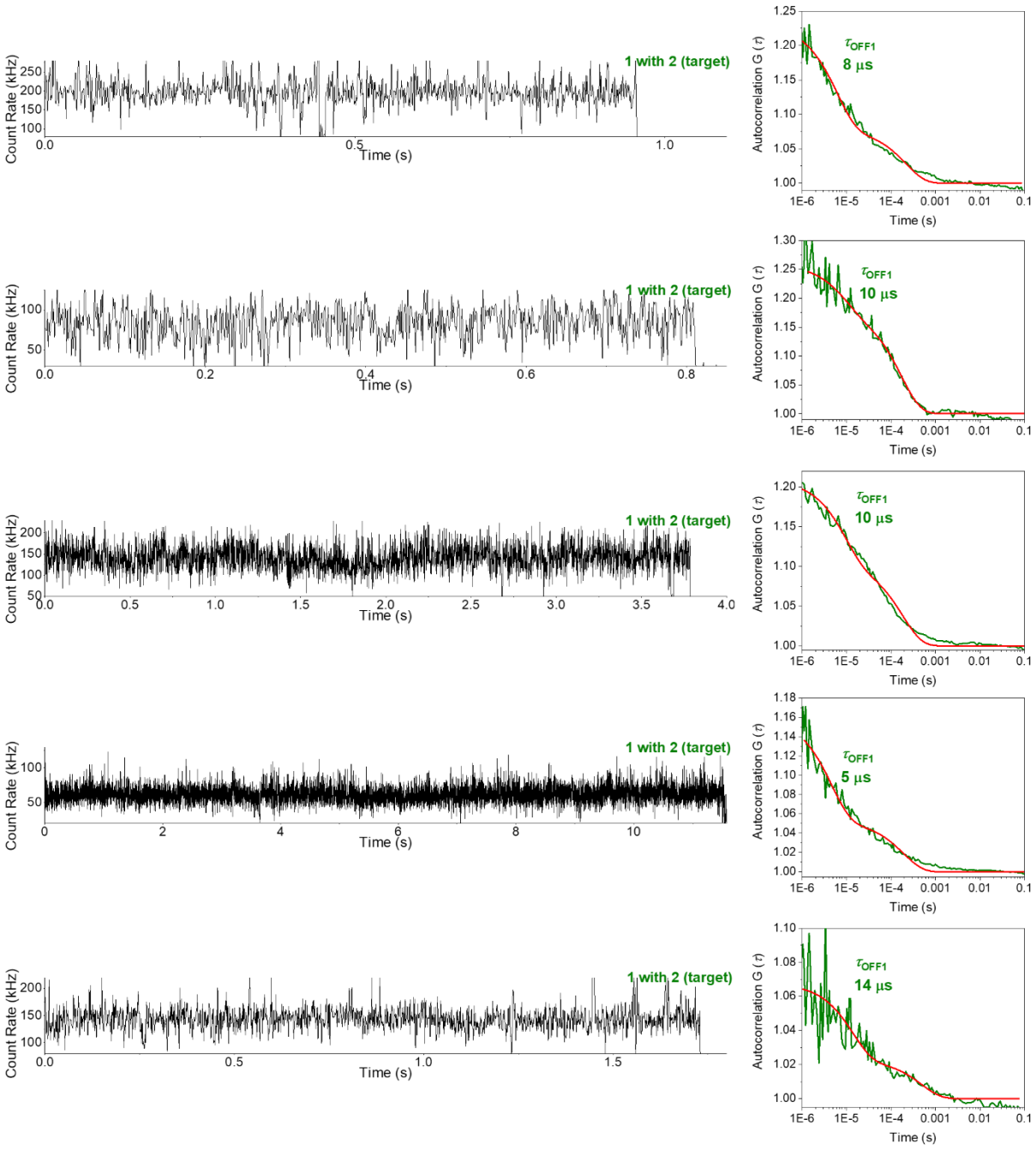

Figure 3-11. Representative fluorescence time traces (Left) obtained from a single **1** molecule attached to the glass surface in the presence of target **2** and the corresponding autocorrelation analyses (Right).

of glucose oxidase in combination with catalase and glucose offers a steady-state O_2 concentration of ca. 14 μM which can lead to a triplet lifetime of ~10^{-4} s,[49] it is reasonable to assign the minor and slower component to the blinking induced by the remaining O_2 in the solution. In addition, occasionally, only the faster component was observed (Figures 3-10 and 3-13), and the autocorrelation curves can be well-fitted with the following equation (3-5),

$$G(\tau)=1+\left(\frac{\tau_{OFF1}}{\tau_{ON1}}\right)\exp\left(-\tau\left(\frac{1}{\tau_{OFF1}}+\frac{1}{\tau_{ON1}}\right)\right) \qquad \text{Equation (3-5)}$$

This supports the above-mentioned assignment. Figure 3-9C shows the histograms of τ_{OFF1} value measured from 50 individual molecules of probe **1** in the absence and presence of target **2**. The lifetime of ^{3}ATTO 647N, τ_{OFF1}, which reflects the dynamics of probe 1 or the heteroduplex formed by hybridization of probe 1 with target 2 to bring 3ATTO 647N* into collision with COT to have a TTET reaction, was determined from the Gaussian fit. As designed, a difference in τ_{OFF1} in the presence and absence of target **2** was observed—the τ_{OFF1} value in the presence of target **2** is about one-half of that in the absence of target **2**. In the absence of target **2**, the slower kinetics of collision between ^{3}ATTO 647N* and COT gave a slower triplet blinking kinetics of ATTO 647N, indicating that ATTO 647N and COT are flexibly moving around. On the other hand, a faster triplet blinking kinetics was observed in the presence of target **2**. This suggests that ATTO 647N and COT in the formed heteroduplex are close to each other with a spatial location easier to have a TTET reaction. To get further insight on the selectivity of probe **1**, a control miRNA (control **3** in Figure 3-12) consisting of both the region differing from miR-155 and the region complementary to the stem of probe **1** was employed (Figure 3-12). The very similar distribution of τ_{OFF1} in the absence and presence of control **3** obtained from 50 individual molecules reveals the high selectivity of probe **1** toward target **2** (Figure 3-12). These results demonstrate that the TTET kinetics between ATTO 647N and COT can be utilized to detect miRNA at the single-molecule level by measuring the triplet blinking of ATTO 647N.

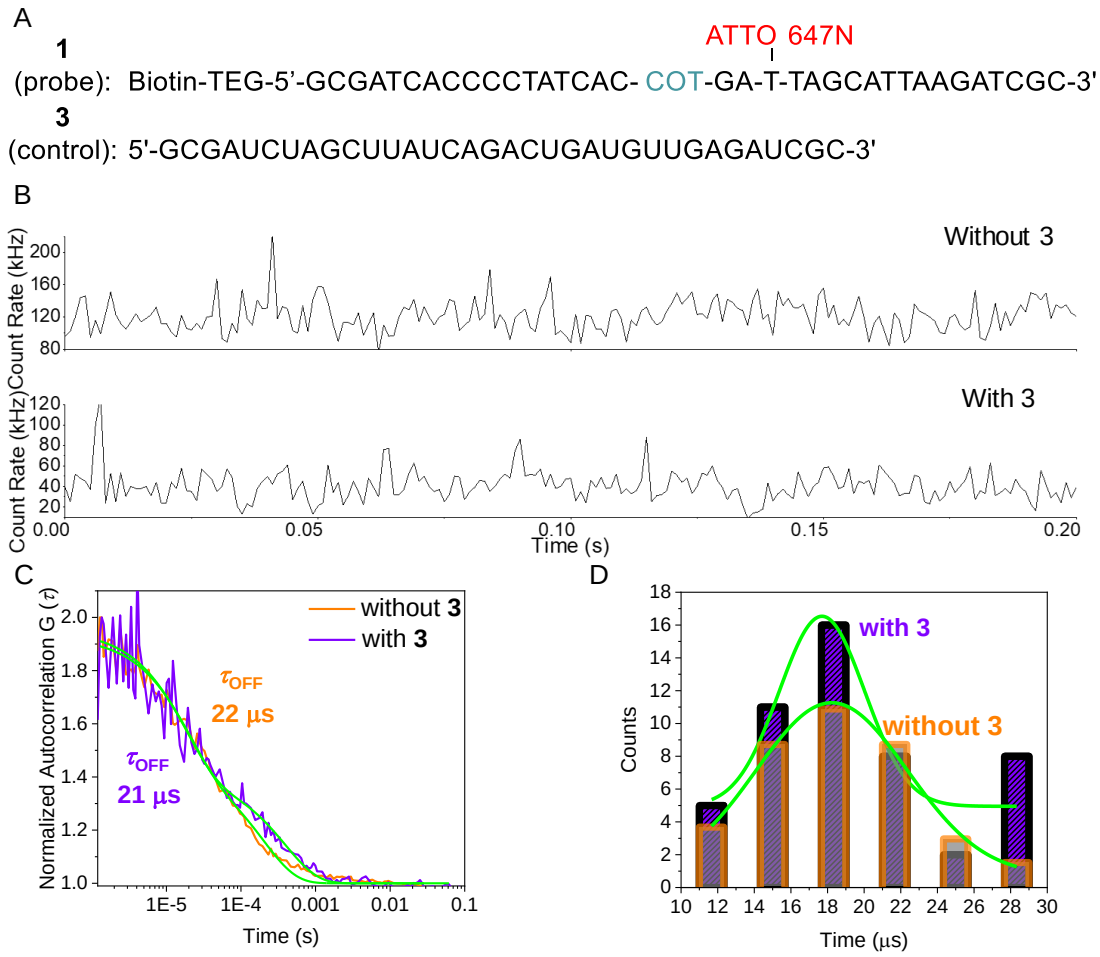

Figure 3-12. (A) Molecular beacon probe **1** and control **3** used as a control miRNA of target **2**. (B) Representative fluorescence time traces obtained from a single **1** molecule attached to the glass surface in the presence and absence of control **3**. (c) Autocorrelation analyses of fluorescence time traces in (B). (D) Histograms of τ_{OFF1} value measured from more than 50 individual **1** molecule in the presence and absence of control **3**.

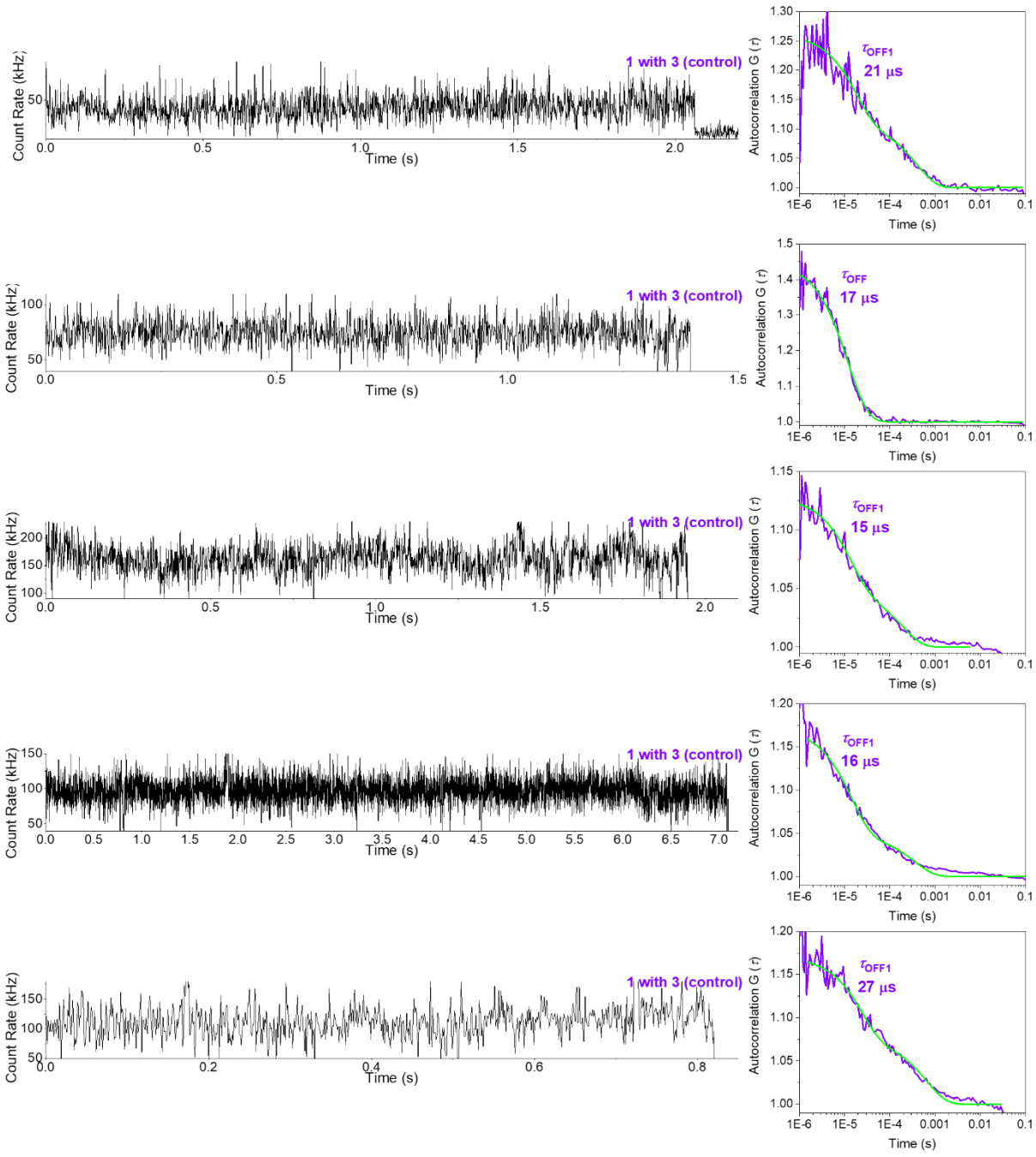
1 with 3 (control)
Count Rate (kHz)
Time (s)
Autocorrelation G (τ)
τOFF1
21 µs
1 with 3 (control)
Count Rate (kHz)
Time (s)
Autocorrelation G (τ)
τOFF
17 µs
1 with 3 (control)
Count Rate (kHz)
Time (s)
Autocorrelation G (τ)
τOFF1
15 µs
1 with 3 (control)
Count Rate (kHz)
Time (s)
Autocorrelation G (τ)
τOFF1
16 µs
1 with 3 (control)
Count Rate (kHz)
Time (s)
Autocorrelation G (τ)
τOFF1
27 µs

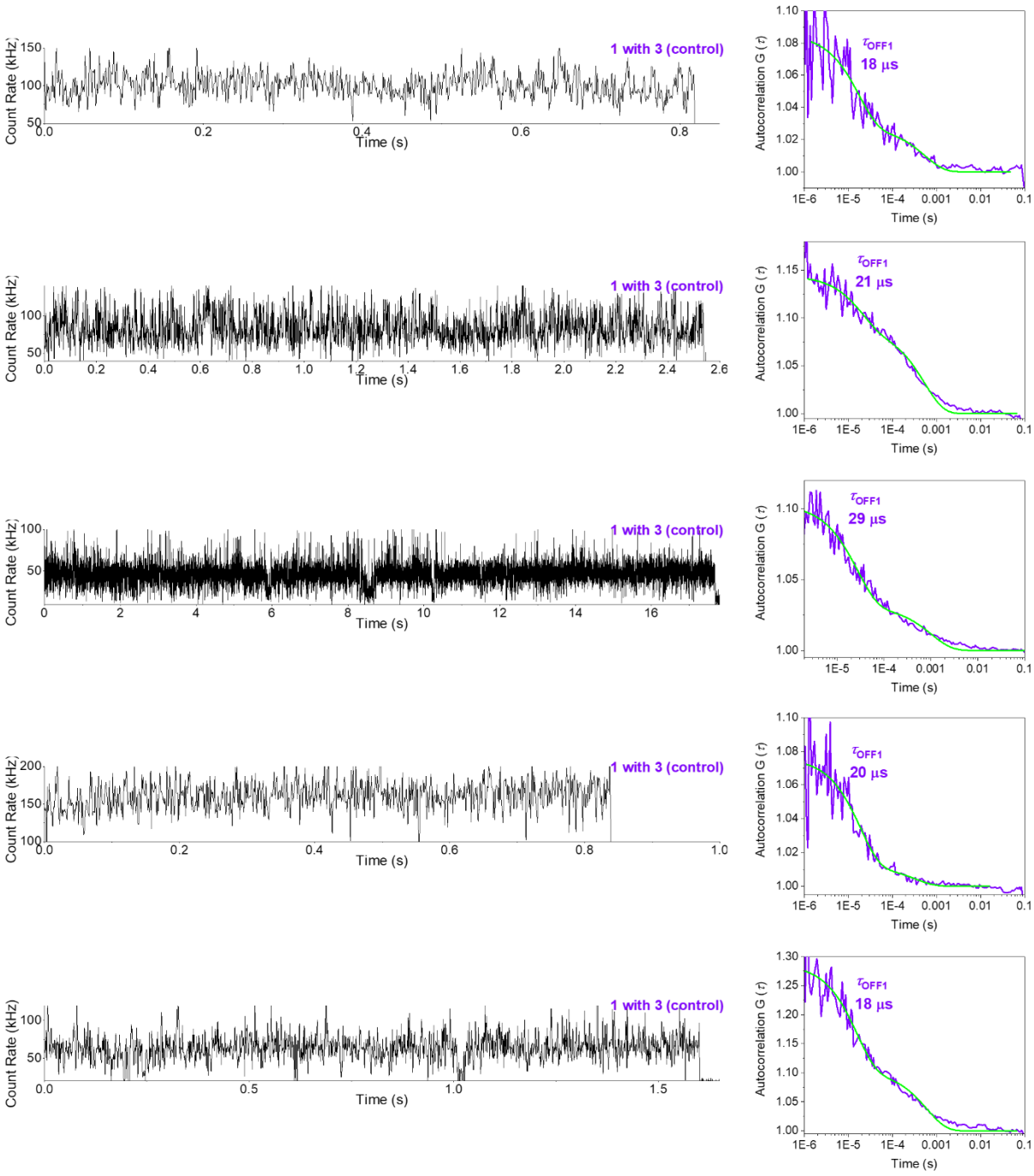

Figure 3-13. Representative fluorescence time traces (Left) obtained from a single **1** molecule attached to the glass surface in the presence of control **3** and the corresponding autocorrelation analyses (Right).

Conclusion

In summary, it was demonstrated that COT works as a superior triplet acceptor in aqueous solution and it depopulates ^{3}ATTO 647N* by TTET, which makes the triplet blinking of ATTO 647N being clearly observed. Owing to the fact that COT plays as both a superior triplet acceptor and a photostabilizer protecting ATTO 647N from photo-bleaching, the controlled triplet blinking of ATTO 647N by COT can be monitored at the single-molecule level. This enables us to study the looping dynamics of ssDNA and detection of target miRNA at the single-molecule level in the time range from 10^{-6} to 10^{-3} s. This method also serves as a complementary method to single-molecule Förster resonance energy transfer (smFRET) and offers a general and powerful tool to access the dynamics of biomolecules and to detect biomarkers at the single-molecule level.

Experimental Section

Materials. All DNA samples were purchased from Gene Design, Inc. Target **2** and control **3** were synthesized by Japan Bio Services Co., LTD. All samples are HPLC oligonucleotides and used as received. The UltraPure water TM DNase/RNase-free Distilled Water from Thermo Fisher Scientific Inc. was used in all FCS measurements. Other chemicals were purchased from the standard suppliers and used without further purification.

Fluorescence correlation spectroscopy (FCS). The FCS measurements were carried out on an inverted microscope (IX73, Olympus) with a 637 nm (OBIS 637 LX, Coherent) or a 532 nm (Sapphire 532 LP, Coherent) CW laser source. Through a dichroic mirror and an objective of NA 1.4 (UPLXAPO40XO 40 × Oil, Olympus) in case of bulk measurement unless specially mentioned or NA 1.42 (UPLXAPO60XO 60 × Oil, Olympus) during single-molecule measurement, the laser beam was focused on the coverslip. The confocal optical system with a pinhole (diameter 25 μm, MPH16, Thorlabs) attached to the side port of the microscope allows only the in-focus area (confocal volume) to be detected. Emitted fluorescence photons from fluorescent molecules inside the confocal volume were detected by a single-photon avalanche photodiode (spAPD) (SPCM-AQRH-14, Perkin-Elmer), and the output was sent to a counting board (USP-FCS-16MB, Unisoku). A band-pass filter (FF01-697/58-25, 582/75-25, Semrock) was used to block the scattered light. A real-time data processing system of Spcm64 (Becker & Hickl GmbH) recorded the real-time fluorescence intensity called time trace. Autocorrelation of the detected fluorescence intensity using FCS software of UNISPEC (Spectroscopy & Kinetics, Unisoku) generated the autocorrelation curves. The laser excitation power was measured by a power meter (S170C, Thorlabs).

Bulk measurement of dsDNA platform with fluorescence and COT being separated by a spacer. A 80 μL solution containing 1.5 nM 3’ end F-attached ssDNA (5’-TCGCTGGCAGGCTCGCT-ATTO 647N), 3 nM 5’ end COT-attached ssDNA (COT-TCGGACGCTCGCACGGT-3’), 2.25 nM spacer-containing ssDNA (5’-ACCGTGCGAGCGTCCGA-spacer-AGCGAGCCTGCCAGCGA-3’ in which spacer is $(dA)_n$ or $(dT)_n$, n = 3, 6, or 12), and 18% (w/v) PEG 20000 was heated to 90 ℃ and naturally cooled down to room temperature in annealing buffer (10 mM PBS buffer, 10 mM $MgCl_2$, pH 7.2). The oxygen scavenger system of glucose oxidase in combination with catalase and glucose was used to remove

oxygen from the system. Before measurement, 5 μL solution of 50 μM (320 U mL^{-1}) glucose oxidase, 5 μL solution of 16 μM (19200 U mL^{-1}) catalase, and 10 μL solution of 280 mM glucose were added to the pre-annealed dsDNA solution and the mixture were quickly added to the well (384 well, Greiner Bio-One Int.). The well was then immediately sealed.

For the measurement under the aerobic condition, the scavenging reagents were replaced by 20 μL water. In the case of measurement without COT, 5' end COT-attached ssDNA was replaced by ssDNA without COT.

During the measurement, a cycle duration was 10 s and 10 cycles were measured for one sample. The average autocorrelation curve was used as the final result. The measurement was carried out at room temperature.

Bulk measurement of COT-ssDNA-ATTO 647N. The sample solution (45 μL) containing 2 nM COT-ssDNA-ATTO 647N, 2.5 μM glucose oxidase, 0.8 μM catalase from Bovine liver, and 28 mM glucose in 10 mM phosphate buffer (pH 7.0) was quickly added to the well (384 well, Greiner Bio-One Int.). The well was then immediately sealed.

During the measurement, a cycle duration was 10 s and 10 cycles were measured for one sample. The average autocorrelation curve was used as the final result. The measurement was carried out at room temperature.

Single-molecule measurement (detection of a model microRNA biomarker—miR-155)

20 μL solution containing 20 nM probe 1 (5'-Biotin-TEG-GCGATCACCCCTATCAC-COT-GA-ATTO 647N modified T-TAGCATTAAGATCGC-3'GCGA), 80 nM target 2 (5'-GCGAUCUUAAUGCUAAUCGUGAUAGGGGUGAUCGC-3') or 80 nM control 3 (5'-GCGAUCUAGCUUAUCAGACUGAUGUUGAGAUCGC-3') was heated to 90 ℃ and naturally cooled down to room temperature in annealing buffer (10 mM PBS buffer, 150 mM NaCl, 1 mM EDTA, pH 7.4).

The well (96-well, eppendorf) was incubated with 100 μL solution containing 62.50 μg mL^{-1} BSA (Sigma Aldrich) and 1.25 μg mL^{-1} biotin-labeled BSA (Sigma Aldrich) in PBS buffer (10 mM, 137 mM NaCl, pH 7.4) at 4℃ overnight. This was followed by rinsing with PBS buffer. After that, the well was further incubated with 100 μL solution of 0.20 mg mL^{-1} streptavidin in PBS buffer (10

mM, 137 mM NaCl, pH 7.4) for 10 min followed by rinsing with PBS buffer (10 mM, 137 mM NaCl, pH 7.4).[50]

The pre-annealed sample solution was diluted to 1/160 (125 pM probe **1**) with a buffer solution containing 10 mM phosphate buffer (pH 7.4), 150 mM NaCl, and 1 mM EDTA. The immobilization of the pre-annealed sample on the glass surface was realized via the interaction between biotin and streptavidin. The pre-incubated well was further incubated with the diluted sample solution for 2 min. After rinsing with a buffer containing 10 mM phosphate buffer (pH 7.4) and 150 mM NaCl, the sample was immobilized to the glass surface.

Before measurement, a solution containing phosphate buffer (pH 7.4), NaCl, EDTA, and PEG 20000, and solutions of glucose oxidase, catalase, and glucose were added to the sample-immobilized well. The total volume of solution in the well is 370 μL and the concentration of each is: 10 mM phosphate buffer, 150 mM NaCl, 1 mM EDTA, 10% (w/v) PEG-20000, 38 U mL^{-1} glucose oxidase, 415 U mL^{-1} catalase, and 7.6 mM glucose. The well was sealed and incubated for 5 min at room temperature.

The single-molecule measurement was carried out under continuous 637 nm excitation with a laser power of 6 μW cm^{-2} at 27 °C.

References

[1] S. van de Linde, I. Krstić, T. Prisner, S. Doose, M. Heilemann, M. Sauer, *Photochem. Photobiol. Sci.* **2011**, *10*, 499–506.

[2] Q. Qi, C. Li, X. Liu, S. Jiang, Z. Xu, R. Lee, M. Zhu, B. Xu, W. Tian, *J. Am. Chem. Soc.* **2017**, *139*, 16036–16039.

[3] T. Ha, P. Tinnefeld, *Annu. Rev. Phys. Chem.* **2012**, *63*, 595–617.

[4] M. Heilemann, S. van de Linde, A. Mukherjee, M. Sauer, *Angew. Chem. Int. Ed.* **2009**, *48*, 6903–6908.

[5] K. Nienhaus, G. Ulrich Nienhaus, *Chem. Soc. Rev.* **2014**, *43*, 1088–1106.

[6] A. Acharya, A. M. Bogdanov, B. L. Grigorenko, K. B. Bravaya, A. V Nemukhin, K. A. Lukyanov, A. I. Krylov, *Chem. Rev.* **2017**, *117*, 758–795.

[7] S. Uno, M. Kamiya, T. Yoshihara, K. Sugawara, K. Okabe, M. C. Tarhan, H. Fujita, T. Funatsu, Y. Okada, S. Tobita, Y. Urano, *Nat. Chem.* **2014**, *6*, 681–689.

[8] S. van de Linde, M. Heilemann, M. Sauer, *Annu. Rev. Phys. Chem.* **2012**, *63*, 519–540.

[9] P. Schäfer, S. van de Linde, J. Lehmann, M. Sauer, S. Doose, *Anal. Chem.* **2013**, *85*, 3393–3400.

[10] E. Haustein, P. Schwille, *Methods* **2003**, *29*, 153–166.

[11] S. Chiantia, J. Ries, P. Schwille, *Biochim. Biophys. Acta - Biomembr.* **2009**, *1788*, 225–233.

[12] N. Opitz, P. J. Rothwell, B. Oeke, P. Schwille, *Sensors Actuators B Chem.* **2003**, *96*, 460–467.

[13] M. Á. Medina, P. Schwille, *BioEssays* **2002**, *24*, 758–764.

[14] H. Yang, G. Luo, P. Karnchanaphanurach, T.-M. Louie, I. Rech, S. Cova, L. Xun, X. S. Xie, *Science.* **2003**, *302*, 262–266.

[15] K. A. Henzler-Wildman, M. Lei, V. Thai, S. J. Kerns, M. Karplus, D. Kern, *Nature* **2007**, *450*, 913–916.

[16] L. R. Ganser, M. L. Kelly, D. Herschlag, H. M. Al-Hashimi, *Nat. Rev. Mol. Cell Biol.* **2019**, *20*, 474–489.

[17] A. M. Mustoe, C. L. Brooks, H. M. Al-Hashimi, *Annu. Rev. Biochem.* **2014**, *83*, 441–466.

[18] K. F. Freed, *Acc. Chem. Res.* **1978**, *11*, 74–80.

[19] Z.-Q. You, C.-P. Hsu, G. R. Fleming, *J. Chem. Phys.* **2006**, *124*, 44506.

[20] B. Fierz, T. Kiefhaber, *J. Am. Chem. Soc.* **2007**, *129*, 672–679.

[21] F. Krieger, A. Möglich, T. Kiefhaber, *J. Am. Chem. Soc.* **2005**, *127*, 3346–3352.

[22] S. Neumaier, M. Büttner, A. Bachmann, T. Kiefhaber, *Proc. Natl. Acad. Sci. U.S.A.* **2013**, *110*, 20988–20993.

[23] B. Fierz, H. Satzger, C. Root, P. Gilch, W. Zinth, T. Kiefhaber, *Proc. Natl. Acad. Sci. U.S.A.* **2007**, *104*, 2163–2168.

[24] S. Chiantia, J. Ries, P. Schwille, *Biochim. Biophys. Acta - Biomembr.* **2009**, *1788*, 225–233.

[25] K. Bacia, E. Haustein, P. Schwille, *Cold Spring Harb. Protoc.* **2014**, *7*, 709–725.

[26] C. Eggeling, J. Widengren, R. Rigler, C. A. M. Seidel, in *Appl. Fluoresc. Chem. Biol. Med.* (Eds.: W. Rettig, B. Strehmel, S. Schrader, H. Seifert), Springer Berlin Heidelberg, Berlin, Heidelberg, **1999**, pp. 193–240.

[27] B. Li, L. Lin, H. Lin, B. C. Wilson, *J. Biophotonics* **2016**, *9*, 1314–1325.

[28] S. Schols, A. Kadashchuk, P. Heremans, A. Helfer, U. Scherf, in *Org. Light Emit. Mater. Devices XIII*, Proc. SPIE, San Diego, California, United States, **2009**, p. 74150A.

[29] L. M. Frutos, O. Castaño, J. L. Andrés, M. Merchán, A. U. Acuña, *J. Chem. Phys.* **2004**, *120*, 1208–1216.

[30] S. Schols, A. Kadashchuk, P. Heremans, A. Helfer, U. Scherf, in *Proc.SPIE*, **2009**.

[31] L. M. Frutos, O. Castaño, J. L. Andrés, M. Merchán, A. U. Acuña, *J. Chem. Phys.* **2004**, *120*, 1208–1216.

[32] V. Balzani, F. Bolletta, F. Scandola, *J. Am. Chem. Soc.* **1980**, *102*, 2152–2163.

[33] L.-M. Frutos, O. Castaño, M. Merchán, *J. Phys. Chem. A* **2003**, *107*, 5472–5478.

[34] R. B. Altman, D. S. Terry, Z. Zhou, Q. Zheng, P. Geggier, R. A. Kolster, Y. Zhao, J. A. Javitch, J. D. Warren, S. C. Blanchard, *Nat. Methods* **2012**, *9*, 68–71.

[35] T. Cordes, J. Vogelsang, P. Tinnefeld, *J. Am. Chem. Soc.* **2009**, *131*, 5018–5019.

[36] Q. Zheng, S. Jockusch, Z. Zhou, R. B. Altman, J. D. Warren, N. J. Turro, S. C. Blanchard, *J. Phys. Chem. Lett.* **2012**, *3*, 2200–2203.

[37] J. Xu, S. Miyamoto, S. Tojo, K. Kawai, *Chem. Eur. J.* **2020**, *26*, 5075–5084.

[38] T. Uzawa, T. Isoshima, Y. Ito, K. Ishimori, D. E. Makarov, K. W. Plaxco, *Biophys. J.* **2013**, *104*, 2485–2492.

[39] T. Uzawa, R. R. Cheng, K. J. Cash, D. E. Makarov, K. W. Plaxco, *Biophys. J.* **2009**, *97*, 205–210.

[40] M. H. Jacob, R. N. D'Souza, T. Schwarzlose, X. Wang, F. Huang, E. Haas, W. M. Nau, *J.*

Phys. Chem. B **2018**, *122*, 4445–4456.

[41] R. Shen, Y. Wang, C.-X. Wang, M. Yin, H.-L. Liu, J.-P. Chen, J.-Q. Han, W.-B. Wang, *Am. J. Transl. Res.* **2015**, *7*, 2115–2126.

[42] W. Kong, L. He, E. J. Richards, S. Challa, C.-X. Xu, J. Permuth-Wey, J. M. Lancaster, D. Coppola, T. A. Sellers, J. Y. Djeu, J. Q. Cheng, *Oncogene* **2014**, *33*, 679–689.

[43] Y. Tay, J. Zhang, A. M. Thomson, B. Lim, I. Rigoutsos, *Nature* **2008**, *455*, 1124–1128.

[44] R. A. Shivdasani, *Blood* **2006**, *108*, 3646–3653.

[45] A. M. Cheng, M. W. Byrom, J. Shelton, L. P. Ford, *Nucleic Acids Res.* **2005**, *33*, 1290–1297.

[46] N. Lynam-Lennon, S. G. Maher, J. V Reynolds, *Biol. Rev.* **2009**, *84*, 55–71.

[47] T. S. Elton, H. Selemon, S. M. Elton, N. L. Parinandi, *Gene* **2013**, *532*, 1–12.

[48] D. Jurkovicova, M. Magyerkova, L. Kulcsar, M. Krivjanska, V. Krivjansky, A. Gibadulinova, I. Oveckova, M. Chovanec, *Neoplasma* **2014**, *61*, 241–251.

[49] C. E. Aitken, R. A. Marshall, J. D. Puglisi, *Biophys. J.* **2008**, *94*, 1826–1835.

[50] J. H. M. van der Velde, J. J. Uusitalo, L.-J. Ugen, E. M. Warszawik, A. Herrmann, S. J. Marrink, T. Cordes, *Faraday Discuss.* **2015**, *184*, 221–235.

General Conclusion

In this dissertation, a water-soluble pyrene (Py) derivative, sulfonated pyrene (**SPy**), was synthesized and used for the study of dynamics of oligonucleotide looping using laser flash photolysis. Two end-attached **SPys** play as probes tracing the dynamics of oligonucleotide looping. They are also photoregulators controlling the conformational change of oligonucleotide through oligonucleotide looping. At the same time, a novel method—1,3,5,7-Cyclooctatetraene (COT)-controlled triplet blinking of ATTO 647N—was developed for studying the conformational dynamics of biomolecules and detection of protein.

In Chapter 1, **SPy** was synthesized and characterized. A 1 mM (390 mg/L) **SPy** solution can be prepared. This makes it possible to use Py derivatives under physiological conditions. By attaching two **SPy**s at both ends of single-stranded DNA (ssDNA), the dynamics of ssDNA looping was studied by observing the formation rate of **SPy** dimer radical cation ($\mathbf{SPy_2^{\bullet+}}$) using laser flash photolysis. The dynamics of ssDNA looping depends on length and nucleobase. As the length increases, looping slows down. Looping of poly(dA) is slower than poly(dT) with the same length, which is because the stronger π-stacking interaction in poly(dA) makes it more rigid than poly(dT). The formation of misfolded conformation during ssDNA looping was observed in 8-mer poly(dT), supporting the configurational diffusion model. Apart from playing as probes tracing the dynamics of ssDNA looping, two end-attached **SPy**s also play as photoregulators controlling the conformational change of ssDNA from an unlooped state to a looped state trapped by $\mathbf{SPy_2^{\bullet+}}$ through ssDNA looping.

In Chapter 2, the dynamics of single-stranded RNA (ssRNA) looping was studied using **SPy** based on laser flash photolysis. By comparing the looping dynamics between ssRNA and ssDNA, it was found that the looping dynamics of poly(rA) is 1.3-times slower than the corresponding poly(dA), while the looping dynamics of 16-mer poly(rU) was found 1.4-times faster than 16-mer poly(dT). A thorough discussion of the difference is made by taking into account the extra hydration around ribose 2'-OH, the presence and absence of C5-CH_3 in thymine and uracil, respectively, the intrinsic flexibility or rigidity of oligonucleotide, and the stabilization energy from **SPy** radical cation ($\mathbf{SPy^{\bullet+}}$) to $\mathbf{SPy_2^{\bullet+}}$. The extra hydration around ribose 2'-OH induces a restricted retarding effect on ssRNA looping, while the absence of C5-CH_3 in uracil makes poly(rU) more flexible and having faster looping dynamics compared with poly (dT). However,

the effects of extra hydration around ribose 2'-OH and C5-CH_3 are not the decisive factors controlling the dynamics of oligonucleotide looping. The decisive factor is the internal flexibility or rigidity of an oligonucleotide, which determines the looping to be controlled by internal friction or solvent friction.

In Chapter 3, COT was proposed as a triplet acceptor to control the triplet blinking of ATTO 647N through triplet-triplet energy transfer (TTET). Using a double-stranded DNA (dsDNA) platform, it was demonstrated that indeed COT controls the triplet blinking ATTO 647N and it plays like a superior triplet acceptor in aqueous solution. The controlled triplet blinking of ATTO 647N by COT can be used for accessing the looping dynamics of ssDNA and detection of miRNA at the single-molecule level in the time range from 10^{-6} to 10^{-3} s. The observed enhanced fluorescence intensity in the presence of COT suggests the role of COT as a photostabilizer improving the performance of ATTO 647N.

In summary, in this dissertation, a water-soluble Py derivative, **SPy**, was synthesized and used as both a probe tracing the dynamics of oligonucleotide looping and a photoregulator controlling the conformational change of oligonucleotide. The dynamics of oligonucleotide looping was studied using laser flash photolysis. Multiple factors that affect the dynamics of oligonucleotide looping were observed and discussed, including length effect, nucleobase effect, extra hydration around 2'-OH, the absence and presence of C5-CH_3, the stabilization energy from $\mathbf{SPy}^{\bullet+}$ to $\mathbf{SPy_2}^{\bullet+}$. At the same time, a novel method was developed and used for accessing the dynamics of oligonucleotide looping and detection of protein in the time range from 10^{-6} to 10^{-3} s on the subnanometer scale. The synthesis and use of **SPy** provide an effective and universal way to the future use of Py derivatives under physiological conditions. With water-soluble Py derivative, it is possible to study the conformational dynamics of other biomolecules. The findings on the dynamics of oligonucleotide looping provide an improved understanding of the dynamic movement of oligonucleotides in aqueous solution. This is of fundamental importance to the understanding of the motions and functions of oligonucleotides. The developed novel method—COT-controlled triplet blinking of ATTO 647N—offers an approach complementary to the widely used FRET for studying the conformational dynamics of biomolecules. All the insight gained in this dissertation contributes to the further understanding of the conformational dynamics of biomolecules.

List of Publication

1. Jie Xu, Shunichi Miyamoto, Sachiko Tojo, Kiyohiko Kawai, Sulfonated Pyrene as a Photoregulator for Single-Stranded DNA Looping**.** *Chem. Eur. J.* **2020**, *26*, 5075-5084.

2. Jie Xu, Sachiko Tojo, Mamoru Fujitsuka, Kiyohiko Kawai. Dynamics of Single-Stranded RNA Looping Probed and Photoregulated by Sulfonated Pyrene. *ChemistrySelect* **2020**, *5*, 8002-8008.

3. Jie Xu, Shuaya Fan, Lei Xu, Atsushi Maruyama, Mamoru Fujitsuka, Kiyohiko Kawai, Control of Triplet Blinking Using Cyclooctatetraene to Access the Dynamics of Biomolecules at the Single-Molecule Level. *Angew. Chem. Int. Ed.* Accepted. https://doi.org/10.1002/anie.202101606.

4. Jie Xu, Mamoru Fujitsuka, Kiyohiko Kawai, Cyclooctatetraene as a Triplet Blinking Controller for Revealing the End-to-End Collision Dynamics of Oligonucleotide using Fluorescence Correlation Spectroscopy (tentative). In preparation.

Acknowledgments

First of all, the author would like to express her deepest appreciation and gratitude to Professor Mamoru Fujitsuka for his valuable suggestions on the research and his considerable help throughout the author's master and doctor courses.

The author really wants to show her heartfelt thanks and appreciation to Associate Professor Kiyohiko Kawai who is the advisor of her research. Without his help and direction, the author cannot achieve her goal of research. The author will forever be grateful for the encouragement and help he gave the author.

The author sincerely thanks Associate Professor Yasuko Osakada for her significant help and encouragement in the past five years both on research and life.

The author owns her special thanks to Assistant Professor Sachiko Tojo for her great help on the measurements of laser flash photolysis and pulse radiolysis. The author thanks the members of the Research Laboratory for Quantum Beam Science of ISIR for their help in running the linear accelerator.

The author is indebted to Professor Mikiji Miyata for his help and encouragement. As a learned scholar, his enthusiasm for science influenced the author.

The author very much appreciates the comments from Professor Kazuya Kikuchi and Professor Michiya Matsusaki on the dissertation and sincerely thanks them.

The author also wants to express her thanks to Professor Tetsuro Majima, and Specially-Appointed Assistant Professor Akira Sugimoto for their direction and help during the master course of the author. The author is grateful to Ms. Sooyeon Kim for her generous help during the master course of the author.

The author very much appreciates the help from other members in the lab and the happiness they shared with the author. The author thanks Dr. Ruan Daming, and Mr. Xue Jiawei for their help on both the research and life. The author highly appreciates Mr. Miyamoto Schunichi's contribution. The author is thankful to Ms. Xu Lei, Miss Li Xinxi, Miss Fan Shuya, Mr. Liu Zuoyue, and Mr. Okada Yuta for their help and the happy time with them. The author wants to show her thanks to all the former members. Especially, the author thanks Dr. Lin Shih-Hsun for his considerable help during the author's master course.

The author offers her sincere gratitude to the Japanese government for the financial support they offered to the author.

Last but not least the author deeply thanks her family and her friends for their continuous support and encouragement to the author in her life.

Jie Xu

2020